WIRELESS POWER TRANSFER FOR OIL WELL APPLICATIONS

A Thesis

Presented to

the Faculty of the Department of Electrical and Computer Engineering

University of Houston

In Partial Fulfillment

of the Requirements for the Degree

Doctor of Philosophy

in Electrical Engineering

by

Xiyao Xin

August 2015

WIRELESS POWER TRANSFER FOR OIL WELL APPLICATIONS

Xiyao Xin

Approved:

Chair of the Committee
Ji Chen, Ph.D., Professor
Department of Electrical and Computer Engineering

Committee Members:

David R. Jackson, Ph.D., Professor
Department of Electrical and Computer Engineering

Stuart Long, Ph.D., Professor
Department of Electrical and Computer Engineering

Driss Benhaddou, Ph.D., Associate Professor
Department of Engineering Technology
College of Technology

George Zouridakis, Ph.D., Professor
Department of Engineering Technology
College of Technology

Suresh K. Khator, Ph.D.,
Associate Dean,
Cullen College of Engineering

Badri Roysam, Ph.D., Professor and
Chair of the Department in Electrical and Computer Engineering

Acknowledgements

I would like to express my most sincere thanks to my thesis advisor, Dr. Ji Chen. It is his guidance and encouragement throughout the whole period of my Ph.D. that inspires me to focus on this research topic and to persistently seek for an answer to this on-going research problem. Special thanks to Dr. David R. Jackson, for his guidance on electromagnetic theory and for his sharp review on each idea, theory and formula that I presented to him. I also would like to thank my committee members, Dr. Stuart Long, Dr. Driss Benhaddou, and Dr. George Zouridakis who provided valuable review comments for my thesis.

Special thanks to Mr. Ran Guo, who helped me to obtain crucial experiment data to validate the theory provided in this thesis. Also thanks to Mr. Jingshen Liu, Mr. Xing Huang, Mr. Qingyan Wang, Dr. Jianfeng Zheng and Dr. Zubiao Xiong who discussed with me about the details of the experiments.

Also, I would like to thank Mr. Paul Tubel for his support and valuable opinions to our research.

Lastly, I would like to express my most gratitude to my parents, who support me all along in my pursuit of scientific research. All these years they have been encouraging me to become an independent researcher and develop my own "methodology." I am still not sure whether I have fulfilled their expectations or not, but I will keep trying.

WIRELESS POWER TRANSFER FOR OIL WELL APPLICATIONS

An Abstract

of a

Thesis

Presented to

the Faculty of the Department of Electrical and Computer Engineering

University of Houston

In Partial Fulfillment

of the Requirements for the Degree

Doctor of Philosophy

in Electrical Engineering

by

Xiyao Xin

August 2015

Abstract

Modern oil industry requires detailed monitoring and management to reduce the risks of unwanted fluid release. Sensors need to be planted along oil wells to gather the downhole environment data. However, there are production packers along oil pipes that are used to provide a seal between pipe casing and tubing to control pipe pressure. Such structures make it difficult for power cables to extend along oil pipes. In order to provide power supply on both sides of production packers, we consider wireless power transfer technique via inductive magnetic coupling between two coils wound along oil pipes. But eddy current induced in metallic pipe and sea water in oil well will counteract the flux link between the transmitting and receiving coils. Also, the distance of power transfer is limited due to the fast decay of the inductive magnetic field.

In this research, we propose a long distance wireless power transfer system along the oil pipes with acceptable efficiency. We cover the oil pipe with a thin layer of soft ferrite, and we add a soft ferrite core to the transmitting and receiving coils. We use FEM simulation software to analyze the magnetic flux link improved by the ferrite structures. A CAD model is used to extract FEM field solutions to estimate the power transfer efficiency, and the estimated efficiency is compared and validated with measurement. We will show through FEM simulation and experiments that the ferrite layer on oil pipe forms a magnetic flux pathway and greatly enhances the flux link between transmitter and receiver, and by building a flux pathway extending through pipe, we are able to make the long distance wireless power transfer in oil well possible.

Table of Contents

List of Figures

List of Tables

Chapter 1 Introduction

1.1 Background and Motive

In the modern oil industry, an emphasis is placed on the security and durability of the oil pipe and the related mechanical systems. The concept of reducing risks of undesired fluid release, mechanical breakdown and the oil well malfunction is called well integrity, and there are standards regulating the activities of well integrity to ensure the quality and security of the oil well operations [1]. Management activities based on daily data entry are necessary for well integrity [2]. Such data include pressure, temperature [3], and CO_2 migration quantity [4], and we need sensors implanted along oil pipe casings to record the data transmitted back to the surface [5]. Such sensors need an electric power supply but power cables are not able to extend freely along oil wells due to production packers, and feed cable through packers via special electrical "penetrators" will add risks of malfunctioning of the packers and wellheads; modifications to packers will add costs to the maintenance of the wells [6]. However, to ensure a better quality of well integrity, we always want a larger coverage of the sensors for collecting data. We propose the solution of wireless power transfer to overcome the difficulty of transmitting electric power across the production packer. In this research, we are going to propose a system with two coils wound along an oil pipe as the power transmitter and the receiver, and the electric power is transferred across the production packer on the receiving coil by magnetic induction.

1.2 Methods of Wireless Power Transfer

1.2.1 Resonant Power Transfer

The technique of wireless power transfer originates from the research of Nikola Tesla, who proposed to transmit power through air and ground using resonant electromagnetic fields [7, 8]. Tesla's wireless power transfer model is a LC resonant circuit driven by a coil with alternating current. The model is illustrated in Figure 1-1.

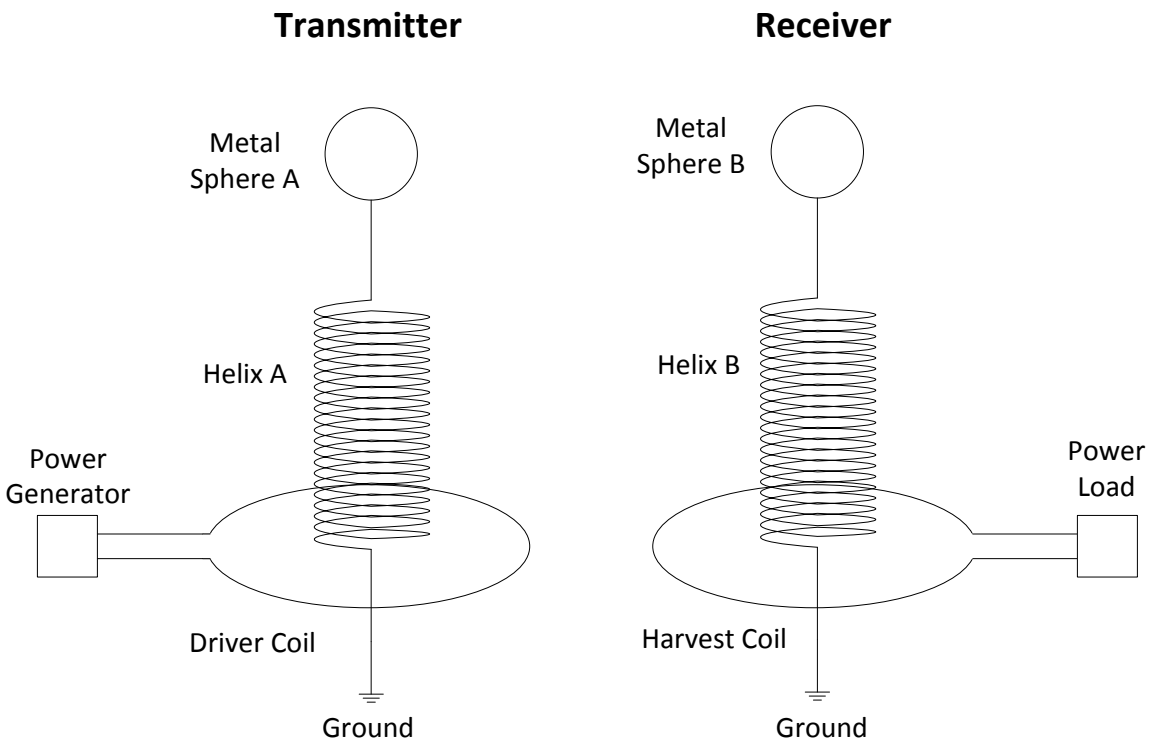

Figure 1-1. The wireless power transfer system by Nikola Tesla.

The helix coil structures and metal spheres in Figure 1-1 form the LC (inductor and capacitor) resonating circuit in both the transmitters and the receivers. When the frequency of the alternating current becomes the self-resonant frequency of the LC circuit, strong alternating electromagnetic fields are induced in space and the displacement current in open space between the spheres and the conductive current in the

ground form the current loop that transmits the electric power from the transmitter to the receiver without continuous cable connections between the power generator and the power load. The concept of LC resonance is an important contribution made by Tesla but using the displacement current induced by LC resonance to transfer power is unsafe and difficult to control. The LC resonance model not only induces strong displacement current within the capacitive components, but also creates strong time varying magnetic field in the inductive components (in Figure 1-1, it is the helix A and B that we are referring to). Therefore instead of using the displacement current, WiTricity group in MIT proposed making the use of magnetic field in the self-resonance LC structure to implement the wireless power transfer system [9]. The model designed by WiTricity group is shown in Figure 1-2.

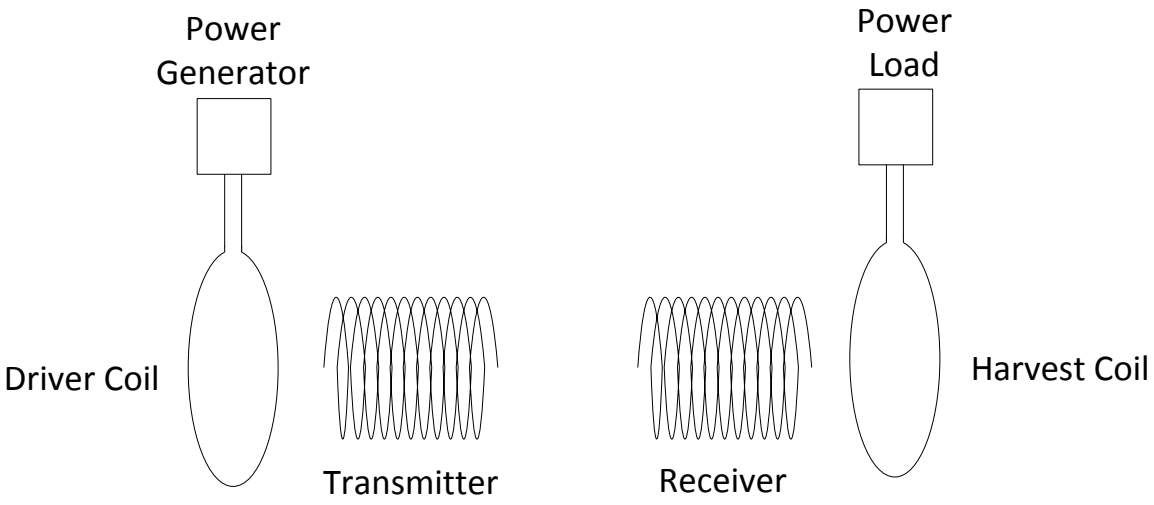

Figure 1-2. The wireless power transfer system by WiTricity group.

The model in Figure 1-2 makes use of the inductive feature of the helix transmitter and receiver and the parasitic capacitance of the helix structure to implement the LC resonance. At the resonant frequency, the strength of the magnetic field generated

by the transmitter reaches maximum and induce an alternating electromagnetic field on the receiver. The harvest coil adjacent to the receiver converts the magnetic field to the electric voltage drop that drives the power load connected to it. According to [9], such two self-resonant coils with very high Quality factor (Q) can reach 2 meters of transmitting distance with an efficiency of about 40%. However, such long distance and high efficiency power transfer system requires a very accurate tuning of both the transmitting coil and the receiving coil to ensure that they have the same self-resonant frequency. Resonant power transfer systems developed by [7, 8, 9] could reach high efficiency in lab, but is hard to be implemented to fit in actual industrial applications.

1.2.2 Inductive Power Transfer

Instead of harvesting the magnetic field from a highly resonant helix coil, we can directly harvest the magnetic field from the transmitter coil via magnetic induction. Such inductive power transfer technique has been widely used for consumer electronics. The idea of inductive power transfer is to connect the power generator and the transmitting coil with a matching network to ensure the maximum current on the coil on desired frequencies. We also connect power load to the receiving coil via matching network to obtain the maximum power output. The matching network can be as simple as a single tuning capacitor [10] or as complicated as series of LC circuit networks [11, 12]. The model of the inductive coupling power transfer is illustrated in Figure 1-3.

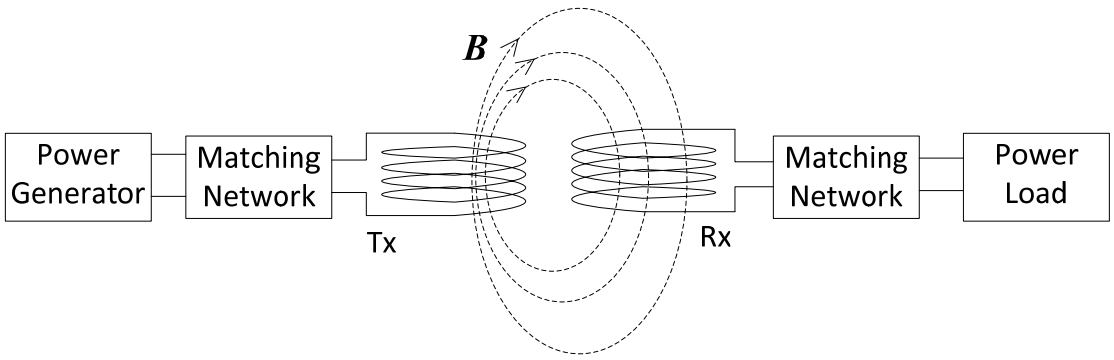

Figure 1-3. The inductive power transfer system model.

Both resonant power transfer and inductive power transfer uses reactive near field induction to perform power transfer. Near fields induced by a current source (in this case, current in the transmitting coil) decays rapidly as the observation point of the field becomes far away from the source. If the distance from the observation point to the current source is r, then the reactive power decays with the order of $1/r^6$ [13]. Such fast decay to some degree limits the power transfer distance of power transfer. There are research works that use radiating fields to transfer power wirelessly [14, 15]. Radiating fields have a lesser decay than reactive near fields in free space but it may decay faster in environments with conductive loss as the radiating field decays exponentially in lossy media. The conductive loss in oil well environment is inevitable. Therefore, using the inductive power transfer system to deliver the electric power across the production packer in an oil well is a reasonable choice. We could wind coils on each side of the production packer as the power transmitter and the receiver. The electric power can then be coupled from the primary coil to the receiving coil by the mutual inductance between them. The tentative model of inductive power transfer along an oil pipe is given in Figure 1-4.

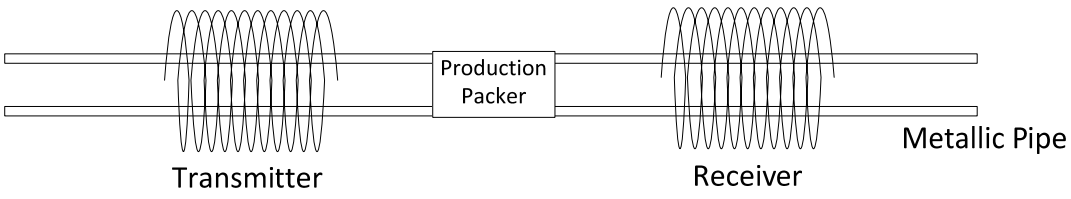

Figure 1-4. Wireless power transfer along oil pipe.

1.2.3 Acoustic Power Transfer

There are also researches done to deliver power via acoustic waves. Acoustic waves can be generated by piezoelectric transducers under the excitation of electric voltages, and similarly, the transducer will induce an electric voltage drop under the excitation of mechanical vibration [16]. Therefore a pair of transducers in the wave-propagating media forms an acoustic power transfer system. According to the Stokes' Law, the larger density of the propagating media material, the smaller the acoustic wave attenuation is [17]. The metallic oil pipe under an oil well could be a proper choice for acoustic wave propagation. There are researches done to develop an acoustic wave guides in the well bores and transfer power using acoustic waves [18]. The acoustic waveguide is made of acoustic fiber which is radially surrounded by a cladding region. The shear wave is excited inside the acoustic wave guide and the energy can be picked up by the receiving transducer.

The design provided by [18] doesn't consider the fact that the pipe structure in the well bore could be discontinuous as the production packer on the pipe disrupts the continuity of the pipe structure. The propagating shear wave inside the pipe will suffer from serious reflection at the location of production packer. Also, impedance matching is

needed to reduce the wave reflection at the interface of transducer and the pipe. The pipe material options are very divergent in the oil industry so such design of acoustic power transfer requires constant re-matching whenever the system is applied to a different pipe material. Therefore, applying acoustic power transfer to the well bore applications faces challenges. Inductive power transfer technique uses a low frequency magnetic field to deliver power and the reactive magnetic field will not be blocked by the discontinuous structure of the metallic pipe. Also, the impedance matching of the coil with the metal core (which is the metal pipe in this case) is not sensitive to the material selection of the metal. Therefore, the inductive power transfer method is more robust than acoustic power transfer when applied to the complicated environment of the oil well.

1.3 Objectives

The objective of this dissertation is to design a wireless power transfer system across the production packer on an oil pipe by means of inductive coupling. We are going to explore the two coil system along a metallic pipe, and analyze the power transfer efficiency by building a circuit and an analytic model. Also, we are going to explore how to improve the wireless power transfer efficiency by adding ferrite materials. In Chapter 2 we are going to consider a circuit models for wireless power transfer and derive power transfer efficiency formulas. In Chapter 3 we use an analytical method to analyze the magnetic coupling between the transmitter and receiver and explore the effect of eddy currents brought by the metallic pipe. In Chapter 4 we apply the analytical and circuit models to the wireless power transfer system on the metallic pipe and show the simulation and experimental results of power transfer efficiency, we will see that the magnetic coupling is affected by the eddy currents induced by the metallic pipe and we

need to improve the design for practical use. In Chapter 5 we improve the wireless power transfer system on the pipe by adding soft ferrite cores to both transmitting and receiving coils and we can see the improvement from the FEM simulation data and experiment results. In Chapter 6, we further improve the wireless power transfer design by adding a soft ferrite layer on the section of metallic pipe between the transmitter and receiver. We will show that the ferrite layer forms a magnetic pathway that concentrates the magnetic flux inside this layer. The magnetic coupling between the coils is greatly enhanced in this way and we are expecting even better power transfer efficiency.

Chapter 2 Circuit Model for Wireless Power Transfer

The working principle of inductive power transfer is to create an inductive magnetic field via a transmitting coil and harvest the reactive magnetic energy by using the inducted electric voltage drop on the receiving coil. While the working principle is only about Faraday's Law, there are other details of the coils that require modeling in order to estimate the power transfer efficiency of the inductive power transfer system. In this chapter, we are going to introduce several circuit models that we use to model and numerically analyze the inductive power transfer system. We will start with a basic circuit model of two coils in a lossless environment, and we gradually add parasitic/distributive components to the model to show the circuit model in practical applications, and we will try to develop CAD formula based on such models to numerically analyze the relation among power transfer efficiency, mutual inductance and eddy current. Finally, we will generalize the circuit models into a matrix form. The matrix model parameters can be directly calculated by FEM simulation and we will derive a power transfer efficiency formula based on the matrix model so that we can evaluate the optimum power transfer efficiency using a commercial FEM simulation package.

2.1 Basic Circuit Model in Lossless Environment

In this model, we assume that the power transmitter and the receiver are in a lossless environment, and that is to say, there is no eddy current loss. Also, we assume that the operating frequency is low enough so that the distributive effect can be neglected. In this case, we model the coils as inductors in series with resistors, and the equivalent circuit model is given in Figure 2-1.

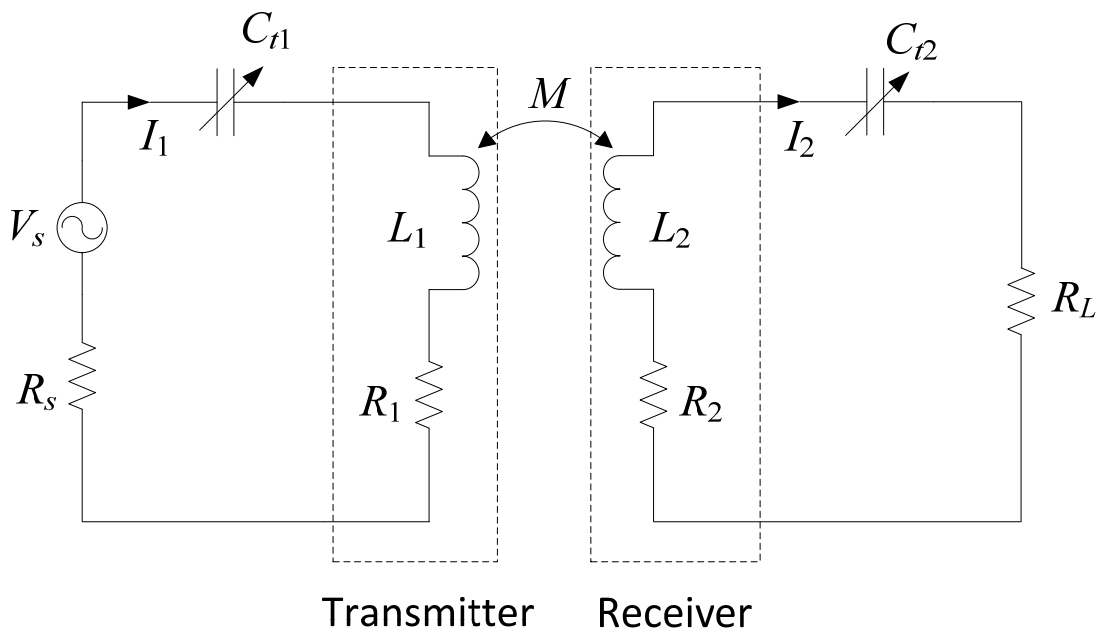

Figure 2-1. The basic circuit model of inductive power transfer in lossless environment

For each component shown in Figure 2-1, there are corresponding physical characteristics related to the coils. The nomenclature of the circuit model in Figure 2-1 is given in Table 2-1. Based on this circuit model, we are going to derive the power transfer efficiency formula. We first assume that the tuning capacitors are resonant with the coil inductors. Then, we adjust the load resistance to obtain the maximum power output. Applying this procedure will not obtain the best power transfer efficiency, as the procedure is not the same with obtaining the extrema of the power transfer efficiency with frequency and load resistance as variables. In weak coupling limit (the concept of which will be shown below), the power transfer efficiency following the above procedure is approaching to the optimal power transfer efficiency. Beyond this limit, the efficiency obtained is not optimal result, but very close to the theoretical maxima of the power transfer efficiency.

Table 2-1. Nomenclature of the Basic Circuit Model in Lossless Environment.

L_1	Transmitter coil inductance
L_2	Receiver coil inductance
R_1	Transmitter coil resistance
R_2	Receiver coil resistance
C_{t1}	Tuning capacitor of the transmitter
C_{t2}	Tuning capacitor of the receiver
M	Mutual inductance
V_s	Power source voltage
R_s	Power source resistance
R_L	Power load resistance
I_1	Current on the transmitter
I_2	Current on the receiver

The tuning capacitors are used to compensate the reactive part of the coil so that the maximum current can be obtained on the primary coil. Also, the tuning capacitor is used on secondary coil for impedance matching to ensure maximum power output on the load resistor. Now, we build circuit equations using Kirchhoff's voltage law, which are given by

$$-V_s + \left(\frac{1}{j\omega C_{t1}} + j\omega L_1 + R_1 + R_s \right) I_1 - j\omega M I_2 = 0 \tag{2-1}$$

and

$$\left(\frac{1}{j\omega C_{t2}} + j\omega L_2 + R_2 + R_L\right) I_2 - j\omega M I_1 = 0. \tag{2-2}$$

We assume that the tuning capacitors of both coils compensate the reactive part of the coil impedance totally, and that is to say

$$\omega = \frac{1}{\sqrt{L_1 C_{t1}}} = \frac{1}{\sqrt{L_2 C_{t2}}}. \tag{2-3}$$

Substituting (2-3) into (2-1) and (2-2), the circuit equations become

$$-V_s + \left(R_1 + R_s\right) I_1 - j\omega M I_2 = 0 \tag{2-4}$$

and

$$\left(R_2 + R_L\right) I_2 - j\omega M I_1 = 0. \tag{2-5}$$

The input power of the voltage source is defined as

$$P_{in} = \mathrm{Re}\left\{\frac{1}{2} V_s I_1^*\right\}. \tag{2-6}$$

The output power on the resistive power load is given as

$$P_{out} = \frac{1}{2}\left|I_2\right|^2 R_L. \tag{2-7}$$

Based on (2-6) and (2-7), we define the power transfer efficiency as

$$e_T = \frac{P_{in}}{P_{out}}. \tag{2-8}$$

Combining (2-4) − (2-8), we obtain the power transfer efficiency of the system as

$$e_T = \frac{1}{1 + \frac{R_2}{R_L} + \frac{\left(R_1 + R_s\right)\left(R_2 + R_L\right)^2}{\left(\omega M\right)^2 R_L}}. \tag{2-9}$$

When we are analyzing the inductive power transfer efficiency, we only want to consider the power loss from the coils for the simplicity reason. So, in this chapter, we assume that

the power source is the ideal voltage source, and R_s is equal to zero. Therefore, the previous equation reduces to

$$e_T = \frac{1}{1 + \frac{R_2}{R_L} + \frac{R_1 \left(R_2 + R_L\right)^2}{\left(\omega M\right)^2 R_L}}. \tag{2-10}$$

According to the magnetic coupling condition, we have two different ways to determine the value of R_L for maximum system efficiency. One is weak coupling condition; the other is strong coupling condition.

2.2 Weak Coupling and Strong Coupling

In inductive power transfer, the weak coupling condition is defined as

$$\left(\omega M\right)^2 << R_1 R_2. \tag{2-11}$$

In this coupling condition, the magnetic field induced by the receiving coil is very small compared to the magnetic field generated by the transmitting coil. Such condition applies to the situation when the distance between power transmitter and receiver is very large. It is reasonable to assume that the current on the transmitting coil is not related to that on the receiving coil. In this case, we only need to have the load resistor equal to the Thevenin resistance of the receiving coil, which means

$$R_2 = R_L. \tag{2-12}$$

Therefore, (2-10) becomes

$$e_T = \frac{1}{2 + 4\frac{R_1 R_2}{\left(\omega M\right)^2}}. \tag{2-13}$$

The efficiency formula given by (2-13) is the power transfer efficiency in lossless environment under the **weak coupling** condition.

For inductive power transfer system, we could let the transmitter and receiver be very close to each other. In this case, the coupling condition becomes

$$(\omega M)^2 \approx R_1 R_2 \text{ or } (\omega M)^2 >> R_1 R_2. \tag{2-14}$$

We categorize such coupling condition as **strong coupling** condition, and we need to consider the relation between the transmitting coil current and the receiving coil current. The discussion of arbitrary coupling condition (both weak and strong) has been given in [19]. According to [19], the optimum load resistance in strong coupling condition is given by

$$R_L^{opt} = R_2 \sqrt{1 + \frac{(\omega M)^2}{R_1 R_2}}. \tag{2-15}$$

Correspondingly, the maximum power efficiency is

$$e_T^{opt} = \left(1 + \frac{2R_1 R_2}{(\omega M)^2} + 2\sqrt{\frac{R_1 R_2}{(\omega M)^2} + \frac{R_1^2 R_2^2}{(\omega M)^4}} \right)^{-1}. \tag{2-16}$$

The efficiency formula given by (2-16) applies to both strong and weak coupling condition. As a matter of fact, if we impose the condition of (2-11), then we have

$$\begin{aligned} e_T^{opt} &= \left(1 + \frac{2R_1 R_2}{(\omega M)^2} + 2\sqrt{\frac{R_1 R_2}{(\omega M)^2} + \frac{R_1^2 R_2^2}{(\omega M)^4}} \right)^{-1} \\ &= \left(1 + \frac{2R_1 R_2}{(\omega M)^2} + 2\frac{R_1 R_2}{(\omega M)^2}\sqrt{1 + \frac{(\omega M)^2}{R_1 R_2}} \right)^{-1} \\ &\sim \left(1 + \frac{2R_1 R_2}{(\omega M)^2} + 2\frac{R_1 R_2}{(\omega M)^2}\left(1 + \frac{(\omega M)^2}{2R_1 R_2} \right) \right)^{-1} \\ &= \left(2 + \frac{4R_1 R_2}{(\omega M)^2} \right)^{-1}. \end{aligned} \tag{2-17}$$

Therefore, assuming the weak coupling condition, the efficiency formula of arbitrary coupling condition reduces back to weak coupling efficiency formula given by (2-13).

In this basic circuit model, both efficiency formula (2-13) and (2-16) show that the power transfer efficiency can be improved in three different ways:

1. Decrease the ohmic loss of the coils;
2. Increase the mutual inductance between the coils;
3. Increase the operating frequency.

In the following section, we will consider practical model of inductive power transfer for oil well applications, and in this model, the ohmic loss due to eddy current is inevitable. In a lossless environment, increasing the operating frequency can increase the power transfer efficiency when frequency is not high enough to make the coil radiation effect significant, as the radiation effect is also regarded as power loss to the stored reactive magnetic energy. In a lossy environment, increasing the operating frequency might also enhance the eddy current effect and weaken the magnetic flux link between the transmitter and receiver (which means in lossy environment, M will decrease when the operating frequency becomes larger). By proper parameter adjustment, we could obtain a combination of frequency, coil dimension and turns so that an optimum efficiency can be reached in a relative manner. Such an approach is still limited by the eddy current effect of the environment, and we still need to build a magnetic flux pathway in order to greatly increase the mutual inductance of the two coil system.

2.3 Circuit Model in Lossy Environment

2.3.1 Building the Circuit Model in Lossy Environment

In a lossy environment, we need to take the eddy current effect into account. Also, in this circuit model of a lossy environment, we consider the parasitic capacitance of the transmitting and the receiving coils. We build a circuit model that regards the eddy current effect and the stray capacitance effect as additional lump components placed into the circuit model in Figure 2-1, and this circuit model is given in Figure 2-2.

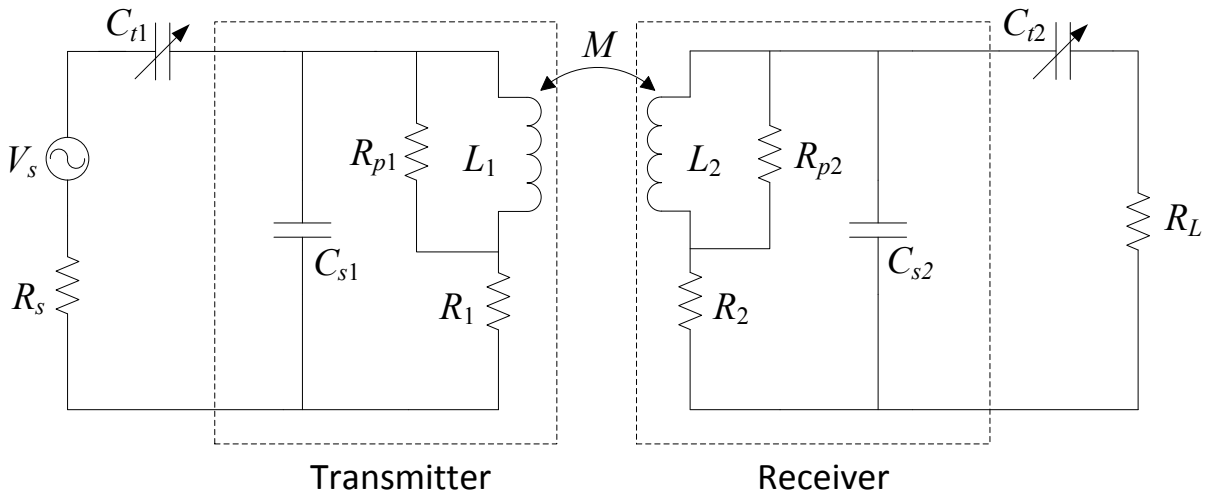

Figure 2-2. Circuit model for inductive power transfer in lossy environment.

In Figure 2-2, we add capacitors (C_{s1} and C_{s2}) parallel to the coils to model the stray capacitance. We add shunt resistors (R_{p1} and R_{p2}) parallel to the coil inductance to model the eddy current loss. We develop the circuit model based on the RLGC model of transmission line. The coils can be regarded as a section of twisted, short-ended transmission line. From the transmission line point of view, the stray capacitance is analogous to the distributive capacitance (C) between single solid wires on the transmission line, and the eddy current loss is similar to the dielectric loss (G) in the

transmission line model [20]. In the transmission line model, both distributive capacitance and dielectric loss conductance are placed across the transmission line in one segment, and if the segment length is far lesser than the wavelength, the sequence of these distributed elements is arbitrary. Similarly, the position of the shunt resistors for the eddy current loss can be either across the coil inductors or parallel to the stray capacitance. These are just two possible ways to model the distributive effect of lossy environment via circuit structure. The alternative circuit model based on the discussion above is given in Figure 2-3.

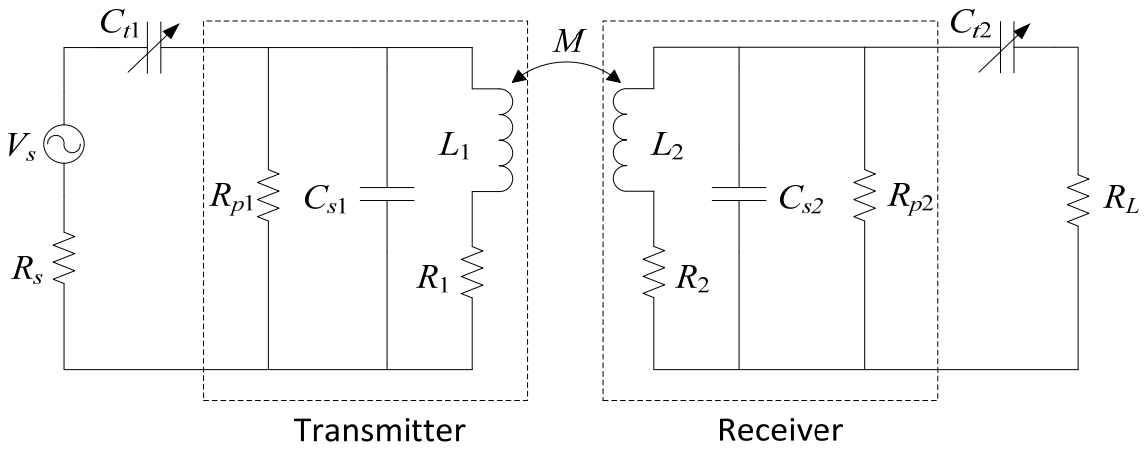

Figure 2-3. Alternative circuit model for inductive power transfer in lossy environment.

2.3.2 The Derivation of Power Transfer Efficiency

Though both models given by Figure 2-2 and Figure 2-3 are valid, the one in Figure 2-2 is easier for efficiency analysis. In this section we are going to show the derivation of power transfer efficiency formula based on the lossy environment circuit model in Figure 2-2. We rearrange the circuit and separate the components into four parts, which are given in Figure 2-4.

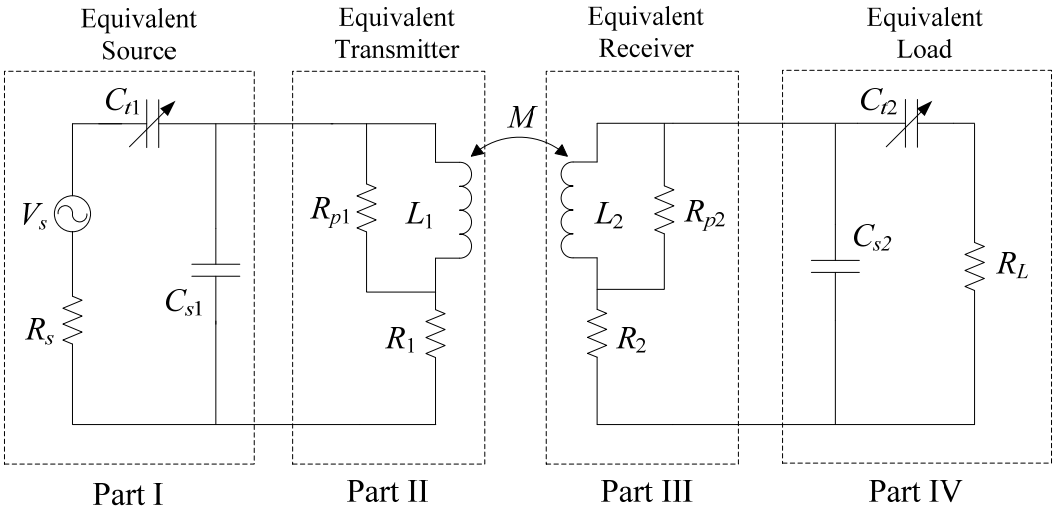

Figure 2-4. Circuit model of inductive power transfer with rearranged modules.

In this circuit model, we take stray capacitance (C_{s1} and C_{s2}) out of the coil circuits and merge them into source and load, as a part of the impedance matching network. At a certain operational frequency, we adjust the tuning capacitor so that the capacitive part of the equivalent source/load compensates the inductive part of the equivalent transmitter/receiver, and we ensure the maximum current on the transmitter and the maximum power output on the equivalent power load. Still, we only consider the power loss on the transmitting and receiving coils so we assume that R_s equals to zero. If we define the power dissipated on Part II, III and IV as P_{II}, P_{III} and P_{IV}, then the power transfer efficiency of the system is defined as

$$e_T = \frac{P_{\mathrm{IV}}}{P_{\mathrm{II}} + P_{\mathrm{III}} + P_{\mathrm{IV}}}. \tag{2-18}$$

The equivalent impedance of Part II is

$$Z_{\mathrm{II}} = R_1 + \frac{R_{p1}}{1 + \left(R_{p1} / (\omega L_1)\right)^2} + \frac{j\omega L_1}{1 + \left((\omega L_1) / R_{p1}\right)^2}. \tag{2-19}$$

If we denote I_{R1} as the current on resistor R_1, then the power dissipated on part II is

$$P_{\mathrm{II}} = \frac{1}{2}\left|I_{R1}\right|^2 \left(R_1 + \frac{R_{p1}}{1+\left(R_{p1}/\left(\omega L_1\right)\right)^2} \right). \tag{2-20}$$

From the equivalent load (Part IV) point of view, the equivalent receiver (Part III) is a Thevenin voltage source, and the Thevenin voltage is given as

$$V_{\mathrm{III}}^{th} = \frac{R_{p2}}{R_{p2} + j\omega L_2}\left(j\omega M I_{L1}\right). \tag{2-21}$$

In (2-21), we denote I_{L1} as the current on the transmitting coil inductor. The mutual inductance M represents the magnetic coupling between the inductor L_1 and L_2. The Thevenin impedance of Part III is

$$V_{\mathrm{III}}^{th} = R_2 + \frac{R_{p2}}{1+\left(R_{p2}/\left(\omega L_2\right)\right)^2} + \frac{j\omega L_2}{1+\left(\left(\omega L_2\right)/R_{p2}\right)^2}. \tag{2-22}$$

Under weak coupling condition, we obtain maximum power output on the load when the load of Part IV reach conjugate match with the Thevenin impedance of Part III, and that to say, the impedance of the equivalent load is

$$Z_{\mathrm{IV}} = \left(Z_{\mathrm{III}}^{th}\right)^* = R_2 + \frac{R_{p2}}{1+\left(R_{p2}/\left(\omega L_2\right)\right)^2} - \frac{j\omega L_2}{1+\left(\left(\omega L_2\right)/R_{p2}\right)^2}. \tag{2-23}$$

The conjugate match can be reached by adjusting the load resistance and the tuning capacitance on the secondary coil, and the matched load will dissipate the same amount of power as the equivalent receiver. Overall, the power dissipated on the secondary coil is

$$P_2 = P_{\mathrm{III}} + P_{\mathrm{IV}} = \frac{\left|V_{\mathrm{III}}^{th}\right|^2}{4\,\mathrm{Re}\left\{Z_{\mathrm{IV}}\right\}}. \tag{2-24}$$

Substituting (2-22) and (2-23) into (2-24), the dissipated power becomes

$$P_2 = \frac{(\omega M)^2 R_{p2}^2 \left| I_{L_1} \right|^2}{4\left(R_{p2}^2 + \omega^2 L_2^2\right)\left(R_2 + \dfrac{R_{p2}}{1+\left(R_{p2}/(\omega L_2)\right)^2} \right)}. \tag{2-25}$$

As the matched load and the equivalent receiver dissipates the same amount of power,

$$P_{\mathrm{III}} = P_{\mathrm{IV}} = \frac{1}{2} P_2. \tag{2-26}$$

Also, the relation of I_{R1} and I_{L1} is given by

$$\frac{I_{R_1}}{I_{L_1}} = \frac{j\omega L_1 + R_{p1}}{R_{p1}}. \tag{2-27}$$

Substituting (2-20), (2-25), (2-26) and (2-27) into (2-18), we finally obtain the efficiency formula as

$$e_T = \frac{1}{4\left(1+\left(\dfrac{\omega L_1}{R_{p1}}\right)^2\right)\left(1+\left(\dfrac{\omega L_2}{R_{p2}}\right)^2\right)\left(R_1 + \dfrac{R_{p1}}{1+\left(\dfrac{R_{p1}}{\omega L_1}\right)^2} \right)\left(R_2 + \dfrac{R_{p2}}{1+\left(\dfrac{R_{p2}}{\omega L_2}\right)^2} \right)}{2 + \dfrac{}{(\omega M)^2}}. \tag{2-28}$$

This formula is complicated with many repeated details so we rearrange the math expression given by

$$e_T = \frac{1}{2 + 4A_1A_2B_1B_2/(\omega M)^2}, \tag{2-29}$$

in which

$$A_i = 1 + (\omega L_i)^2 / R_{pi} \ (i = 1, 2), \tag{2-30}$$

and

$$B_i = R_i + \frac{R_{pi}}{1+\left(R_{pi}/\left(\omega L_i\right)\right)^2}\ \left(i=1,2\right). \tag{2-31}$$

Similar to the RLGC model in transmission line theory, a larger R_p means smaller eddy current loss. In fact, when R_p approaches to infinity (which represents an almost lossless environment), we have

$$A_i \sim 1\ \left(i=1,2\right), \tag{2-32}$$

$$B_i \sim R_i\ \left(i=1,2\right), \tag{2-33}$$

and

$$e_T \sim \frac{1}{2+4R_1R_2/\left(\omega M\right)^2}. \tag{2-34}$$

So, the lossy environment model reduces back to lossless model.

2.3.3 Eddy Current Effect in Lossy Environment

From the circuit formula above, we can see that eddy current brought two negative effects to the wireless power transfer system. First of all, it weakens the magnetic coupling between the transmitter and receiver as the shunt resistors modeling the eddy current will consume part of the input current which is supposed to be on the coil inductors. Also, the current on the shunt resistor is dissipated as ohmic loss and therefore the overall power transfer efficiency is lowered.

The advantage of circuit model is that we could lump all distributive effects into this circuit structure and analyze their effect to the power transfer efficiency via a CAD formula. However, it is difficult to link the circuit model with FEM simulation data and experimental results. What we can extract from both simulation and experiment are Thevenin voltage and impedance, and it is clumsy to calculate all circuit components via

equations built by them. Therefore, we generalize the circuit model into an impedance matrix, and we use the matrix model to estimate power transfer efficiency from FEM simulation data and experiment.

2.4 Matrix Model for Inductive Power Transfer

2.4.1 Building the Matrix Model

The matrix model treats the two coil system as an impedance matrix. Such model has been applied to radiative wireless power transfer [21]. In this dissertation, we use the low frequency approximation of the impedance matrix model to investigate the wireless power transfer in lossy environment. The graphic illustration of the matrix model for inductive power transfer is given in Figure 2-5.

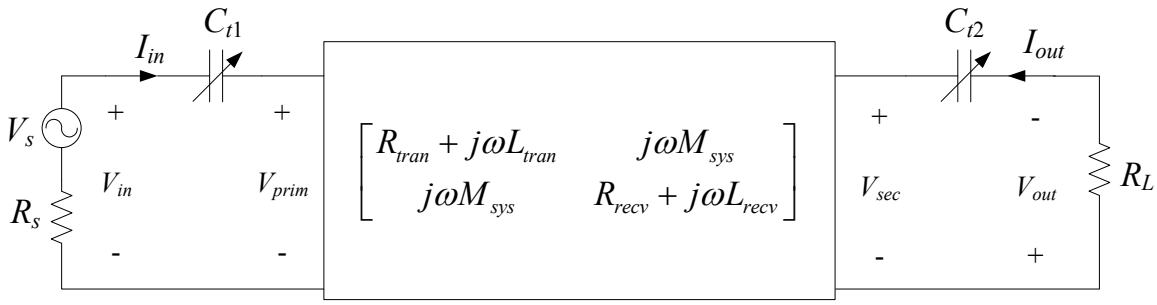

Figure 2-5. The matrix model of the inductive power transfer system.

In this matrix model, we directly model the two coil system using the equivalent impedance of the coils. The input impedances of each coil are given as

$$\left.\frac{V_{prim}}{I_{in}}\right|_{I_{out}=0} = R_{tran} + j\omega L_{tran} \tag{2-35}$$

and

$$\left.\frac{V_{sec}}{I_{out}}\right|_{I_{in}=0} = R_{recv} + j\omega L_{recv}. \tag{2-36}$$

The mutual inductance M is calculated by the open circuit voltage on the secondary coil and the input current on the primary coil. The calculation is given by

$$M = \left. \frac{V_{sec}}{j\omega I_{in}} \right|_{I_{out}=0}. \tag{2-37}$$

In oil well applications, the two coil system is installed on the metallic oil pipe. The eddy current effect of the oil pipe not only affects the magnitude of the parameter M, but also gives it a phase angle, making it a complex number.

2.4.2 Deriving the Power Transfer Efficiency Formula for Matrix Model

In this section, we show the mathematic derivation of the efficiency formula from the matrix model (given in Figure 2-5). The result and the derivation process will be very similar to that of lossless case (Section 2.1), but the resistive element of the matrix includes the eddy current effect in a lossy environment, which gives the formula a different application background. The matrix form of the two coil system is given by

$$\begin{bmatrix} V_{prim} \\ V_{sec} \end{bmatrix} = \begin{bmatrix} j\omega L_{tran} + R_{tran} & j\omega M_{sys} \\ j\omega M_{sys} & j\omega L_{recv} + R_{recv} \end{bmatrix} \begin{bmatrix} I_{in} \\ I_{out} \end{bmatrix}. \tag{2-38}$$

The input voltage V_{in} is the sum of the voltage on both tuning capacitors and the coil, the same for the output voltage V_{out}. The overall system equations are

$$V_{in} = \left(\frac{1}{j\omega C_{t1}} + j\omega L_{tran} + R_{tran} \right) I_{in} + j\omega M_{sys} I_{out} \tag{2-39}$$

and

$$j\omega M_{sys} I_{in} + \left(R_{recv} + R_L + \frac{1}{j\omega C_{t2}} + j\omega L_{recv} \right) I_{out} = 0. \tag{2-40}$$

We adjust the tuning capacitors till they totally compensate the reactive part of the coil impedances, and the equations become

$$V_{in} = R_{tran} I_{in} + j\omega M_{sys} I_{out} \tag{2-41}$$

and

$$j\omega M_{sys} I_{in} + \left(R_{recv} + R_L \right) I_{out} = 0. \tag{2-42}$$

The input power is of the system is defined as

$$P_{in} = \frac{1}{2} \mathrm{Re}\left\{ V_{in} I_{in}^{*} \right\}. \tag{2-43}$$

Combining these three equations above, we derive the input power as

$$P_{in} = \frac{1}{2} \left[R_{tran} + \frac{\omega^2 \left(\mathrm{Re}\left\{ M_{sys} \right\}^2 - \mathrm{Im}\left\{ M_{sys} \right\}^2 \right)}{R_{recv} + R_L} \right] \left| I_{in} \right|^2. \tag{2-44}$$

The output power on the load is given by

$$P_{out} = \frac{1}{2} \left| I_{out} \right|^2 R_L. \tag{2-45}$$

Also, we arrange (2-42) as

$$\left| \frac{I_{out}}{I_{in}} \right|^2 = \frac{\left| \omega M_{sys} \right|^2}{\left(R_{recv} + R_L \right)^2}. \tag{2-46}$$

Then, we calculate the power transfer efficiency as

$$e_T = \frac{P_{out}}{P_{in}} = \frac{1}{\left(1 + \frac{R_{recv}}{R_L} \right) \frac{\mathrm{Re}\left\{ M_{sys} \right\}^2 - \mathrm{Im}\left\{ M_{sys} \right\}^2}{\left| M_{sys} \right|^2} + \frac{R_{tran} \left(R_{recv} + R_L \right)^2}{R_L \left| \omega M_{sys} \right|^2}}. \tag{2-47}$$

In this research, we are trying to reduce the eddy current effect by adding a ferrite material structure to the inductive power system. So, in our design, the imaginary part of the mutual inductance is supposed to be much smaller than the real part, and we can reduce the efficiency formula as

$$e_T = \frac{P_{out}}{P_{in}} = \frac{1}{1 + \frac{R_{recv}}{R_L} + \frac{R_{tran}\left(R_{recv} + R_L\right)^2}{R_L \left|\omega M_{sys}\right|^2}}. \tag{2-48}$$

This result is analogous to (2-10), and it is valid for arbitrary coupling condition. If we match the load with the Thevenin impedance of the secondary coil (R_{recv}), then the efficiency formula becomes

$$e_T = \frac{1}{2 + 4\frac{R_{tran}R_{recv}}{\left|\omega M_{sys}\right|^2}}. \tag{2-49}$$

This impedance matching approach ensures maximum output power under weak coupling. In strong coupling, however, the efficiency given by (2-49) will not exceed 50% no matter how strong the magnetic flux link is. This is because the efficiency in above formula is obtained when the load resistor equals the Thevenin resistance of the secondary coil, which means

$$R_L = R_{recv}. \tag{2-50}$$

Similar to the derivation shown in Section 2.1, the derivation shown above obtains the optimum power transfer efficiency in the weak coupling limit but the result is not the theoretical maximum power transfer efficiency under the strong coupling condition. It is a second best solution but the efficiency is very close to the maximum limit. Under strong coupling condition, the optimum load for maximum efficiency is given as

$$R_L^{opt} = R_{recv}\sqrt{1 + \frac{\left|\omega M\right|^2}{R_{tran}R_{recv}}}. \tag{2-51}$$

The derivation of (2-51) is similar to (2-15). The correspondingly optimized efficiency is given as

$$e_T^{opt} = \left(1 + 2\eta + 2\sqrt{\eta + \eta^2}\right)^{-1}, \tag{2-52}$$

in which

$$\eta = \frac{R_1 R_2}{\left|\omega M\right|^2}. \tag{2-53}$$

The disadvantage of using (2-50) to perform impedance matching is that the efficiency will never exceed 50%. In experiments, however, the matching procedure indicated by (2-50) is easy to be implemented so in this research we use (2-50) to validate simulation data via experiments. Also, it is difficult to implement a load resistor with exactly the same value as the Thevenin coil resistance or any desired value calculated by CAD formulas. CAD formulas are predicting the best efficiency we can obtain given the ideal impedance matching condition. In actual experiment, however, we are expecting the experimental results to be lower than these optimum values. What we will do is to try our best to emulate the ideal impedance matching indicated by the given CAD formulas so that the experiment and simulation data will be as close as possible.

2.4.3 The Matrix Model and FEM Simulation

The advantage of the matrix model is that it directly makes use of the data obtained by FEM simulation and experiment. The ANSYS Maxwell 2D/3D eddy current solver is able to extract the impedance matrix from the FEM field solution, and we can use the impedance data to numerically estimate the power transfer efficiency by the matrix model formula. In this dissertation we use ANSYS Maxwell 2D eddy current solver specifically, but the matrix model we have developed in this chapter can be applied to any FEM simulation software package. FEM simulation software calculates the field distribution of the two-coil model along pipe with the current excitation on the

primary coil. Then, the input resistance of the primary coil and secondary coil are given by

$$R_{tran} = \left. \frac{\int_V \frac{1}{\sigma} |\boldsymbol{J}|^2 \, dV}{|I_{in}|} \right|_{I_{out}=0} \tag{2-54}$$

and

$$R_{recv} = \left. \frac{\int_V \frac{1}{\sigma} |\boldsymbol{J}|^2 \, dV}{|I_{out}|} \right|_{I_{in}=0} . \tag{2-55}$$

The integral domain V includes all the lossy subjects in the FEM model, which are coils, metallic pipes and the lossy environment. We can see that R_{tran} and R_{recv} take eddy current effect of lossy subjects into consideration. The mutual inductance between the transmitting and receiving coils is given by

$$M_{sys} = \left. \frac{\sum_{\text{All turns}} \int_{S_2} \boldsymbol{B} \cdot \boldsymbol{dS}}{I_{in}} \right|_{I_{out}=0} = \left. \frac{\sum_{\text{All turns}} \int_{C_2} \boldsymbol{E} \cdot \boldsymbol{dl}}{j\omega I_{in}} \right|_{I_{out}=0} . \tag{2-56}$$

The integral domain S_2 is the coil area for each turn on the secondary coil and C_2 is the coil contour for each turn. We add the integral results for each turns on the receiver to obtain the overall mutual inductance. Therefore, we can extract the parameters of the matrix model that we need to evaluate the optimum power transfer efficiency.

Chapter 3 Analytical Model for Wireless Power Transfer

In this chapter, we are going to build an analytical model for the wireless power transfer system along the metallic pipe. We will start with the most fundamental model with two single loop coils in the lossless open space, and then we add a metallic pipe structure to the model and discuss the effects brought by the pipe. Furthermore, we add a layer of material with high permeability which radially surrounding the metallic pipe and explore the mutual coupling between the transmitting and the receiving coils.

3.1 Basic Model in the Lossless Open Space

We start with the basic model having two single loop coils in lossless open space. In this model, we assume that the transmitter and receiver are coaxially aligned and they share the same coil radius, which is shown in Figure 3-1.

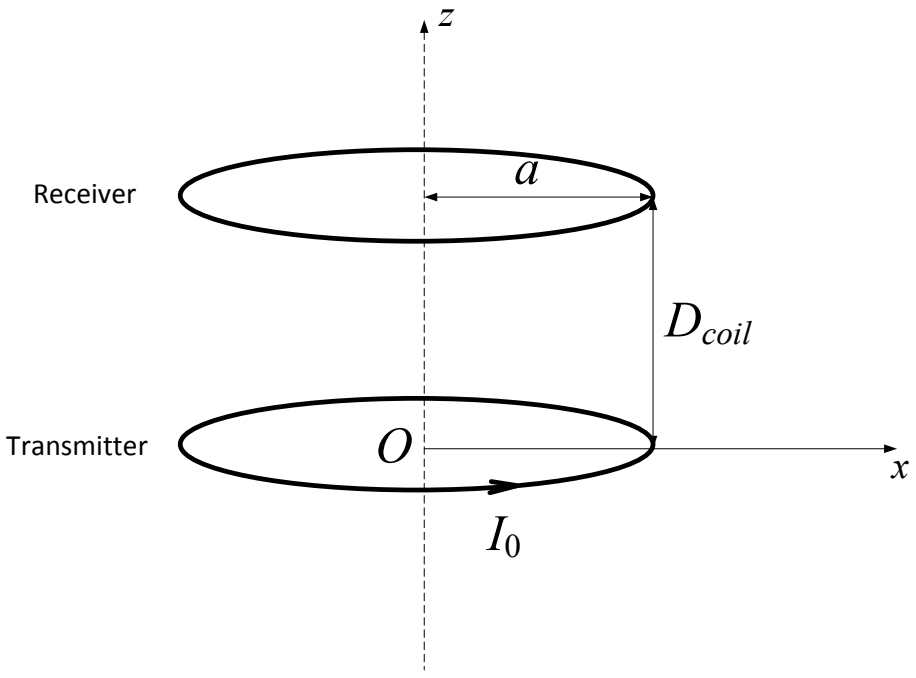

Figure 3-1. The basic analytical model with loop coils in the lossless open space.

In Figure 3-1, parameter a is the radius of the transmitting and the receiving coil. For this fundamental model, the mutual inductance between the coils can be given by a standard formula consisting of complete elliptic integrals [22]. The mutual inductance is given by

$$M_{sys} = \mu_0 a\left[\left(\frac{2}{k}-k\right)K(k)-\frac{2}{k}E(k)\right], \tag{3-1}$$

in which

$$k = \frac{2a}{\sqrt{D_{coil}^2+4a^2}}, \tag{3-2}$$

$$E(k) = \int_0^{\pi/2}\sqrt{1-k^2\sin^2\phi}\,d\phi, \tag{3-3}$$

and

$$K(k) = \int_0^{\pi/2}\frac{d\phi}{\sqrt{1-k^2\sin^2\phi}}. \tag{3-4}$$

This standard formula assumes DC current on the primary coil. For our application, we need to take the frequency of the current into consideration. In this dissertation, we use the spectral domain method to calculate the fields induced by the primary coil. Also, we assume that the frequency of the primary coil current is not high enough to show a distributive effect, and the current distribution on the coil can be regarded as uniform. In this case, the field excited by the primary coil current is transverse electric to z direction (TE_z), and the vector electric potential $\boldsymbol{F}$ only has z-direction component $\boldsymbol{F_z}$, which satisfies the Helmholtz equation [23]. In this model, we assume the environment is air and the Helmholtz equation for $\boldsymbol{F_z}$ in air region is given by

$$\nabla^2 F_z + k_0^2 F_z = 0, \tag{3-5}$$

in which

$$k_0 = \omega\sqrt{\mu_0\varepsilon_0}. \tag{3-6}$$

The parameter k_0 in (3-6) is the wavenumber in air. We divide the space into two regions, one is $\rho < a$, and the other is $\rho > a$. The fields in the open space are entirely the incident field generated by the primary coil. Accordingly we write the electric potential of the fields as

$$F_{z0}^{inc}\Big|_{\rho<a} = \int_{-\infty}^{+\infty} A(k_z) J_0\left(k_{\rho 0}\rho\right) e^{-jk_z z} dk_z \tag{3-7}$$

and

$$F_{z0}^{inc}\Big|_{\rho>a} = \int_{-\infty}^{+\infty} B(k_z) H_0^{(2)}\left(k_{\rho 0}\rho\right) e^{-jk_z z} dk_z. \tag{3-8}$$

In these two equations, k_z and k_ρ are wave numbers in the on spectral domain. The relation of these three wavenumbers is

$$k_{\rho 0}^2 + k_z^2 = k_0^2. \tag{3-9}$$

The electric fields in such a TE model only have a ϕ component, and the electric fields are calculated as

$$E_{\phi 0}^{inc}\Big|_{\rho<a} = \frac{1}{\varepsilon}\frac{\partial F_{z0}^{inc}}{\partial\rho}\Big|_{\rho<a} = \frac{1}{\varepsilon}\int_{-\infty}^{+\infty} k_{\rho 0} A(k_z) J_0'\left(k_{\rho 0}\rho\right) e^{-jk_z z} dk_z \tag{3-10}$$

and

$$E_{\phi 0}^{inc}\Big|_{\rho>a} = \frac{1}{\varepsilon}\frac{\partial F_{z0}^{inc}}{\partial\rho}\Big|_{\rho>a} = \frac{1}{\varepsilon}\int_{-\infty}^{+\infty} k_{\rho 0} B(k_z) H_0^{(2)'}\left(k_{\rho 0}\rho\right) e^{-jk_z z} dk_z. \tag{3-11}$$

At the boundary where $\rho = b$, the electric field is continuous, so

$$A(k_z) J_0'\left(k_{\rho 0}a\right) = B(k_z) H_0^{(2)'}\left(k_{\rho 0}a\right). \tag{3-12}$$

Similarly, we calculate the magnetic field in the air region as

$$H_z^{inc}\Big|_{\rho<a} = \frac{1}{j\omega\mu_0\varepsilon_0}\left(\frac{\partial^2}{\partial z^2}+k^2\right)F_{z0}^{inc}\Big|_{\rho<a}$$
$$= \frac{1}{j\omega\mu_0\varepsilon_0}\int_{-\infty}^{+\infty} k_\rho^2 A(k_z) J_0\left(k_{\rho 0}\rho\right)e^{-jk_z z}dk_z \tag{3-13}$$

and

$$H_z^{inc}\Big|_{\rho>a} = \frac{1}{j\omega\mu_0\varepsilon_0}\left(\frac{\partial^2}{\partial z^2}+k^2\right)F_{z2}^{inc}$$
$$= \frac{1}{j\omega\mu_0\varepsilon_0}\int_{-\infty}^{+\infty} k_\rho^2 A(k_z) H_0^{(2)}\left(k_{\rho 0}\rho\right)e^{-jk_z z}dk_z. \tag{3-14}$$

Again, on the boundary where $\rho = b$, the coil current is regarded as a filament, so the current density on the boundary is

$$\boldsymbol{J_s} = \delta(z)\hat{\phi}. \tag{3-15}$$

The boundary condition for the magnetic field is then given by

$$H_{z0}^{inc}\Big|_{\rho\to a^-} - H_{z0}^{inc}\Big|_{\rho\to a^+} = \delta(z). \tag{3-16}$$

Next, we expand the Dirac function in the spectral domain as

$$\delta(z) = \frac{1}{2\pi}\int_{-\infty}^{+\infty} e^{-jk_z z}dk_z. \tag{3-17}$$

Substituting (3-13), (3-14) and (3-17) into (3-16), we obtain another equation for the boundary condition as

$$A\left(k_z\right)J_0\left(k_{\rho 0}a\right) - B\left(k_z\right)H_0^{(2)}\left(k_{\rho 0}a\right) = \frac{j\omega\mu_0\varepsilon_0}{2\pi k_{\rho 0}^2}. \tag{3-18}$$

Combining (3-12) and (3-18) using the Wronskian identity, we solve for the unknown function $A(k_z)$ and $B(k_z)$ as

$$A\left(k_z\right) = \frac{\omega\mu_0\varepsilon_0 a}{4k_\rho}H_1^{(2)}\left(k_{\rho 0}a\right) \tag{3-19}$$

and

$$B\left(k_z\right)=\frac{\omega\mu_0\varepsilon_0 a}{4k_\rho}J_1\left(k_{\rho 0}a\right). \tag{3-20}$$

Hence, we can write the incident field as

$$F_z^{inc}\Big|_{\rho<a}=\int_{-\infty}^{+\infty}\frac{\omega\mu_0\varepsilon_0 a}{4k_{\rho 0}}H_1^{(2)}\left(k_{\rho 0}a\right)J_0\left(k_{\rho 0}\rho\right)e^{-jk_z z}dk_z \tag{3-21}$$

and

$$F_z^{inc}\Big|_{\rho>a}=\int_{-\infty}^{+\infty}\frac{\omega\mu_0\varepsilon_0 a}{4k_{\rho 0}}J_1\left(k_{\rho 0}a\right)H_0^{(2)}\left(k_{\rho 0}\rho\right)e^{-jk_z z}dk_z. \tag{3-22}$$

Therefore, the incident electric field is given as

$$E_\phi^{inc}\Big|_{\rho<a}=-\frac{\omega\mu_0 a}{4}\int_{-\infty}^{+\infty}H_1^{(2)}\left(k_{\rho 0}a\right)J_1\left(k_{\rho 0}\rho\right)e^{-jk_z z}dk_z \tag{3-23}$$

and

$$E_\phi^{inc}\Big|_{\rho>a}=-\frac{\omega\mu_0 a}{4}\int_{-\infty}^{+\infty}J_1\left(k_{\rho 0}a\right)H_1^{(2)}\left(k_{\rho 0}\rho\right)e^{-jk_z z}dk_z. \tag{3-24}$$

Then, we can calculate the mutual inductance of the two coil system using (2-56), and it is calculated as

$$\begin{aligned}M_{sys}^{inc}&=N_1N_2\left.\frac{\int_{C_2}E_{\phi 2}^{inc}dl}{-j\omega}\right|_{\rho\to a,z=D_{coil}}\\&=-j\frac{\pi a^2\mu_0}{2}\int_{-\infty}^{+\infty}J_1\left(k_{\rho 0}a\right)H_1^{(2)}\left(k_{\rho 0}a\right)e^{-jk_z D_{coil}}dk_z.\end{aligned} \tag{3-25}$$

It is worth mentioning that the minus sign in (3-25) is arbitrary; it depends on the voltage reference direction on the receiving coil. In this dissertation, we choose to keep the minus sign and to be consistent with it in the following formula of mutual inductance.

3.2 Analytical Model with Metallic Pipe

In this section, we analyze the mutual inductance of the two coil system along the metallic pipe using the spectral domain method. Still we consider both of the transmitting and receiving coils as a single turn for simplicity, and we still assume that the transmitting and the receiving coils share the same radius. This model is illustrated in Figure 3-2.

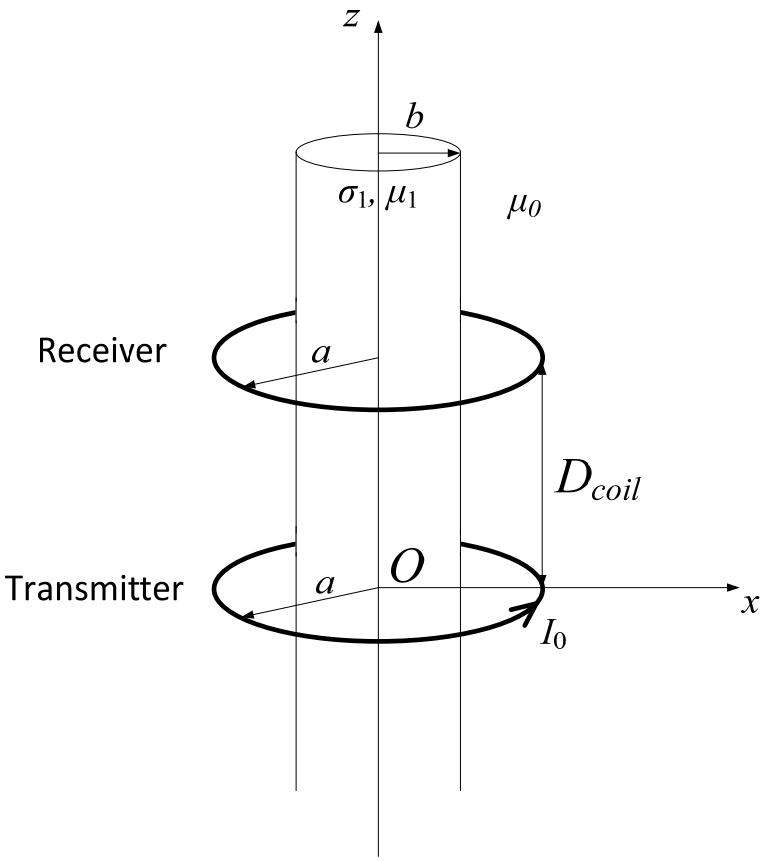

Figure 3-2. The two coil model along the metallic pipe.

We assume that under the desired operating frequency, the skin depth of the metallic pipe is far smaller than the pipe thickness, and we replace the pipe structure with a cylindrical surface impedance boundary and the surface impedance is

$$Z_{s1} = R_{s1}(1+j), \tag{3-26}$$

in which

$$R_{s1} = \frac{1}{\sigma_1 \delta_1} \text{ and } \delta_1 = \sqrt{\frac{2}{\omega \mu_1 \sigma_1}}. \tag{3-27}$$

There will be scattered wave due to the surface impedance boundary. The scattered wave is also transverse electric to the z direction and the vector electric potential of which obeys the Helmholtz equation, so the angularly independent electric potential of the scattered field is given by

$$F_{z0}^{sca} = \int_{-\infty}^{+\infty} C(k_z) H_0^{(2)}(k_{\rho 0}\rho) e^{-jk_z z} dk_z. \tag{3-28}$$

In scattered field, the Hankel function is chosen in the superposition integral since the scattered fields are entirely outgoing. At the pipe surface where $\rho = b$, we have

$$\left.\frac{E_{\phi 0}^{tot}}{H_{z0}^{tot}}\right|_{\rho=b} = -Z_{s1}. \tag{3-29}$$

We apply a similar derivation procedure as given in the incident field calculation, and the scattered electric and magnetic fields are given by

$$E_{\phi 0}^{sca}\Big|_{\rho=b} = \frac{1}{\varepsilon}\left.\frac{\partial F_{z0}^{sca}}{\partial \rho}\right|_{\rho=b} = -\frac{1}{\varepsilon}\int_{-\infty}^{+\infty} k_\rho C(k_z) H_1^{(2)}(k_{\rho 0}a) e^{-jk_z z} dk_z \tag{3-30}$$

and

$$\begin{aligned} H_{z0}^{sca}\Big|_{\rho=b} &= \frac{1}{j\omega\mu_0\varepsilon_0}\left(\frac{\partial^2}{\partial z^2} + k_0^2\right)\int_{-\infty}^{+\infty} C(k_z) H_0^{(2)}(k_{\rho 0}a) e^{-jk_z z} dk_z \\ &= \frac{1}{j\omega\mu_0\varepsilon_0}\int_{-\infty}^{+\infty} k_{\rho 0}^2 C(k_z) H_0^{(2)}(k_{\rho 0}a) e^{-jk_z z} dk_z. \end{aligned} \tag{3-31}$$

On the impedance boundary, the boundary condition equation is given by

$$E_{\phi}^{inc}\Big|_{\rho=b}+E_{\phi 0}^{sca}\Big|_{\rho=b}=-Z_s\left(H_z^{inc}\Big|_{\rho=b}+H_{z0}^{sca}\Big|_{\rho=b}\right). \tag{3-32}$$

Using this boundary condition, we solve for the unknown function $C(k_z)$ as

$$C\left(k_z\right)=\frac{\frac{\omega\mu_0 a}{4}H_1^{(2)}\left(k_{\rho 0}a\right)J_1\left(k_{\rho 0}b\right)-\frac{k_{\rho 0}bZ_{s1}}{4j}H_1^{(2)}\left(k_{\rho 0}a\right)J_0\left(k_{\rho 0}b\right)}{\frac{Z_s k_\rho^2}{j\omega\mu_0\varepsilon_0}H_0^{(2)}\left(k_{\rho 0}b\right)-\frac{k_\rho}{\varepsilon_0}H_1^{(2)}\left(k_{\rho 0}b\right)}. \tag{3-33}$$

Use the results for the incident fields and scattered fields, we give the total electric field in the region where $\rho > b$ as

$$E_{\phi 0}^{tot}=\left(-\frac{\omega\mu_0 a}{4}\right)\int_{-\infty}^{+\infty}F\left(k_{\rho 0}\right)J_1(k_{\rho 0}a)H_1^{(2)}(k_{\rho 0}\rho)e^{-jk_z z}dk_z, \tag{3-34}$$

in which

$$F(k_\rho)=1-\frac{H_1^{(2)}(k_{\rho 0}a)J_1(k_{\rho 0}b)-\left(\frac{Z_{s1}k_{\rho 0}}{j\omega\mu_0}\right)H_1^{(2)}(k_{\rho 0}a)J_0(k_{\rho 0}b)}{H_1^{(2)}(k_{\rho 0}b)J_1(k_{\rho 0}a)-\left(\frac{Z_{s1}k_{\rho 0}}{j\omega\mu_0}\right)H_0^{(2)}(k_{\rho 0}b)J_1(k_{\rho 0}a)}. \tag{3-35}$$

Then, the mutual inductance between the coils is given by

$$\begin{aligned}M_{sys}^{tot}=-N_1N_2\frac{\int_{C_2}E_\phi^{tot}dl}{j\omega}\Bigg|_{\rho\to a,h=D_{coil}}&=-N_1N_2\frac{2\pi aE_\phi^{tot}}{j\omega}\\&=N_1N_2\frac{\mu_0\pi a^2}{2j}\int_{-\infty}^{+\infty}F\left(k_{\rho 0}\right)J_1(k_{\rho 0}a)H_1^{(2)}(k_{\rho 0}a)e^{-jk_zD_{coil}}dk_z.\end{aligned} \tag{3-36}$$

Specifically, if we assume that the metallic pipe is perfectly conducting (which means $\sigma_1 \to \infty$), then the surface impedance of the pipe is approaching to zero ($Z_s \to 0$). In this case, (3-35) is simplified as

$$F^{PEC}(k_\rho)=1-\frac{H_1^{(2)}(k_{\rho 0}a)J_1(k_{\rho 0}b)}{H_1^{(2)}(k_{\rho 0}b)J_1(k_{\rho 0}a)}. \tag{3-37}$$

In [24], Shen gave an asymptotic form of the total electric field for large coil separation at the position of $\rho = a$, but he didn't give a derivation. The asymptotic form of the total electric field given by Shen is

$$E_{\phi 0}^{tot}\Big|_{\rho=a} \sim \left(1-\frac{b^2}{a^2}\right)^2 E_{\phi}^{inc}\Big|_{\rho=a}. \tag{3-38}$$

We are going to give a derivation of (3-38) in the appendix. Correspondingly, the mutual inductance between coils along the PEC pipe can be approximated by

$$M_{sys}^{tot} \sim \left(1-\frac{b^2}{a^2}\right)^2 M_{sys}^{inc}. \tag{3-39}$$

Though the asymptotic formula of mutual inductance above is derived under the assumption that the pipe is perfectly conducting, we will show in the following chapter it also gives good approximation of mutual inductance of the system along practical metal pipe, the conductivity of which is sufficiently large.

3.3 PEC Pipe with Ferrite Layer

In the following chapters, we will show that the magnetic coupling between the transmitter and receiver can be enhanced if we add a layer of soft ferrite on the metallic pipe. We will use experiment and FEM simulation to support this new design but in this chapter, we are going to use an analytical method to derive a formula for mutual inductance for the design in question. The model for a pipe covered with a ferrite layer is shown in Figure 3-3.

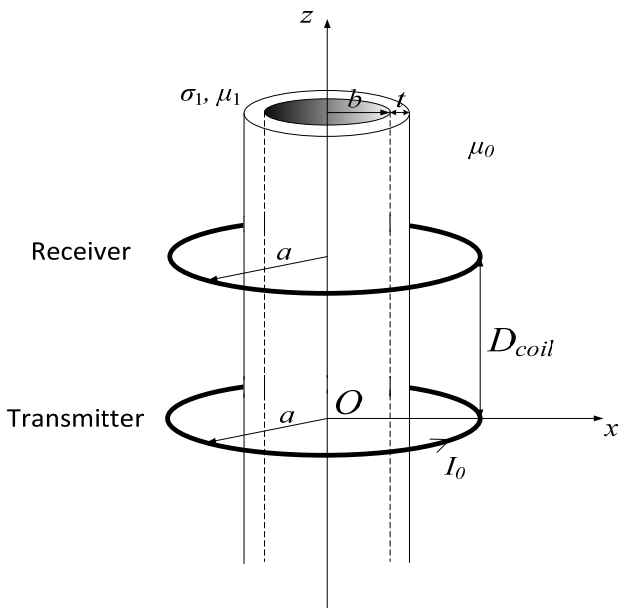

Figure 3-3. The analytical wireless power transfer model for with pipe covered by soft ferrite material.

For simplicity, we assume that the pipe in the model is perfectly conducting. Therefore, at the boundary of $\rho = b$, the electric field should be zero. In order to satisfy the boundary condition, we directly write the electric vector potential in the region of the ferrite layer as

$$F_{z1}^{sca} = \int_{-\infty}^{+\infty} X(k_z) \begin{vmatrix} H_0^{(1)\prime}(k_{\rho 1} b) & H_0^{(1)}(k_{\rho 1}\rho) \\ H_0^{(2)\prime}(k_{\rho 1} b) & H_0^{(2)}(k_{\rho 1}\rho) \end{vmatrix} e^{-jk_z z} dk_z, \tag{3-40}$$

in which

$$k_{\rho 1} = \sqrt{k_1^2 - k_z^2}. \tag{3-41}$$

We also know that

$$H_0^{(1)\prime}(x) = -H_1^{(1)}(x) \text{ and } H_0^{(2)\prime}(x) = -H_1^{(2)}(x). \tag{3-42}$$

Therefore (3-40) can be arranged as

$$F_{z1}^{sca} = \int_{-\infty}^{+\infty} X(k_z) \begin{vmatrix} H_0^{(1)}(k_{\rho 1}\rho) & H_1^{(1)}(k_{\rho 1}b) \\ H_0^{(2)}(k_{\rho 1}\rho) & H_1^{(2)}(k_{\rho 1}b) \end{vmatrix} e^{-jk_z z} dk_z. \tag{3-43}$$

In (3-41), k_1 is the wavenumber of the ferrite layer region. We use first and second kind of Hankel function to denote inward and outward cylindrical waves in (3-40). For the air region, the cylindrical wave is purely outward. So, the electric vector potential is given by

$$F_{z0}^{sca} = \int_{-\infty}^{+\infty} Y(k_z) H_0^{(2)}(k_{\rho 0}\rho) e^{-jk_z z} dk_z. \tag{3-44}$$

Correspondingly, the electric fields in ferrite region and in air are given by

$$E_{\phi 1}^{sca} = -\frac{1}{\varepsilon_1} \int_{-\infty}^{+\infty} k_{\rho 1} X(k_z) \begin{vmatrix} H_1^{(1)}(k_{\rho 1}\rho) & H_1^{(1)}(k_{\rho 1}b) \\ H_1^{(2)}(k_{\rho 1}\rho) & H_1^{(2)}(k_{\rho 1}b) \end{vmatrix} e^{-jk_z z} dk_z \tag{3-45}$$

and

$$E_{\phi 0}^{sca} = -\frac{1}{\varepsilon_0} \int_{-\infty}^{+\infty} k_{\rho 0} Y(k_z) H_1^{(2)}(k_{\rho 0}\rho) e^{-jk_z z} dk_z. \tag{3-46}$$

Similarly, the magnetic fields in ferrite region and in air are given by

$$H_{z1}^{sca} = \frac{1}{j\omega\mu_1\varepsilon_1} \int_{-\infty}^{+\infty} k_{\rho 1}^2 X(k_z) \begin{vmatrix} H_0^{(1)}(k_{\rho 1}\rho) & H_1^{(1)}(k_{\rho 1}b) \\ H_0^{(2)}(k_{\rho 1}\rho) & H_1^{(2)}(k_{\rho 1}b) \end{vmatrix} e^{-jk_z z} dk_z \tag{3-47}$$

and

$$H_{z0}^{sca} = \frac{1}{j\omega\mu_0\varepsilon_0} \int_{-\infty}^{+\infty} k_{\rho 0}^2 Y(k_z) H_0^{(2)}(k_{\rho 0}\rho) e^{-jk_z z} dk_z. \tag{3-48}$$

At the outer boundary of ferrite layer ($\rho = b + t$), the electric field and magnetic field are continuous. Therefore the boundary conditions are given by

$$E_{\phi 1}^{sca}\Big|_{\rho=b+t} = \left(E_{\phi 0}^{sca} + E_{\phi}^{inc}\right)\Big|_{\rho=b+t} \tag{3-49}$$

and

$$H_{z1}^{sca}\Big|_{\rho=b+t} = \left(H_{z0}^{sca} + H_z^{inc}\right)\Big|_{\rho=b+t}. \tag{3-50}$$

Applying these two boundary conditions and through algebraic manipulation, we solve the unknown function $X(k_z)$ and $Y(k_z)$ as

$$Y\left(k_z\right) = \frac{\omega\mu_0\varepsilon_0 a}{4k_{\rho 0}} H_1^{(2)}\left(k_{\rho 0}a\right) \frac{J_1\left(k_{\rho 0}(b+c)\right) - \dfrac{\mu_1 k_{\rho 0}}{\mu_0 k_{\rho 1}} \dfrac{D_1\left(k_{\rho 1}\right)}{D_0\left(k_{\rho 1}\right)} J_0\left(k_{\rho 0}(b+c)\right)}{\dfrac{\mu_1 k_{\rho 0}}{\mu_0 k_{\rho 1}} \dfrac{D_1\left(k_{\rho 1}\right)}{D_0\left(k_{\rho 1}\right)} H_0^{(2)}\left(k_{\rho 0}(b+c)\right) - H_1^{(2)}\left(k_{\rho 0}(b+c)\right)} \tag{3-51}$$

and

$$X\left(k_z\right) = \frac{\omega\mu_0\varepsilon_0 a}{4k_{\rho 0}} H_1^{(2)}\left(k_{\rho 0}a\right) \frac{\dfrac{J_0\left(k_{\rho 0}(b+t)\right)}{H_0^{(2)}\left(k_{\rho 0}(b+t)\right)} - \dfrac{J_1\left(k_{\rho 0}(b+t)\right)}{H_1^{(2)}\left(k_{\rho 0}(b+t)\right)}}{\dfrac{\mu_0\varepsilon_0 k_{\rho 1}^2}{\mu_1\varepsilon_1 k_{\rho 0}^2} \dfrac{D_0\left(k_{\rho 1}\right)}{H_0^{(2)}\left(k_{\rho 0}(b+t)\right)} - \dfrac{\varepsilon_0 k_{\rho 1}}{\varepsilon_1 k_{\rho 0}} \dfrac{D_1\left(k_{\rho 1}\right)}{H_1^{(2)}\left(k_{\rho 0}(b+t)\right)}}. \tag{3-52}$$

In (3-51) and (3-52), the $D_1(k_{\rho 1})$ and $D_2(k_{\rho 1})$ are given as

$$D_1\left(k_{\rho 1}\right) = \begin{vmatrix} H_1^{(1)}\left(k_{\rho 1}(b+t)\right) & H_1^{(1)}\left(k_{\rho 1}b\right) \\ H_1^{(2)}\left(k_{\rho 1}(b+t)\right) & H_1^{(2)}\left(k_{\rho 1}b\right) \end{vmatrix} \text{ and } D_0\left(k_{\rho 1}\right) = \begin{vmatrix} H_0^{(1)}\left(k_{\rho 1}(b+t)\right) & H_1^{(1)}\left(k_{\rho 1}b\right) \\ H_0^{(2)}\left(k_{\rho 1}(b+t)\right) & H_1^{(2)}\left(k_{\rho 1}b\right) \end{vmatrix}. \tag{3-53}$$

On the secondary coil where $\rho = a$, the total electric field is given by

$$E_{\phi 0}^{tot} = \left(-\frac{\omega\mu_0 a}{4}\right) \int_{-\infty}^{+\infty} F_m\left(k_{\rho 0}\right) J_1(k_{\rho 0}a) H_1^{(2)}(k_{\rho 0}\rho) e^{-jk_z z} dk_z, \tag{3-54}$$

in which

$$F_m\left(k_{\rho 0}\right) = 1 - \frac{J_1\left(k_{\rho 0}(b+c)\right) - \dfrac{\mu_1 k_{\rho 0}}{\mu_0 k_{\rho 1}} \dfrac{D_1\left(k_{\rho 1}\right)}{D_0\left(k_{\rho 1}\right)} J_0\left(k_{\rho 0}(b+c)\right)}{H_1^{(2)}\left(k_{\rho 0}(b+c)\right) - \dfrac{\mu_1 k_{\rho 0}}{\mu_0 k_{\rho 1}} \dfrac{D_1\left(k_{\rho 1}\right)}{D_0\left(k_{\rho 1}\right)} H_0^{(2)}\left(k_{\rho 0}(b+c)\right)} \frac{H_1^{(2)}\left(k_{\rho 0}a\right)}{J_1\left(k_{\rho 0}a\right)}. \tag{3-55}$$

Then, the mutual inductance between the transmitter and receiver is given by

$$M_{sys}^{tot} = N_1 N_2 \frac{\mu_0 \pi a^2}{2j} \int_{-\infty}^{+\infty} F_m\left(k_{\rho 0}\right) J_1(k_{\rho 0}a) H_1^{(2)}(k_{\rho 0}a) e^{-jk_z D_{coil}} dk_z. \tag{3-56}$$

Chapter 4 Wireless Power Transfer along Metallic Pipes

In this chapter, we are going to analyze the wireless power transfer model of two coils wound along the metallic oil pipe. We are going to explore the eddy current effect brought by the metallic pipe to see how it affects the power transfer efficiency. We first start with the analytical model discussed in Section 3.1 and 3.2 evaluate the mutual inductance and the power transfer efficiency of the system numerically, and then we are going to validate our model using FEM simulation. We also will show the experimental results and compare them with FEM simulation and numerical modeling.

4.1 Numerical Analysis using Analytical Models

In this chapter we use the stainless steel pipes in lab to perform experiments and simulation. The permeability and the conductivity of the stainless pipe is unknown. But it is estimated that the permeability could be very close to 1. In the following simulations and theoretical analysis, we set the permeability (μ_r) of the pipes as 1 and the conductivity (σ) as 1.1×10^6 S/m. We expect such assumption will result in difference between the simulation and the experimental results. We directly use the dimension of the stainless steel pipe we have in the lab to perform the numerical analysis. The dimension of the stainless steel pipe is given in Table 4-1.

Table 4-1. Dimensions of the Stainless Steel Pipe.

Dimension	Value	Unit
Outer Diamter (*OD*)	113.96	mm
Inner Diamter (*ID*)	108	mm
Pipe Length (L_{pipe})	90	cm

In the analytical model, we are going to assume that the pipe is infinitely long. The transmitting coil and receiving coils we fabricate in lab are solenoids wound on PVC pipe. The pictures of the coils are shown in Figure 4-1.

Figure 4-1. One of the coils used in experiment and modeled in simulation.

In the analytical model, we still model the solenoid coils as single loops wound on the pipe, and we scale the mutual inductance results by multiplying the number of turns of the transmitting coil and the receiving coil. Such an approximation might result in inaccuracy, especially when the coils are near to each other. We will compare the analytical model results with FEM simulation to see the difference. The dimensions of the coils that are measured in the lab are given in Table 4-2.

Table 4-2. Parameters of the Coil Used for Wireless Power Transfer.

Parameter	Value	Unit
Coil diameter (D_{coil})	155.04	mm
Wire diameter (d_w)	2.052	mm
Coil Length (L_{coil})	18	cm
Number of turns (N)	50	dimensionless

Next, we are going to numerically evaluate the infinite integral given in (3-34). In (3-34), the wavenumber in the ρ direction is given by

$$k_{\rho 0} = \sqrt{k_0^2 - k_z^2}. \tag{4-1}$$

Therefore, there are branch cuts in the complex integration domain. We choose to have the integration contour around the Sommerfeld branch cut [25] to fasten the convergence of the integral. The integration contour and the Sommerfeld branch cuts are shown in Figure 4-2.

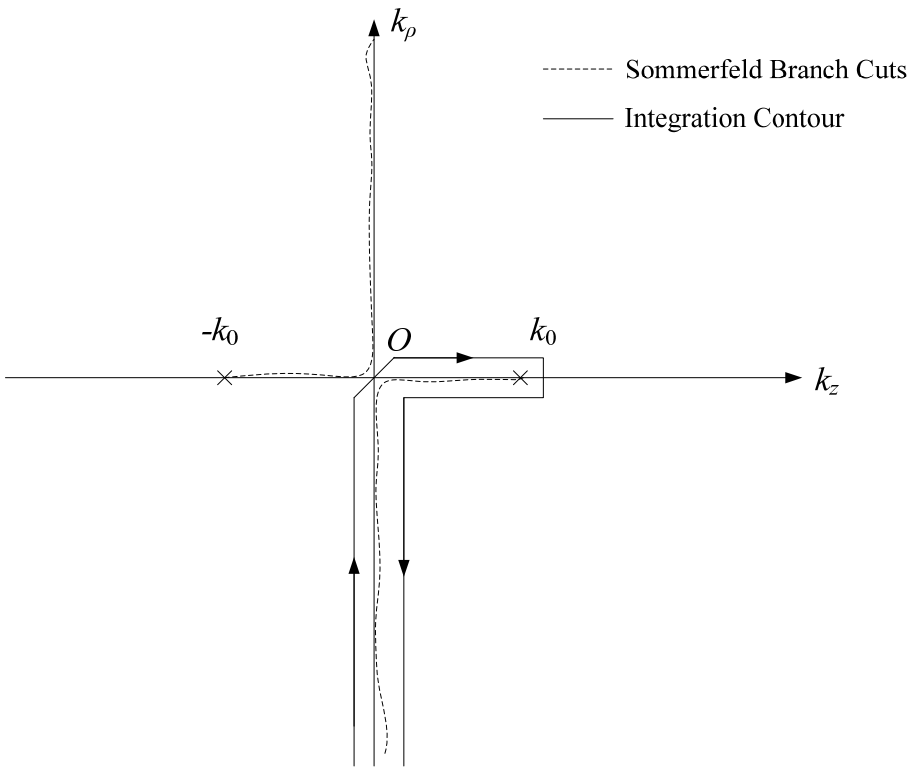

Figure 4-2. Sommerfeld branch cuts and the integration contour.

Assuming the conductivity of the pipe metal is 1.1×10^6 S/m, we calculate and plot the mutual inductance between the two coils along the metallic pipe, and we compare the results with the mutual inductance without the presence of the metallic pipe. We are going to calculate the mutual inductance in a lossless environment in two ways, one using the infinite integral given by (3-25), and the other using the elliptic integral given by (3-1). We plot the results for mutual inductance in Figure 4-3.

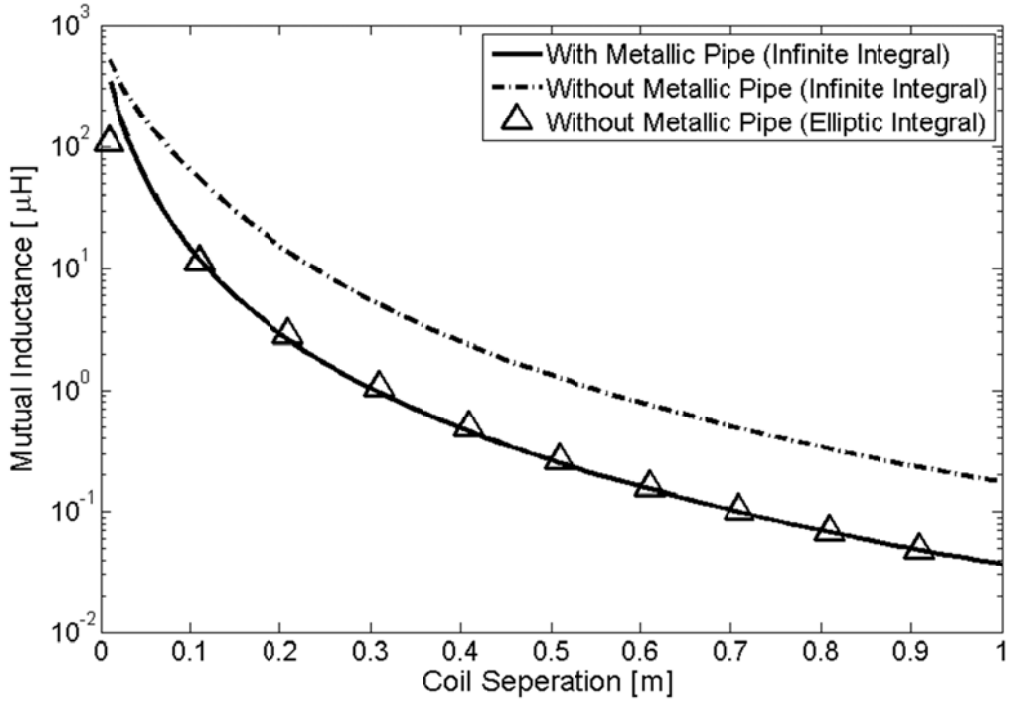

Figure 4-3. Mutual inductance $|M_{sys}|$ given by analytical model at 100 kHz.

In Figure 4-3, the "coil separation" is defined as the distance between the nearest edges of the coils. The mutual inductance between the coils will be slightly complex according to the previous discussion, but it is the magnitude of the mutual inductance that is related to the power transfer efficiency, as indicated in (2.49) and (2.52). We can see that the mutual inductance between two coils is affected negatively by the presence of the metallic pipe, and according to our previous discussion, this is due to the fact that the eddy current induced on the metallic pipe will counteract the magnetic flux generated by the primary coil. Also, the mutual inductance results calculated by the infinite integral form of (3-25) and elliptic integral form of (3-1) agree with each other very well, which validates our method of spectral domain analysis given in Chapter 3.

According to (3-39), the mutual inductance between coils along metallic pipe can be asymptotically calculated by the mutual inductance in air multiplied by a factor. We plot numerical results of mutual inductance calculated by the infinite integral and by the asymptotic formula, which is shown in Figure 4-4.

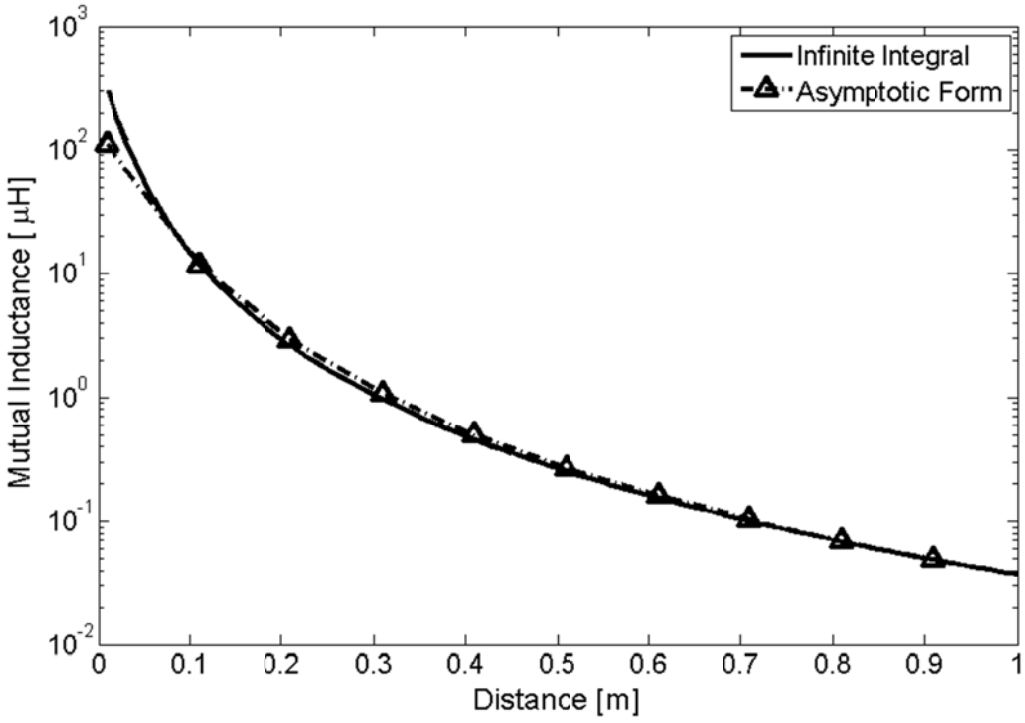

Figure 4-4. Mutual inductance for two coils on a pipe calculated by infinite integral and asymptotic formula.

In Figure 4-4, we substitute the elliptic integral results for the lossless environment mutual inductance into (3-39) to obtain the asymptotic results of mutual inductance along the metallic pipe. We keep the pipe conductivity as 1.1×10^6 S/m. We can see that as the coil separation becomes sufficiently large, the asymptotic results of mutual inductance become very close to the infinite integral result provided by (3-36). Though (3-39) is derived under the condition that the metallic pipe is perfectly

conducting, we can see from the result above that the asymptotic formula also applies to actual pipes with finite but sufficiently large conductivity.

4.2 FEM Simulation

In this section we are going to validate the mutual inductance results via FEM simulation and evaluate the power transfer efficiency. The FEM simulation package we use in this dissertation is ANSYS Maxwell 2D eddy current solver. We use two approaches to model the coils in the FEM simulation. One is to use single loop, which is the same as the analytical model. The mutual inductance results will be scaled by multiplying the square of the number of turns. The other is to directly model the whole coil in the FEM simulation and directly extract the mutual inductance and coil impedance from the simulation results. The comparison of these two models is illustrated in Figure 4-5.

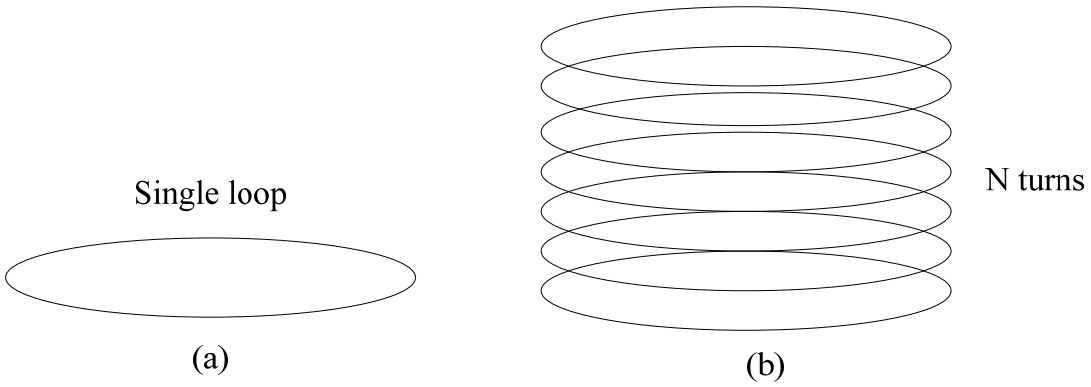

Figure 4-5. Two ways of modeling coils in FEM simulation software: (a) Single loop model, with inductance and resistance scaled by number of turns in post-processing; (b) Whole coil model with each turn directly modeled in the simulation.

In the following we are going to refer these two methods of modeling as the single loop model and the whole coil model. The FEM simulation results of the mutual inductance are given in Figure 4-6.

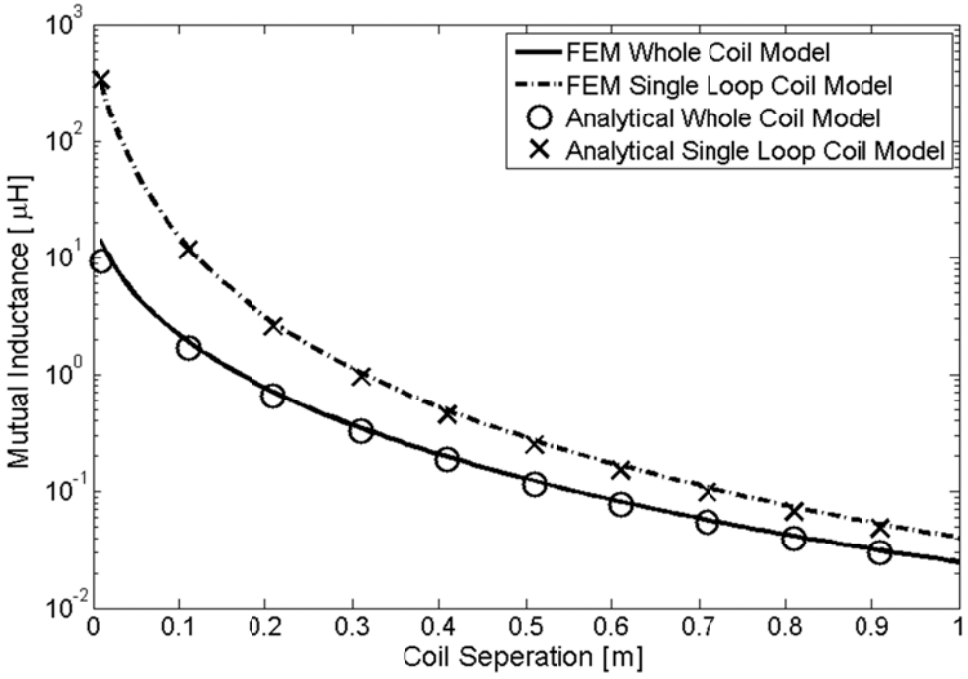

Figure 4-6. FEM simulation of mutual inductance between two coils along a metallic pipe at the frequency of 100 kHz.

The single loop coil model predicts higher mutual inductance results than the whole coil model. This is because the open circuit voltages induced on each turns of the secondary coil is not uniform. The turns further away from the transmitter induces lesser open circuit voltage as the magnetic flux decays along the center axis. The scaled loop coil model doesn't consider the dimension of the coil length and assumes each turn of the receiving coil has an open circuit voltage same as the one nearest to the transmitter, hence predicting a higher mutual inductance result. Since the analytical model also regards the coils as single loops and scale the mutual inductance afterwards, the mutual inductance results of analytical model should agree with single loop model of the FEM simulation, and the results in Figure 4-6 confirms this. This result validates the mathematical formulation of the analytical model but also shows that the assumptions made by

analytical model do not totally apply to actual coils. The whole coil model predicts a lower mutual inductance but we expect that the whole coil model agrees better with actual experiment data, which will be shown in the section on the experiment.

The FEM simulation software can also extract the coil impedance and we could use the matrix model formula given in Section 2.4.3 to evaluate the power transfer efficiency. Using the whole coil model, we calculate the power transfer efficiency as in Figure 4-7. The power transfer efficiency is evaluated by (2-52) assuming a power load resistance that is given by (2-51).

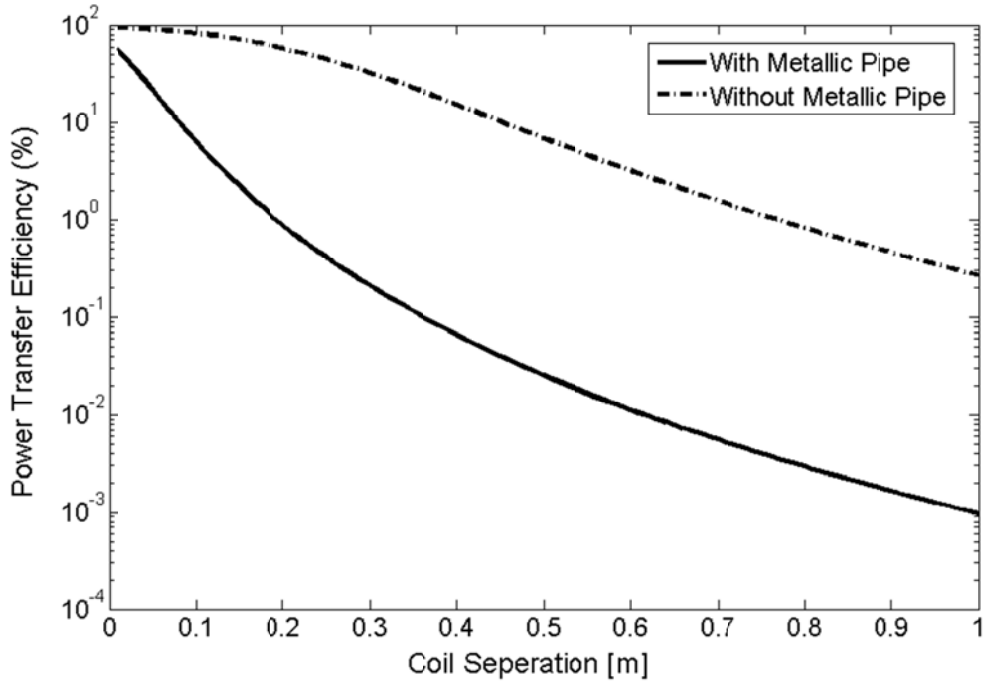

Figure 4-7. FEM simulation of power transfer efficiency at the frequency of 100 kHz.

4.3 Experiment Validation

In this section, we need to validate the efficiency and mutual inductance data given by the whole coil model. We test the power transfer system in an actual experiment

and compare the measured data with FEM simulation. The experimental setup is given in Figure 4-8.

Figure 4-8. Experimental setup for wireless power transfer along stainless steel pipe.

The tuning capacitor and the power load are installed on the breadboard shown in Figure 4-8. We use a function generator as the power source and use it to feed the transmitter coil. The input voltage (V_{in}) and the input current (I_{in}) of the transmitter are measured by voltage and current probes connected to an oscilloscope. We also measure the output voltage (V_{out}) on the power load (R_L) to calculate the output power. Then, the power transfer efficiency of the system is given by

$$e_T^{meas} = \frac{P_{out}}{P_{in}}, \tag{4-2}$$

in which

$$P_{in} = \frac{1}{2} V_{in} I_{in} \cos 2\pi f \Delta t \tag{4-3}$$

and

$$P_{out} = \frac{V_{out}^2}{2R_L}. \tag{4-4}$$

In (4-3), f is the frequency of the input voltage, and Δt is the time delay between the input voltage and the input current. The time delay can be directly measured by the time cursor of the oscilloscope. By connecting the voltage probe directly to the open ends of the secondary coil, we can measure the open-circuit voltage of on the receiver and then calculate the mutual inductance. The mutual inductance between transmitter and the receiver is calculated as

$$\left| M_{sys}^{meas} \right| = \frac{\left| V_{open} \right|}{2\pi f \left| I_{in} \right|}. \tag{4-5}$$

Still operating the wireless power transfer system at 100 kHz, we measure the mutual inductance between the coils. The measured results are shown in Figure 4-9.

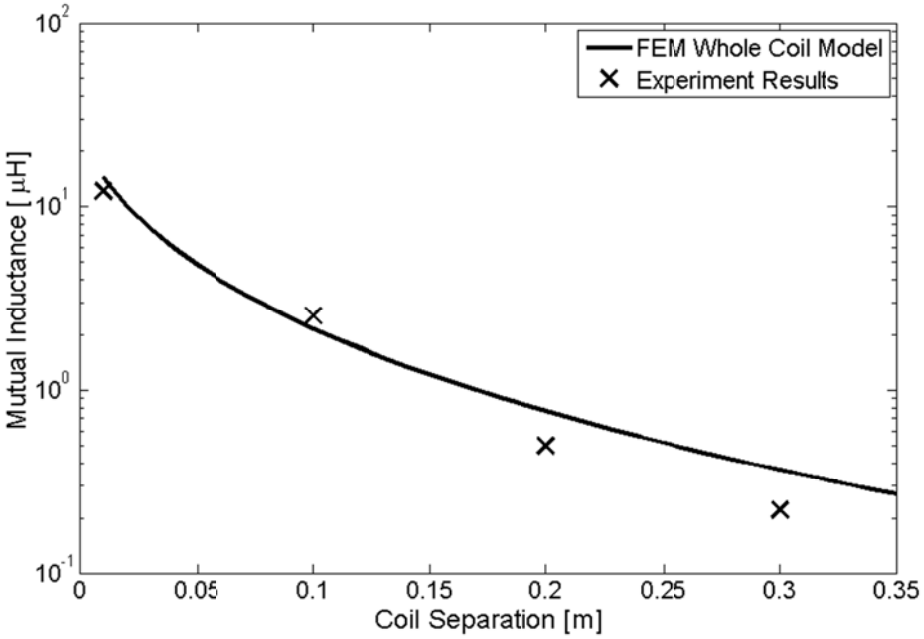

Figure 4-9. Experiment results of mutual inductance and comparison with FEM simulation at the frequency of 100 kHz.

In actual experiment, we measure the mutual inductance with coil separation from 1 cm to 30 cm. When the coil separation becomes further, the open circuit voltage becomes so small that it is difficult to distinguish the signal from the background noise. We collect the effective mutual inductance data and compare them to the corresponding FEM simulation results using the whole coil model, and we find out that the experiment measurement and the FEM simulation agrees to each other. We continue to measure the power transfer efficiency and compare the data with the FEM simulation. The power transfer efficiency is shown in Figure 4-10.

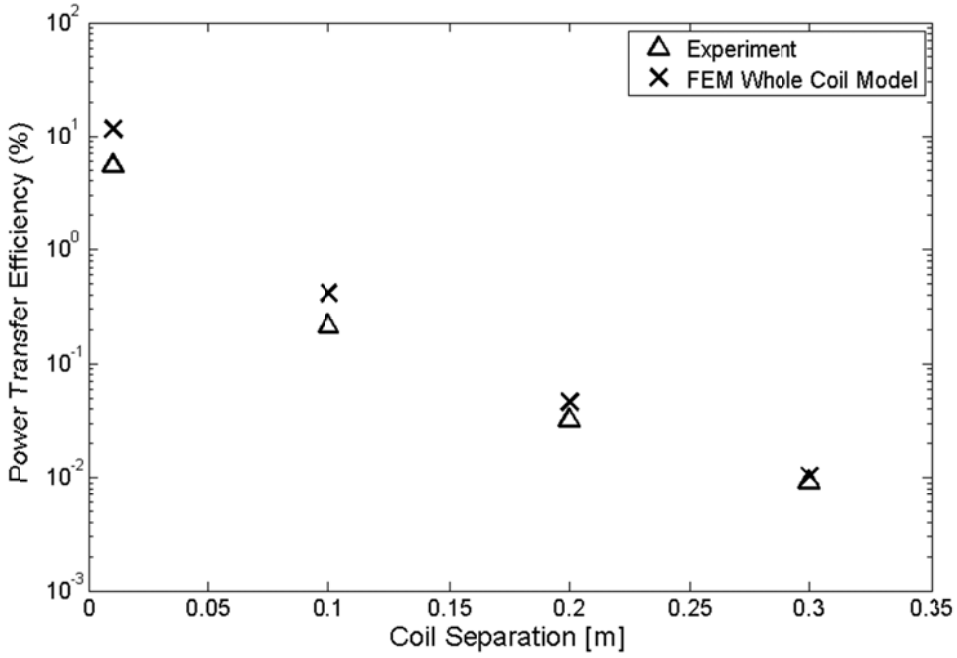

Figure 4-10. Experiment data of power transfer efficiency and comparison with FEM simulation at 10 kHz.

We choose the operation frequency as 10 kHz in Figure 4-10 as this set of experiment efficiency data will be important reference data in Chapter 6. The power transfer efficiency given by FEM simulation of whole coil model is validated by the experimental results. Therefore, we come to know that the whole coil model in FEM simulation gives a closer evaluation for mutual inductance and power transfer efficiency of the actual experiment. The analytical model and single loop model predicts both mutual inductance and power transfer efficiency higher than the actual value. Still, these two models are useful when we add new structures to the original model and we want to have a quick estimation of the model performance. Later on we need to rely on the whole coil model to validate with actual experiments. In the following chapters, we are going to use this model to explore the ways to improve the power transfer efficiency of the system by adding ferrite materials.

Chapter 5 Wireless Power Transfer with Ferrite Cores

5.1 Description of the Model

The eddy current induced by the metallic pipe will counteract the magnetic flux and the power transfer efficiency is affected negatively. In this chapter, we explore the method of improving power transfer efficiency by adding soft ferrite cores to the transmitting and receiving coils. Soft ferrite materials are ferromagnetic materials with large relative permeability (μ_r) [26]. Also, the magnetic polarization of the material is easily switched by the external alternating magnetic field, so the hysteresis effect for this kind of material is relatively low. With high permeability, coil cores made by such materials are able to enhance the magnetic flux generated by the transmitting coil and then increase the mutual inductance between the transmitter and receiver. The wireless power transfer system with ferrite core is illustrated in Figure 5-1.

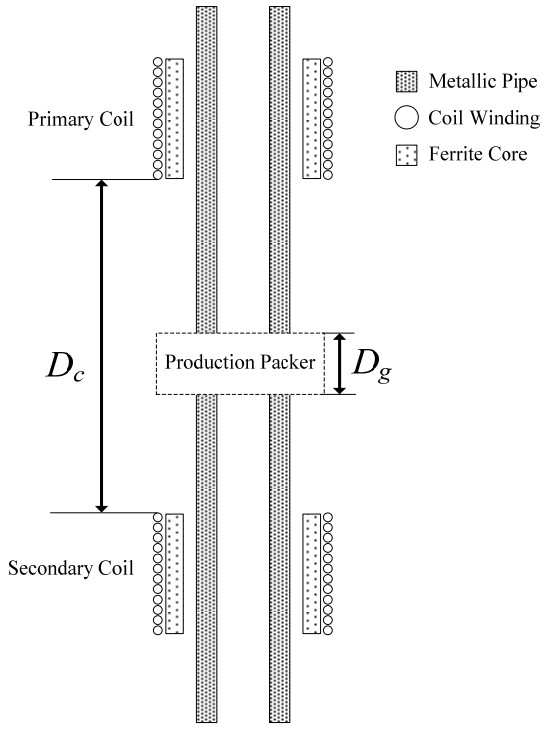

Figure 5-1. Wireless power transfer system with ferrite cores on coils.

The ferrite core we use is the Ferroxcube 3C90. This is a low frequency power material for general purpose transformers at a frequency up to 0.2 MHz [27]. Some of the important parameters of the material are given in Table 5-1.

Table 5-1. Parameters of 3C90 Ferrite Material.

Parameter	Condition	Value	Unit
Initial Relative Permeability (μ_i)	25 °C; ≤ 10 kHz; 0.25 mT	2300±20%	
Conductivity (σ)	DC, 25 °C	0.2	$S \cdot m^{-1}$
Curie Temperature (T_c)		≥ 220	°C
Density		≈ 4800	$kg \cdot m^{-3}$

The initial relative permeability of the 3C90 ferrite is large (2300) and such magnetic properties help concentrating the flux inside the ferrite core of the material. It also has a high Curie's temperature (larger than 220 °C) so the ferrite core can maintain the magnetic property even in the downhole environment with high temperatures over 100 °C. However, the electric conductivity of the material will add eddy current loss to the coils as the frequency increases. Also, the permeability of the material is a complex number as the frequency becomes higher. The curves of permeability for real and imaginary parts are shown in Figure 5-2.

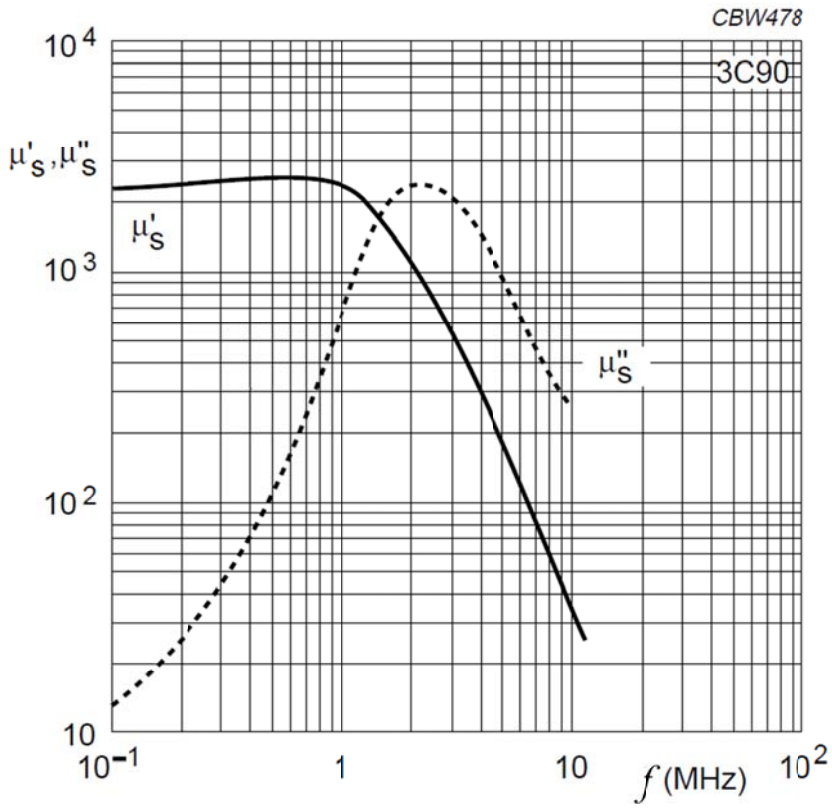

Figure 5-2. Real and imaginary parts of the permeability of the 3C90 material (Courtesy of Ferroxcube) [27].

5.2 FEM Simulation

It is difficult to evaluate the system with the analytical model so we directly apply FEM simulation to the model. We use the same coils shown in chapter 4, and we add 3C90 ferrite cores to the coil to enhance the magnetic coupling. There are commercial ferrite cores made of 3C90 material in the market and we are going to use the one called T140/106/25. The dimension of the core T140 is given in the following Table 5-2.

Table 5-2. Dimensions of the T140/106/25 Ferrite Core.

Dimension	Value	Unit
Outer Diameter (*OD*)	140	mm
Inner Diameter (*ID*)	106	mm
Pipe Length (L_{pipe})	25	mm

We combine eight T140/106/25 cores to together and install them into the coils that we have shown in Chapter 4. The combined cores have the approximate length of 200 mm. The inner diameter of the T140 is lesser than the outer diameter of the stainless steel metal pipe we use in Chapter 4. Therefore, we use the black steel pipes in lab, though the permeability and conductivity of the pipe is unknown. Same as the stainless steel pipe, we assume the permeability (μ_r) as 1, and the conductivity as 1.1×10^6 S/m. We will show that such assumption will not affect the simulation result of mutual inductance, but it will make the input impedance of the coils different from the actual value so that the simulation data of power transfer efficiency might be different from the experimental results. The dimension of the black steel pipe is given in the following Table 5-3.

Table 5-3. Dimensions of the Black Steel Pipe.

Dimension	Value	Unit
Outer Diameter (*OD*)	88.9	mm
Inner Diameter (*ID*)	76.9	mm
Pipe Length (L_{pipe})	1	m

In this simulation, we directly set the relative permeability of the black steel pipe as 1 and assume the conductivity is the same as the stainless steel pipe. We will expect that the simulation results and the experiment results are different and we will explore the difference in the next section. The mutual inductance between the coils is illustrated in Figure 5-3.

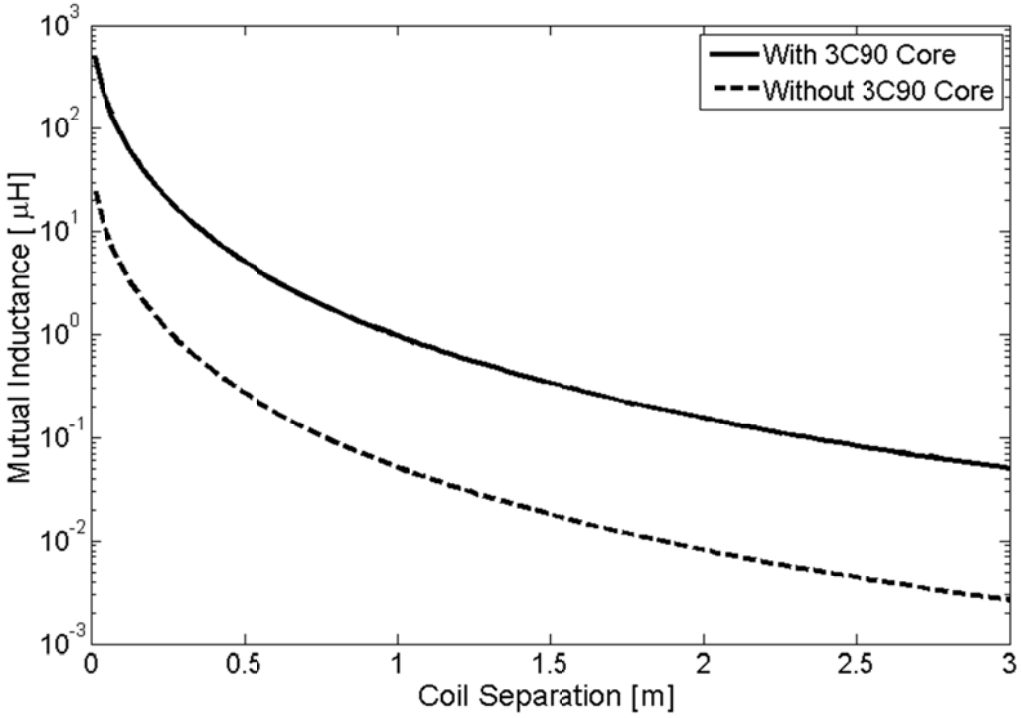

Figure 5-3. FEM simulation of mutual inductance between the coils at 100 kHz with comparison of with or without 3C90 core on the coils.

The magnetic coupling between the coils with 3C90 core is apparently stronger than that without any ferrite cores. We expect that the power transfer efficiency is also going to be improved. The FEM simulation results for the optimum power transfer efficiency are given in Figure 5-4.

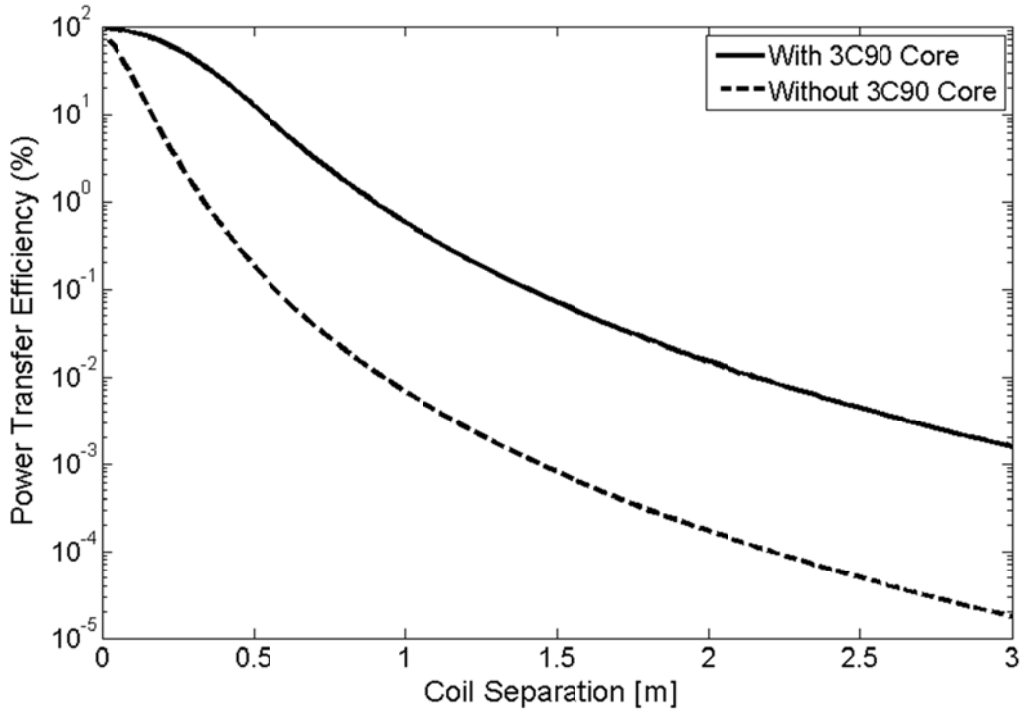

Figure 5-4. FEM simulation of power transfer efficiency of coils with 3C90 core.

The results show that adding the ferrite core will enhance the magnetic coupling and therefore increase the power transfer efficiency. This is the first step towards improving the wireless power transfer system along the oil pipe to meet practical industrial requirements. In the following section we will validate the simulation results via experiment.

5.3 Experimental Validation

We already discussed the improvement of mutual inductance and the power transfer efficiency brought by the 3C90 ferrite cores on the coils. We use FEM simulation to show the improvement. In this section, we are going to validate the simulation results using experiment. The experimental setup is shown in the Figure 5-5.

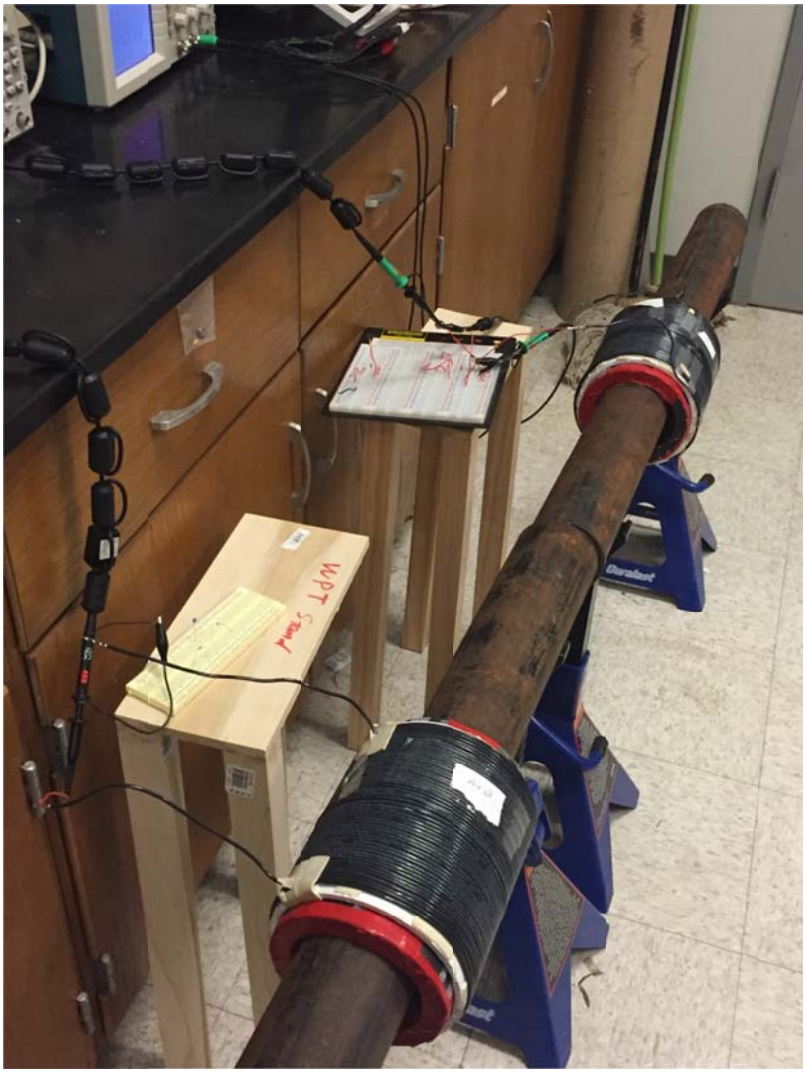

Figure 5-5. Experiment setup for wireless power transfer using coils with 3C90 ferrite cores.

The T140/106/25 3C90 cores are directly installed on the coils described in Chapter 4. We place the coils along the black PE pipes and measure the mutual inductance and the power transfer efficiency. We follow the same experiment procedure discussed in Section 4.3. Also, we will compare the experimental results with the simulation data. The mutual inductance results are shown in Figure 5-6.

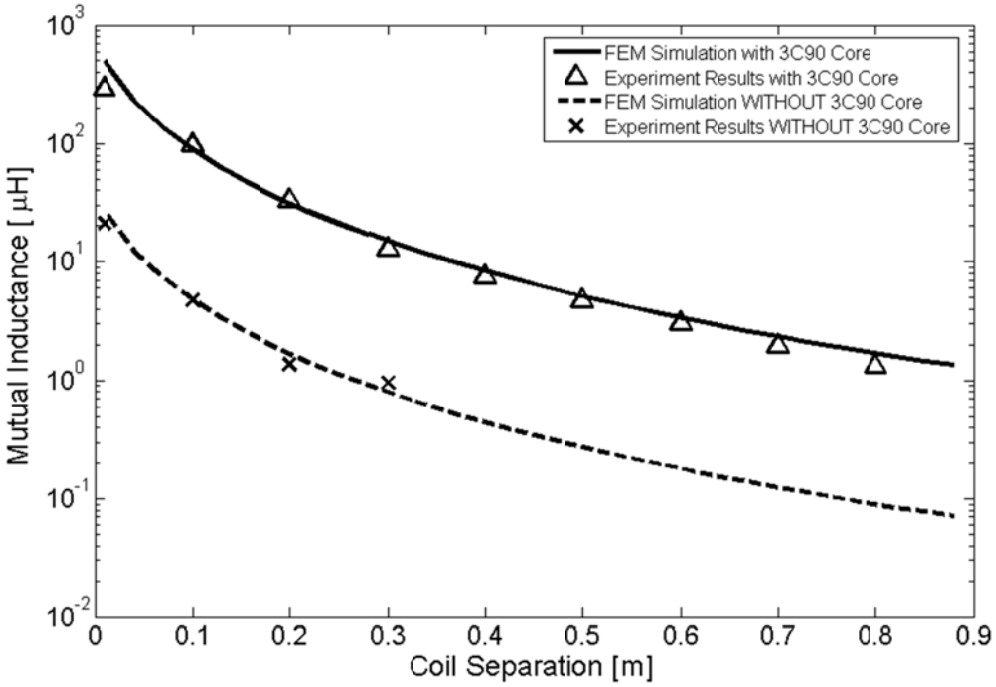

Figure 5-6. Experiment results of mutual inductance between coils with 3C90 ferrite cores.

Both experiment and the simulation show that adding ferrite core will enhance the magnetic coupling of the system. Within the measurable range of the oscilloscope, we find a good agreement between the simulation data and the experiment results. We continue to validate the power transfer efficiency data with experiments. In principle, FEM simulation data predicts the maximum power transfer efficiency that the system could ever achieve given a certain frequency and the coil separation. To approach the maximum efficiency, an optimal load resistor needs to be selected. According to (2-51), the optimum load resistance for maximum power transfer efficiency for each distance varies with the strength of magnetic coupling. When the coils are near to each other, we accordingly adjust the load resistance. When the coil separation enlarges, the optimum load resistance approaches to the Thevenin resistance of the secondary coil. Therefore, it

is reasonable to pick a load resistor the value of which is close to the secondary coil resistance at the desired operation frequency when the coil separation is sufficiently large. We measure the impedance of each coil on the pipe using an RLC meter at the frequency of 100 kHz and the inductance and equivalent series resistance (ESR) of the coils are given in Table 5-4.

Table 5-4. Inductance and ESR of the Coils with 3C90 Cores on the Metallic Pipe.

Parameter	Value	Unit
Primary Coil Inductance (L_1)	737.5	μH
Primary Coil ESR (R_1)	7.67	Ω
Secondary Coil Inductance (L_2)	769.7	μH
Secondary Coil ESR (R_2)	8.44	Ω

It is impossible to find a resistor with the exact value shown in the table. We can only use standard resistors with values close to the coil measurement results. We use a resistor with a reference value of 10 Ω as the load resistor connected to the secondary coil. We follow the measurement procedure described in Chapter 4 and measure the power transfer efficiency of the system. Also, we will compare the results with simulation data. The measured power transfer efficiency is shown in Figure 5-7.

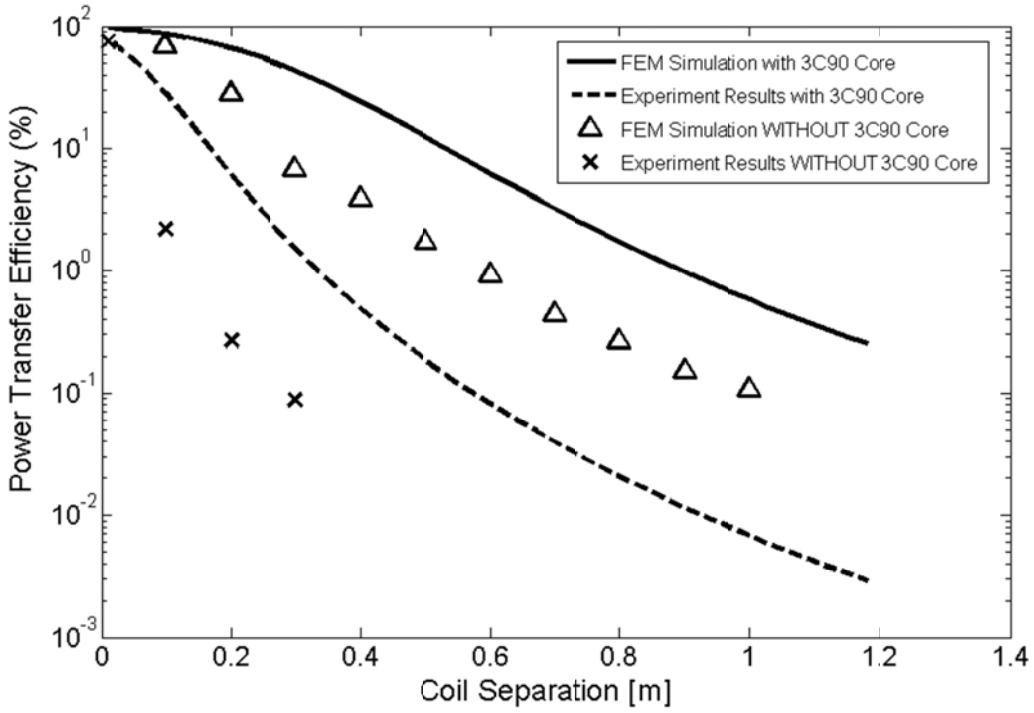

Figure 5-7. Experiment results of power transfer efficiency of the system with 3C90 ferrite cores at 100 kHz.

When the coil separation is small, the experimental results have a better agreement with FEM simulation data. The discrepancy between the simulation and the experimental results become more obvious. This is due to the fact that the FEM simulation estimates a smaller series resistance of the coils at 100 kHz than in the actual measurement. When the coil separation is small, the mutual inductance plays a more dominant role in the power transfer efficiency so we can see that experiment and simulation agree with each other at very small coil separation. As the coil separation increases, the coil resistance becomes dominant in determining the power transfer efficiency. A smaller coil resistance will give a better estimation of the power transfer efficiency according to the matrix model formula. We do not know the exact value of the permeability and conductivity of the pipe material and we directly assume that the

physical properties of the pipe material are the same as stainless steel. Such an assumption might not be valid. But still, we already see that the measured mutual inductance results agree with the simulation data better, because the mutual inductance in this case is more related to the ferrite core material properties, which is known from the data sheet provided by the manufacturer. We already know that the FEM simulation results are over-estimating the power transfer efficiency. But the experimental results also show that adding a soft ferrite core will enhance the magnetic coupling and increase the power transfer efficiency.

Chapter 6 Wireless Power Transfer with Ferrite Layer

6.1 Previous Works Using Ferrite Materials and Guiding Structures

It is very recently that there are emerging works done in the area of inductive power transfer using ferrite materials to increase the magnetic coupling. Large ferrite cores with a length of 3 meters are used to build transmitting and receiving coils for wireless power transfer [28]. The dipole coils described in [28] are wound on ferrite cores with a piecewise linear shape. Such shape makes the flux distribution inside the ferrite core become uniform in an average sense, and the flux lines between two parallel dipole coils become more concentrated, and hence the power transfer efficiency is improved. The efficiency data provided by [28] is promising, but the model is not practical for oil well applications as the diameter of the oil well can never be as large as 3 meters. In recent research, there are approaches that have been studied to add a cement layer to the oil pipe to form an acoustic waveguide, so that acoustic power can transfer along oil pipe wirelessly [18]. The role of the cement layer in [18] is to act as a wave propagating media that concentrate the most of acoustic energy inside of it. Though such an approach can concentrate the propagating acoustic power and improve the power transfer efficiency, there are potential problems of impedance matching between the piezoelectric transducers and the cement layer. Also, the propagating wave energy will suffer from serious reflection if there is a gap or fracture on the cement layer.

6.2 Magnetic Circuit Analogy

Inspired by [28] and [18], we add a ferrite sheet layer onto the oil pipe. The ferrite sheet layer not only concentrates the magnetic flux lines similar to [28], but also acts as a magnetic flux pathway to link the transmitter and receiver wirelessly, which is analogous

to the design given by [18]. The magnetic flux pathway we introduce to our design is actually an open loop magnetic circuit. A typical magnetic circuit is given in Figure 6-1.

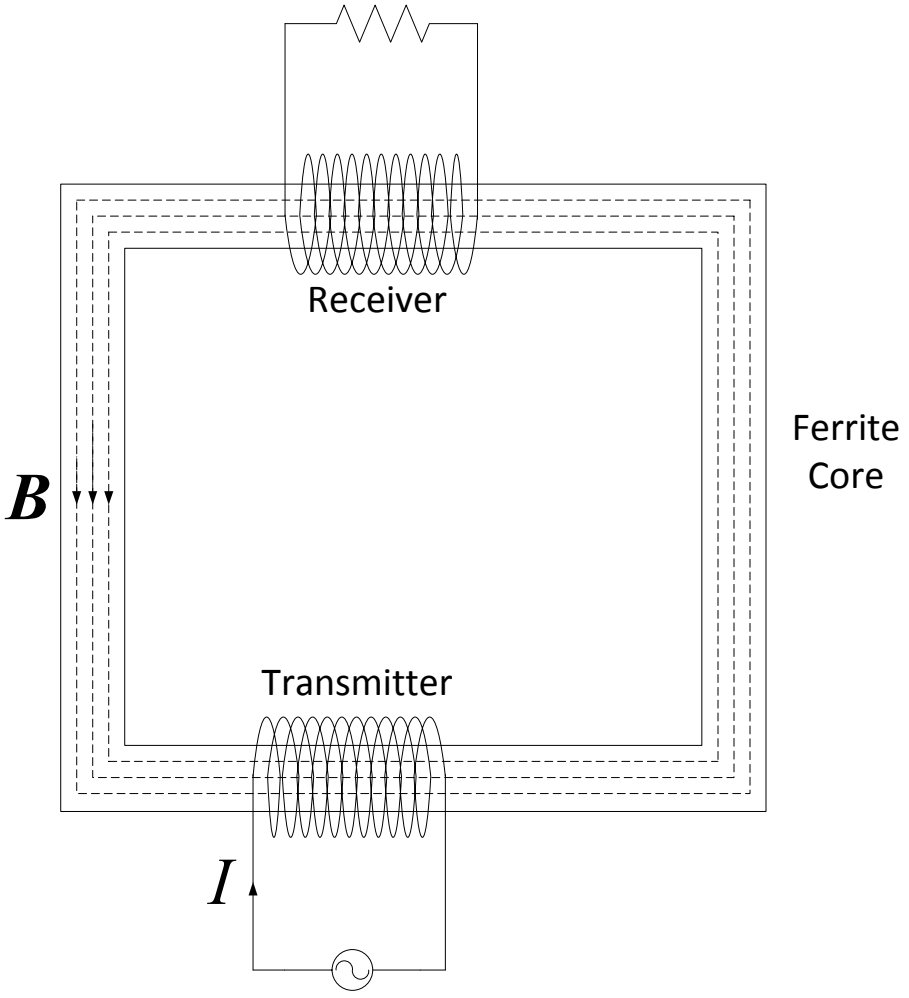

Figure 6-1. Magnetic circuit with a power transmitter and a receiver.

The magnetic circuit is formed by a ferrite loop core. The transmitter wound on the core generates an external magnetic field which induces a magnetic flux distribution inside the magnetic circuit. The magnetic flux in the ferrite core is given by [29]

$$\Phi = \frac{F_m}{R_m}. \tag{6-1}$$

The formula given by (6-1) can be regarded as an Ohm's law for the magnetic circuit. F_m is the magnetic force (magnetic circuit version of electric force in Ohm's law) and R_m (unit: A/Wb) is the magnetic reluctance. The magnetic resistance of the ferrite core is given by

$$R_m = \frac{l}{\mu A}. \tag{6-2}$$

In (6-2), l is the length of the ferrite core segment, μ is the ferrite permeability, and A is the cross section area of the ferrite core. Therefore, we can see that given the length of the ferrite segment, the magnetic resistance will be smaller if we have larger material permeability for the cross section area. These two aspects are crucial to our design. Applying the ferrite layer onto the oil pipe, we obtain an open-loop magnetic circuit, shown in Figure 6-2.

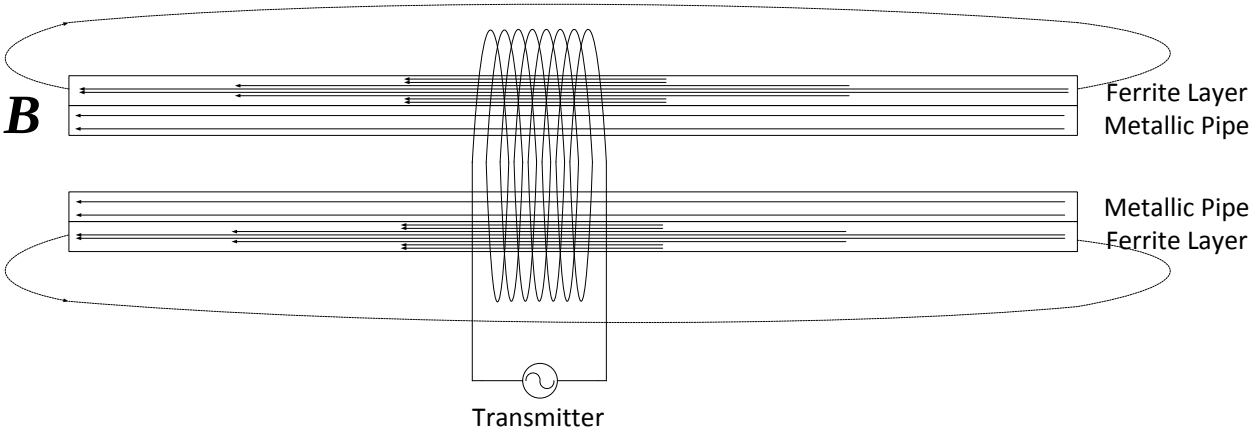

Figure 6-2. Flux density and the open loop magnetic circuit along the oil pipe.

If the ferrite material layer does not form a closed loop pathway, the magnetic flux distribution inside the ferrite material will not be as uniform as shown in [28]. The magnetic flux density will reach its maximum at the location of the transmitter and will reach a minimum at the ends of the ferrite layer sections. But still, due to the low

magnetic resistance of the ferrite material, we manage to concentrate more magnetic flux along the metallic pipe. The time varying magnetic flux carries the reactive magnetic energy. If we add another receiving coil anywhere on the ferrite layer, we could harvest the reactive magnetic energy via magnetic induction. The efficiency of the power transfer will depend on the flux density strength at the location. As the flux density will drop drastically at the ends of the ferrite layer, we either keep the receiver away from the ferrite section ends or enlarge the coverage of the ferrite sheet layer in order to obtain as long of a power transmitting distance as possible. In oil applications, the oil pipe could be ferromagnetic metal as well. In this case, the pipe and the ferrite layer structure are analogous to a parallel electric circuit, shown in Figure 6-3.

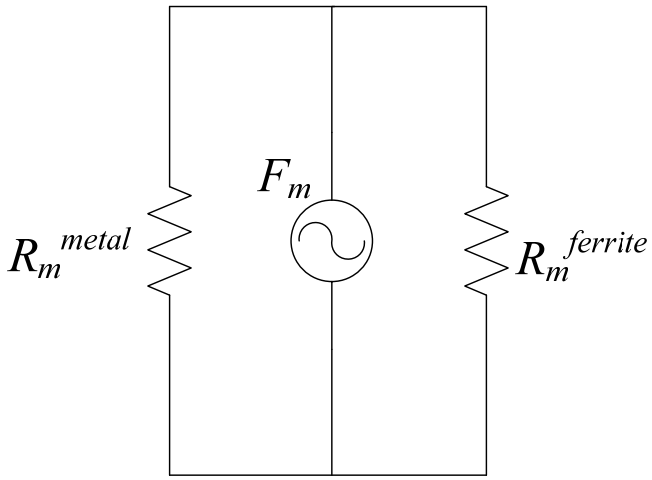

Figure 6-3. Analogous parallel electric circuit model for ferrite layer and metallic pipe structure.

The ferromagnetic metal pipe will also have a relatively large magnetic permeability compared and there will be certain amount of magnetic flux leaked into the metal pipe. The magnetic flux inside the metal pipe will be counteracted by the inverse magnetic field induced by the eddy current effect as the operating frequency increases.

Therefore, it is desired to reduce the flux leaked to the metallic pipe as much as possible. In order to do this, we need to decrease the magnetic resistance of the ferrite layer by using materials with higher permeability or increase the thickness of the ferrite layer. We will show the flux distribution and the thickness adjustment of the ferrite material layer with more details in the section on FEM Simulation.

6.3 Model of Wireless Power Transfer with Ferrite Layer

Based on the discussion above, we develop the wireless power transfer model by covering the metallic oil pipe with a soft ferrite material with a high permeability so that a magnetic pathway is formed along the oil pipe covering the region around the production packer. The model for wireless power transfer is shown in Figure 6-4.

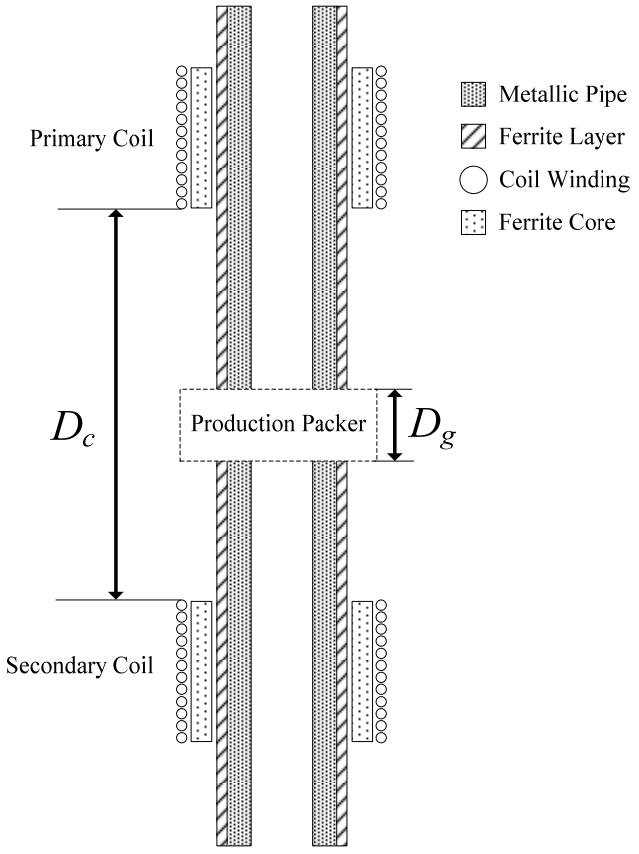

Figure 6-4. The wireless power transfer model with soft ferrite sheet.

In order to implement such a structure in the lab, we need to find ferrite sheet products that could easily be installed on and peeled off from the pipe. In this research, we pay special attention to a class of commercial products called sintered ferrite sheets. Such a ferrite sheet has the properties of high permeability (usually larger than 100) and low loss tangent. The products come with a sticky layer so they are easy to be installed on the metallic pipe. There are several manufacturers providing such products, like Würth Elektronik, Maruwa Co., Ltd, and Toda Kogyo Corporation. We choose the FLX series of Toda Kogyo Co. as the material for the ferrite layer in the simulation. The magnetic property of the FLX series is given in Table 6-1.

Table 6-1. Property of Toda Kogyo FLX Series [30].

Grade	FLX-950	FLX-247	FLX-146	FLX-221
Material	Ni-Zn-Cu Ferrite	Ni-Zn-Cu Ferrite	Ni-Zn-Cu Ferrite	Ni-Zn-Cu Ferrite
Thickness (mm)	0.05~0.3	0.05~0.3	0.05~0.3	0.05~0.3
μ'@13.56 MHz	140	310	380	660
Curie Temp. (°C)	215	210	150	100

We notice that for the FLX series, the Curie temperature becomes lower as the material permeability is made to be higher. We need to keep in mind that the wireless power transfer system we design might be working in a high temperature environment. Therefore, we need to make a balance between the permeability and the Curie temperature when choosing the appropriate material for the ferrite layer. In the following section on the simulation, we choose FLX-247 as a practical option for the ferrite layer

added on the metallic pipe. The sintered ferrite material is effective for concentrating the flux inside the ferrite material, but it is expensive to cover a large distance of metallic oil pipe with such material. When we are conducting experiments to build a startup project, we prefer some material with less cost but with a desired magnetic property. The magnetic shielding sheet 3M 1380 is an ideal choice to build such startup model. The magnetic property of 3M 1380 material is measured in the lab and will be discussed in the following sections. It is made of magnetic shielding material with a large permeability. However, the shielding material also has a large imaginary part of the permeability so we might need to lower the operation frequency to avoid too much loss when using this ferrite sheet product.

6.4 FEM Simulation

6.4.1 Continuous Soft Ferrite Layer

In this section, we are going to add the ferrite layer to the metallic pipe in the FEM simulation model and illustrate the improvement brought by this structure. We first remove the ferrite core of the coils so that we focus solely on the coupling enhancement of the ferrite layer. Also, we first consider the best case scenario in which the ferrite layer is continuous between the transmitter and receiver. In actual applications, there will be production packers along the pipe which leave a gap on the ferrite material layer. The effect of the layer gap will be discussed in the next section. The model for simulation is given in Figure 6-5. The coils shown in Figure 6-5 have the same dimensions as the coils in the previous chapters.

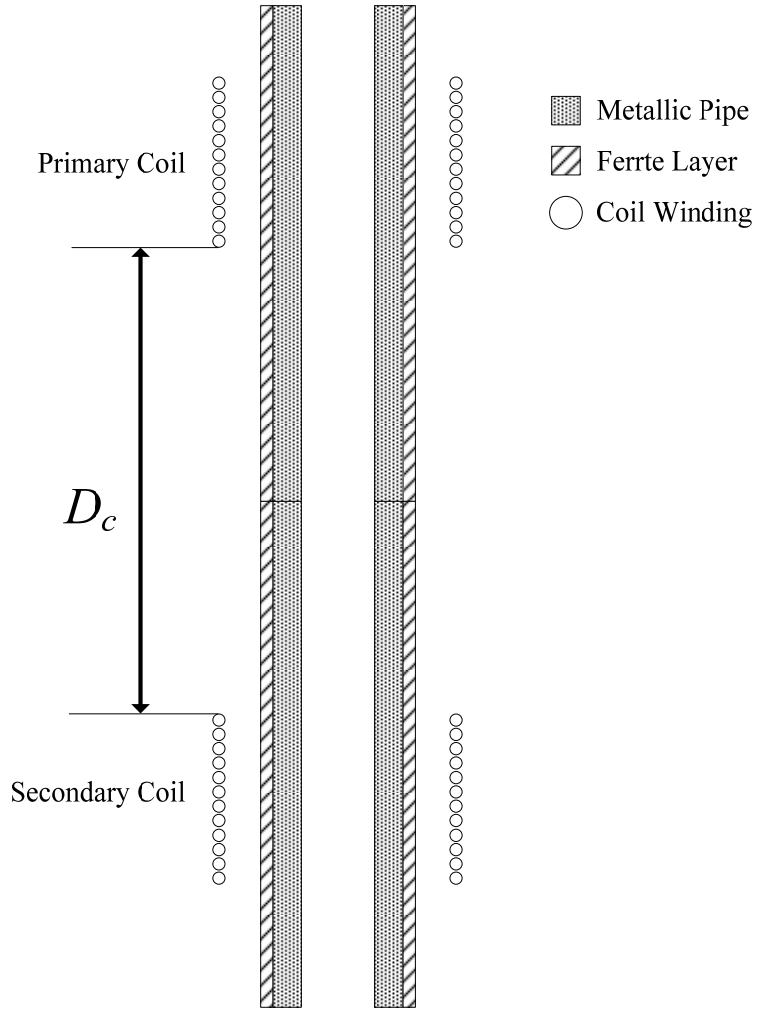

Figure 6-5. The FEM simulation model with a continuous ferrite layer.

We use the parameter values given by Table 6-1 to setup the material properties in the FEM simulation. We set the layer thickness as 0.3 mm the metallic pipe is made of stainless steel. In the simulation, we set the length of both the pipe and ferrite layer as 5 meters. We are also going to calculate the mutual inductance using the analytical method described in Section 3.3 to compare with the FEM simulation results. The FEM simulation result for the mutual inductance is given in Figure 6-6.

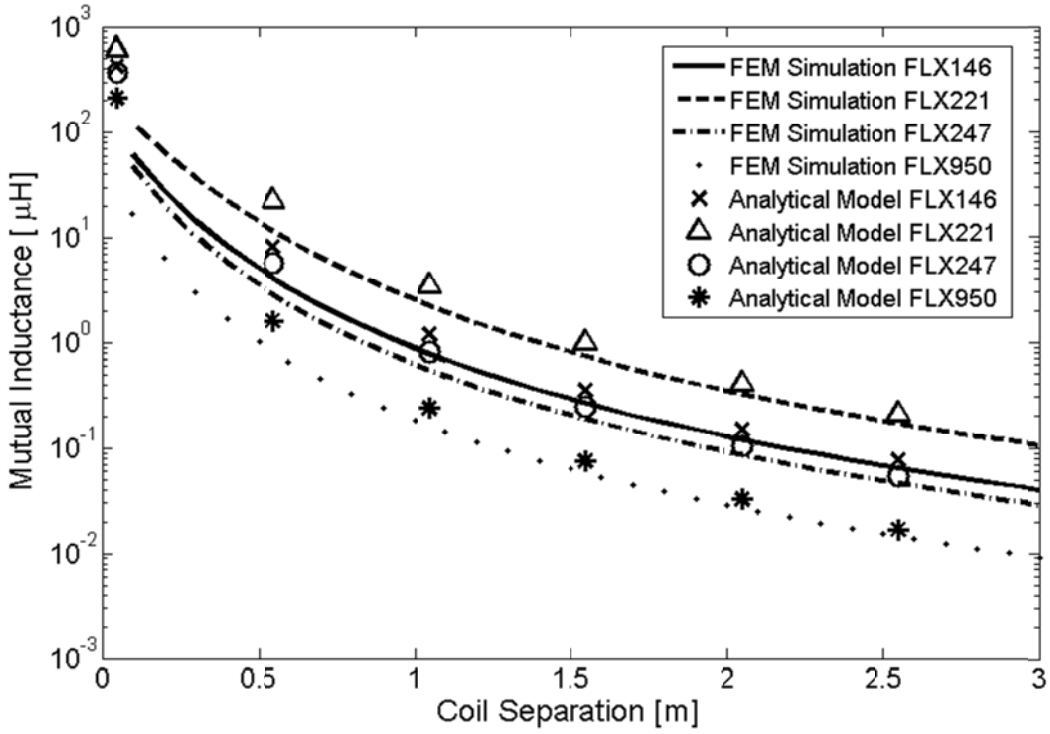

Figure 6-6. The Mutual inductance of the system with a soft ferrite layer.

The analytical model predicts the mutual inductance slightly higher than FEM simulation, but the results are still comparable to each other. At a fixed coil separation, the mutual inductance is positively related to the magnetic permeability. The ferrite sheet FLX221 has the largest magnetic permeability and correspondingly the system with this ferrite layer has the largest mutual inductance given a certain coil separation. We also expect that the larger ferrite layer permeability will also yield better power transfer efficiency. The FEM results for power transfer efficiency are illustrated in Figure 6-7.

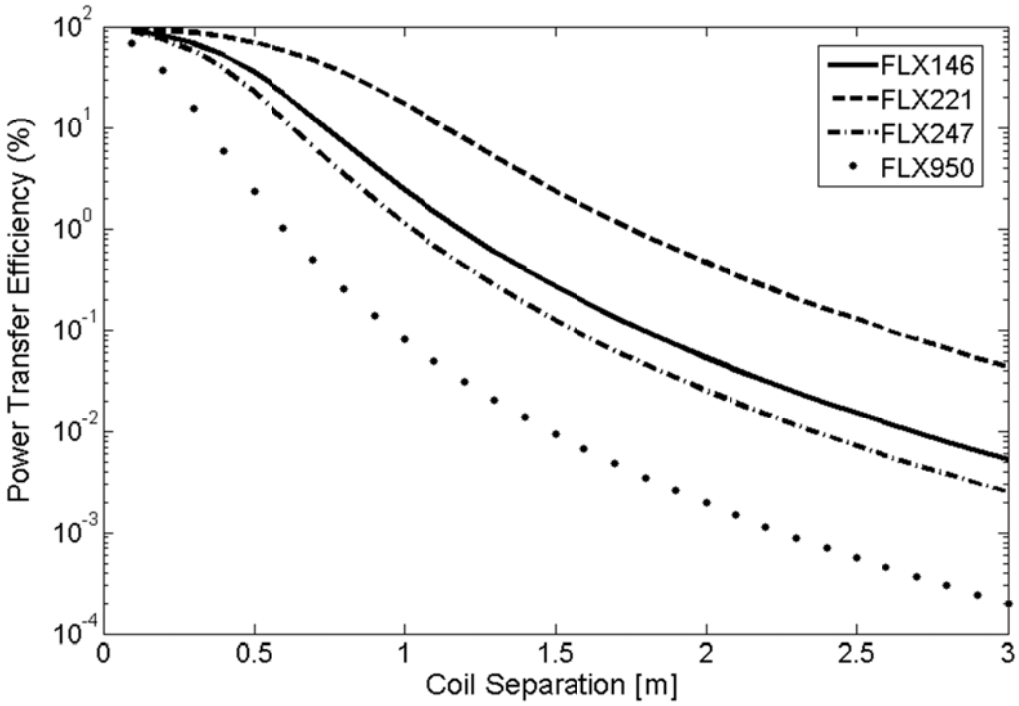

Figure 6-7. FEM simulation of power transfer efficiency with the soft ferrite layer.

Both Figure 6-6 and Figure 6-7 show that adding a soft ferrite layer improves the magnetic coupling and the power transfer efficiency of the wireless power transfer system along the metallic pipe. The ferrite layer is acting like an open-ended magnetic circuit, and we can lower the magnetic resistance of this layer structure not only by increasing the permeability of the material, but also by adding thickness of the layer structure. Using FLX247 as the ferrite layer material, we vary the layer thickness and the mutual inductance of the two coil system along the pipe is then given in Figure 6-8.

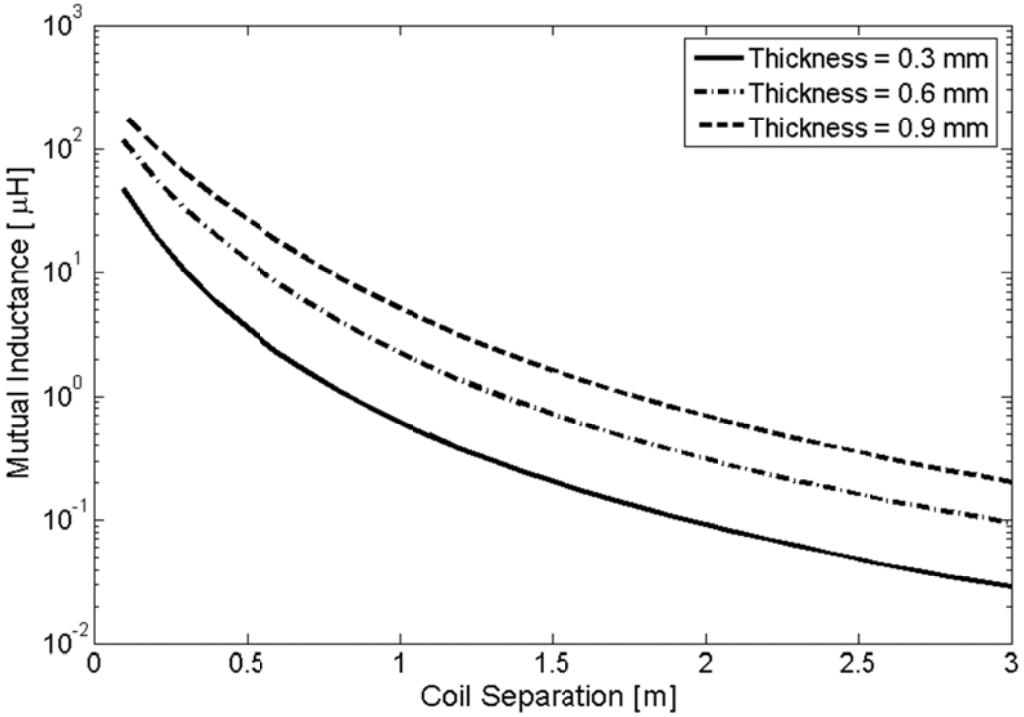

Figure 6-8. FEM simulation of mutual inductance with a ferrite sheet layer of varying thickness.

Adding thickness to the ferrite layer enhances the magnetic coupling between the coils. We should expect the same for the power transfer efficiency. We use the matrix model formula to predict the optimal power transfer efficiency of the system given a range of coil separation, and the simulation results for the power transfer efficiency is given in Figure 6-9.

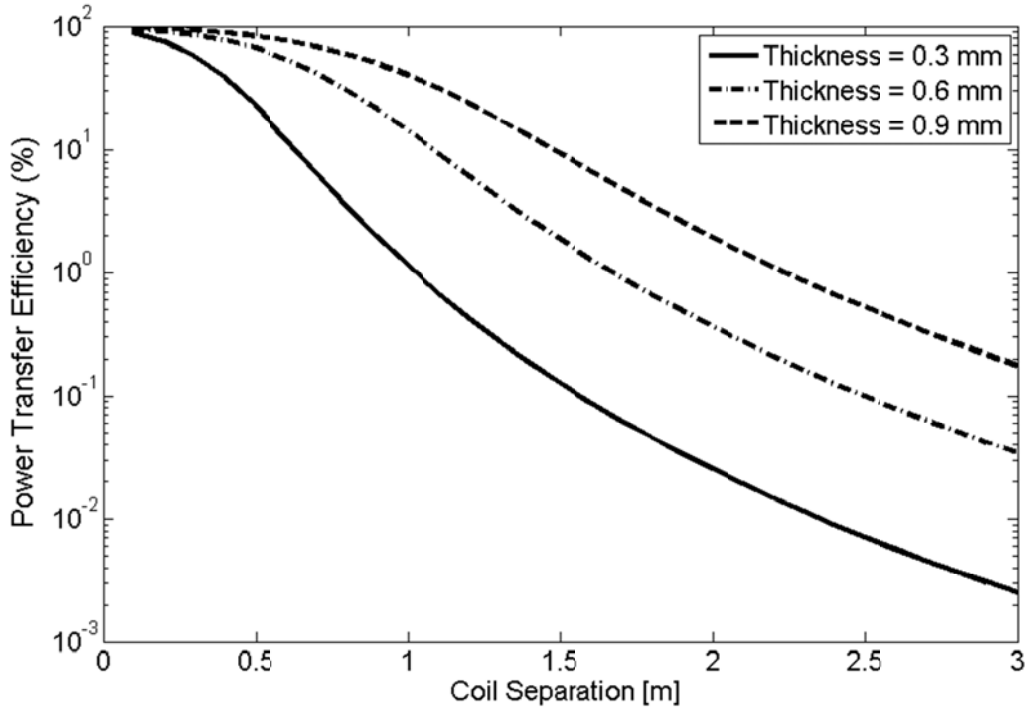

Figure 6-9. FEM simulation of power transfer efficiency of the system with a soft ferrite layer of varying thickness.

6.4.2 Soft Ferrite Layer with a Gap

In Section 6.4.1 we assumed that the ferrite layer on the pipe is continuous between the transmitter and receiver. However in an actual application, we might not be able to customize the production packer between the coils to cover it with ferrite layer as well. Therefore, we need to consider the situation that there is a gap in the ferrite layer, and we need to model the gap structure in the FEM simulation. The production packers are mostly made of rubber material so it is reasonable for us to model a pipe break in the simulation as well. The simulation model of the system with a gap is shown in Figure 6-10.

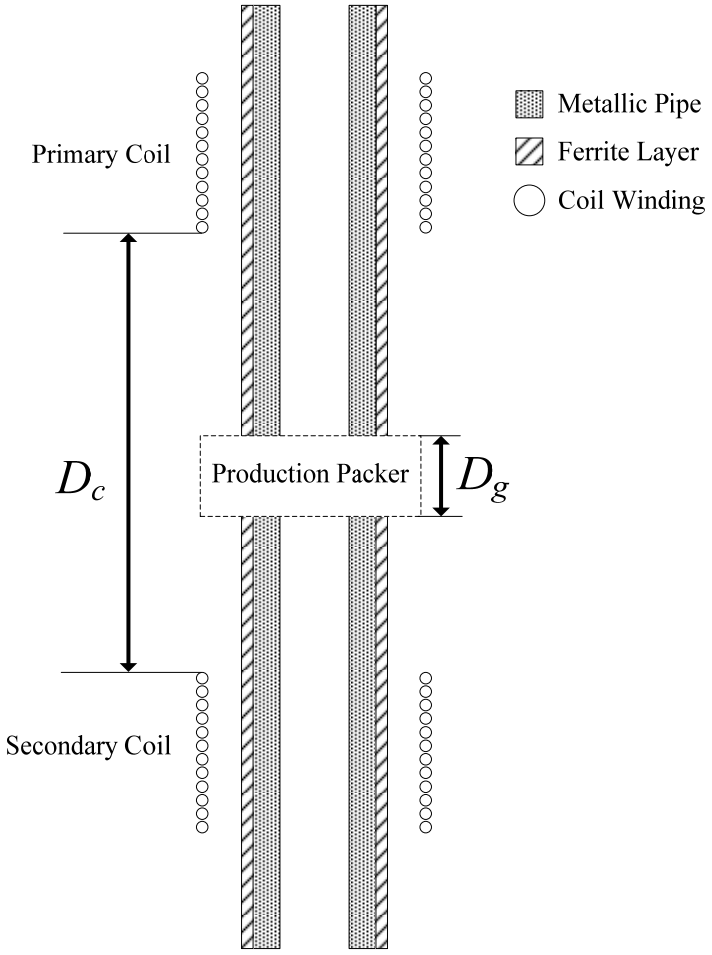

Figure 6-10. FEM simulation model with a pipe gap.

In FEM simulation, we set the coil separation (D_c) as 1 meter and we vary the gap distance (D_g) from 10 cm to 1 meter and calculate the mutual inductance and power transfer efficiency. The mutual inductance of the system is shown in Figure 6-11.

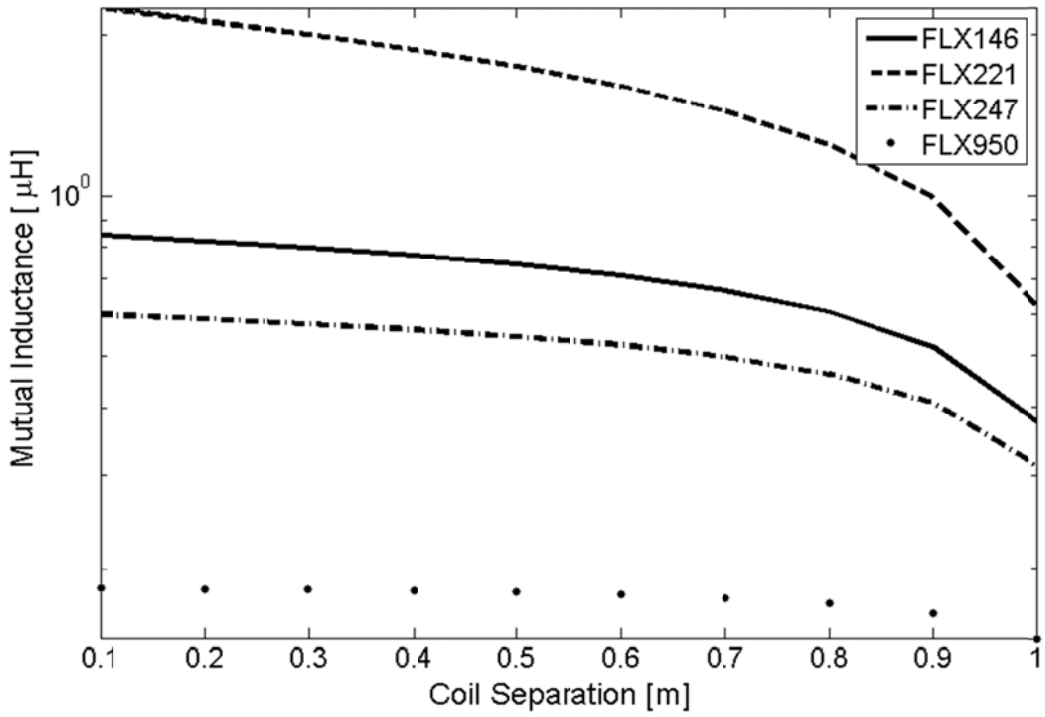

Figure 6-11. FEM simulation of mutual inductance with pipe gap variations.

Given the fixed coil separation of 1 meter, we gradually increase the pipe gap to see the change in the mutual inductance. We notice from Figure 6-11 that only when the gap length is close to 80% of the coil separation will the mutual inductance curves have an obvious decrease. Similarly, we perform simulation to estimate the optimal power transfer efficiency and the results are shown in Figure 6-12.

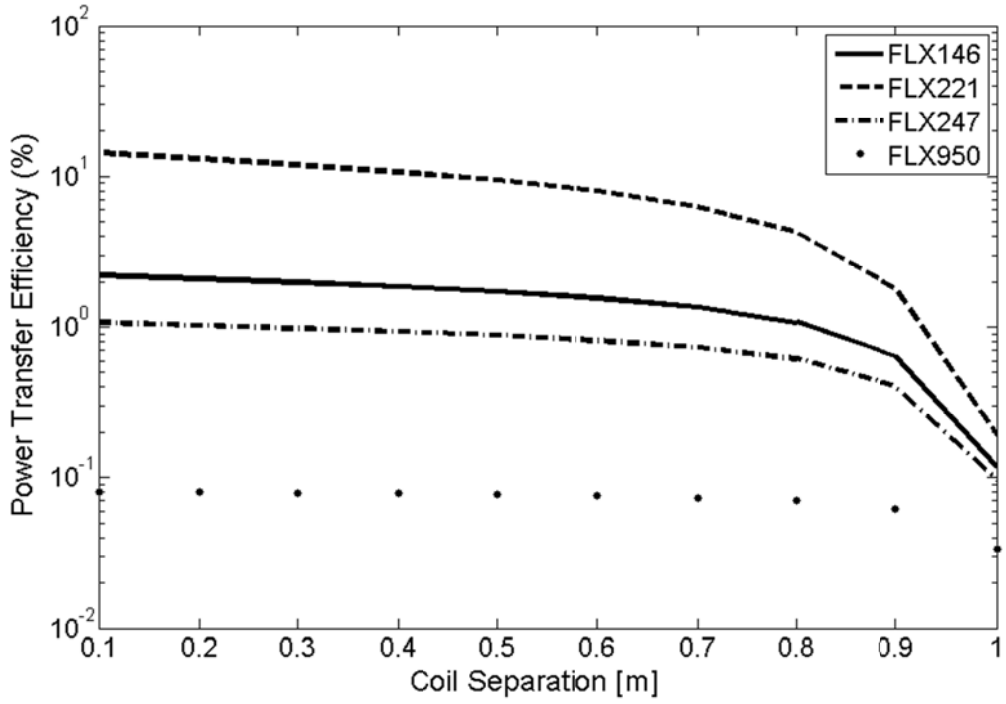

Figure 6-12. FEM simulation of power transfer efficiency with gap variations.

Based on the results of Figure 6-11 and Figure 6-12, we conclude that the pipe gap will not affect the mutual inductance and power transfer efficiency very much as long as the gap length is small compared to the coil separation. Therefore, the design given in this research could also apply to the situation in which the production packer is not customized by covering it with a soft ferrite layer.

6.4.3 Combining Ferrite Layer and Ferrite Core

We have already seen that adding a ferrite layer on the metallic oil pipe improves the magnetic coupling and power transfer efficiency. We could further improve the performance of the system by adding ferrite cores to the coils. A simulation model of wireless power transfer with a ferrite layer and ferrite cores is given in Figure 6-13.

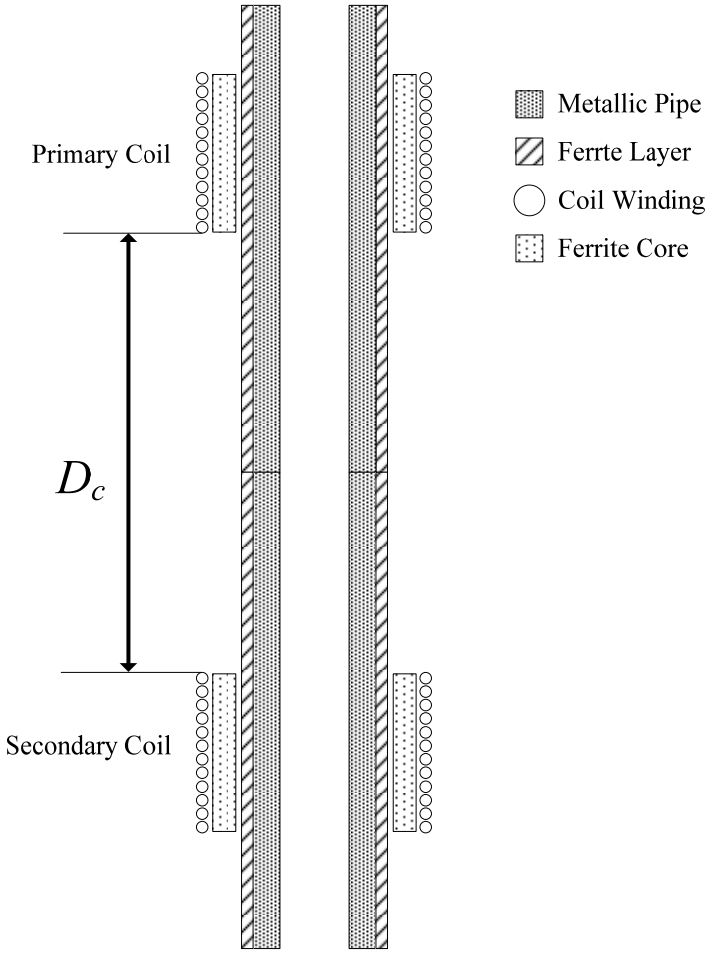

Figure 6-13. Simulation model of wireless power transfer with a ferrite layer and ferrite cores.

In Figure 6-13 we keep the ferrite layer continuous on the pipe so that we could compare with the mutual inductance and power transfer efficiency results from the model given in Figure 6-5. The soft ferrite material for the ferrite layer on the pipe is FLX247 and the ferrite cores on the coils are made of 3C90. The FEM simulation of mutual inductance is given in Figure 6-14.

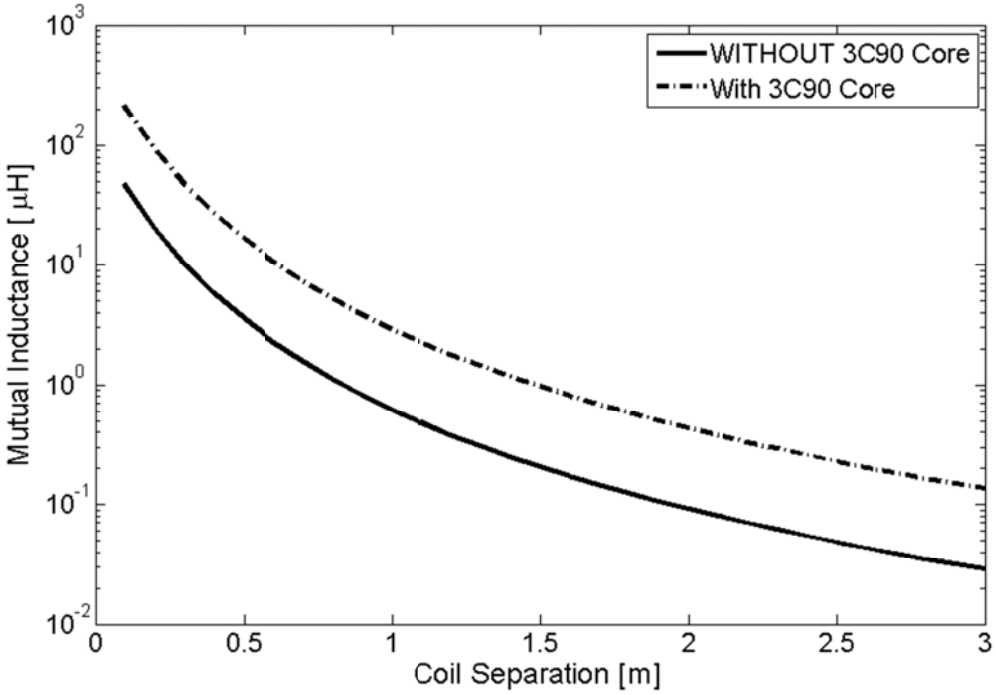

Figure 6-14. FEM simulation results for mutual inductance along a ferrite material coated pipe showing comparisons with or without ferrite cores on the coils.

Adding ferrite cores, the magnetic coupling between the coils is improved, as the magnetic cores enhance the magnetic flux link between the transmitter and receiver. It is expected to see the same improvement on the power transfer efficiency. The simulation results of optimum power transfer efficiency are given in Figure 6-15.

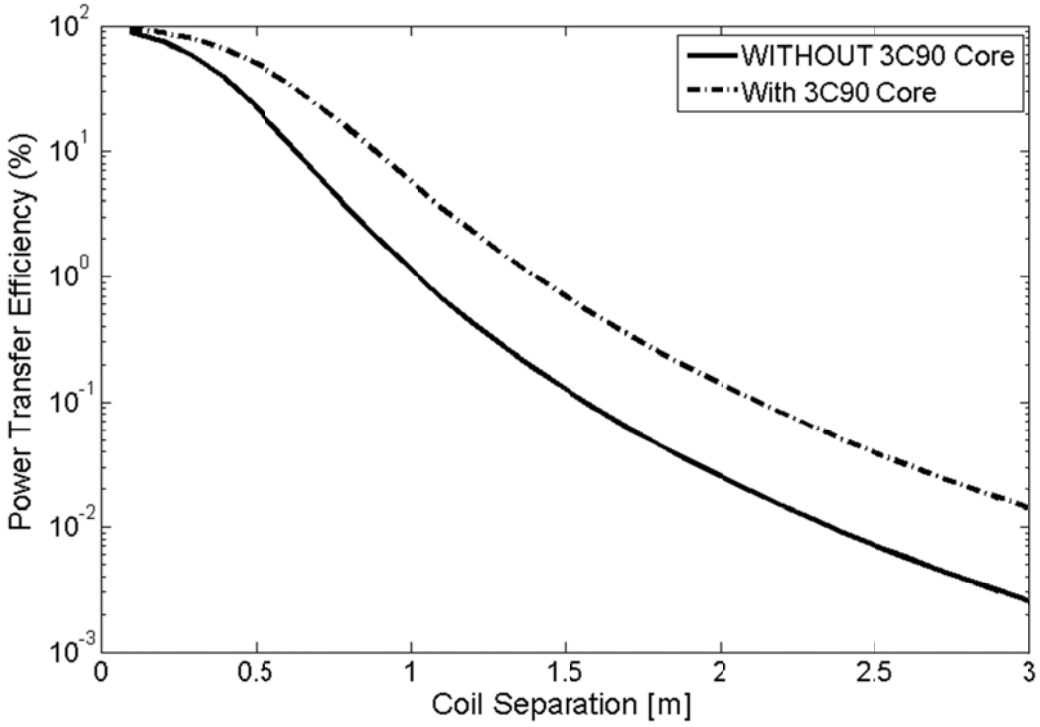

Figure 6-15. Simulation results for power transfer efficiency along a ferrite material coated pipe, showing comparisons with or without ferrite cores on the coils.

6.4.4 Ferrite Layer with Ferromagnetic Metal Pipe

The pipe metal used in simulation models given in Section 6.4.1 6.4.2 and 6.4.3 is stainless steel, and in simulation, we assume the permeability of the metal is 1. In actual applications in oil industry, it is possible that the metallic oil pipe is also ferromagnetic, which means the relative permeability (μ_r) of the pipe metal is larger than 1. Though such a ferromagnetic property of the metallic pipe might enhance the magnetic flux link between the transmitter and receiver, the eddy current induced inside the pipe might still be the dominant effect and such improvement of magnetic flux link could be trivial. In this section, we keep the same dimensions of the pipe, but we vary the permeability value of the pipe metal and explore the change of mutual inductance and power transfer

efficiency. The mutual inductance between the transmitter and receiver is shown in Figure 6-16.

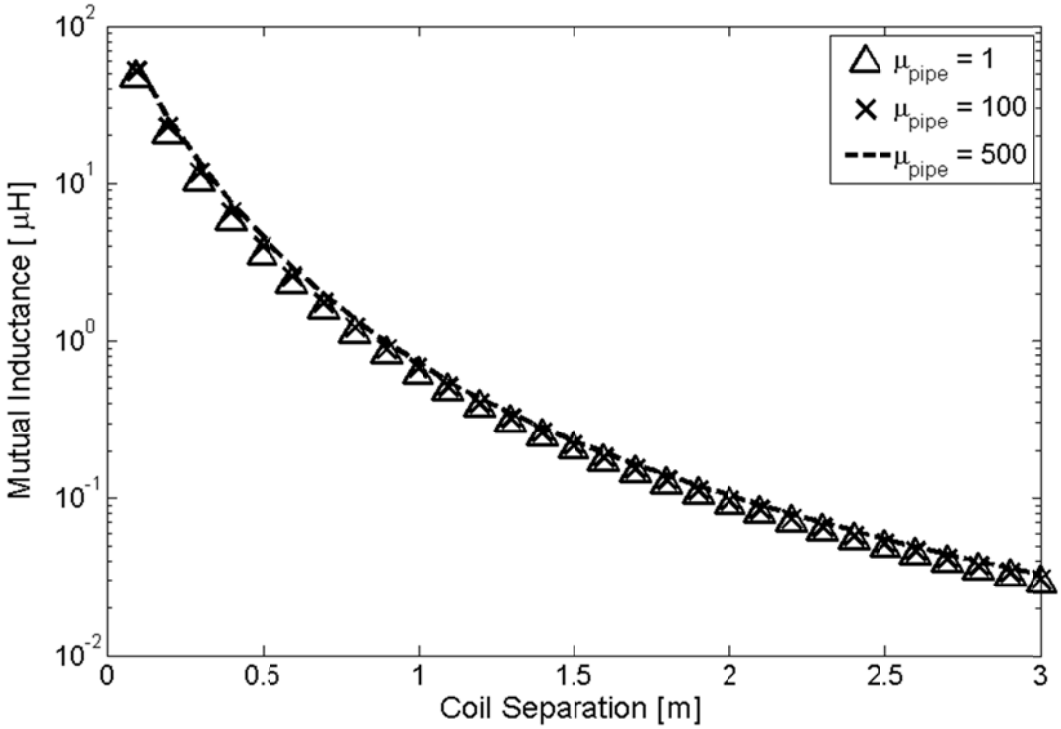

Figure 6-16. FEM simulation of mutual inductance with variation of pipe metal permeability.

The results in Figure 6-16 show that the mutual inductance of the system doesn't increase significantly when there is a large change of the pipe metal permeability. This is because the eddy current induced inside the pipe counteracts the additional magnetic flux brought by the ferromagnetic material. However, the simulation results show that the input resistance of the transmitter and receiver increases with the pipe metal permeability, as is shown in Figure 6-17.

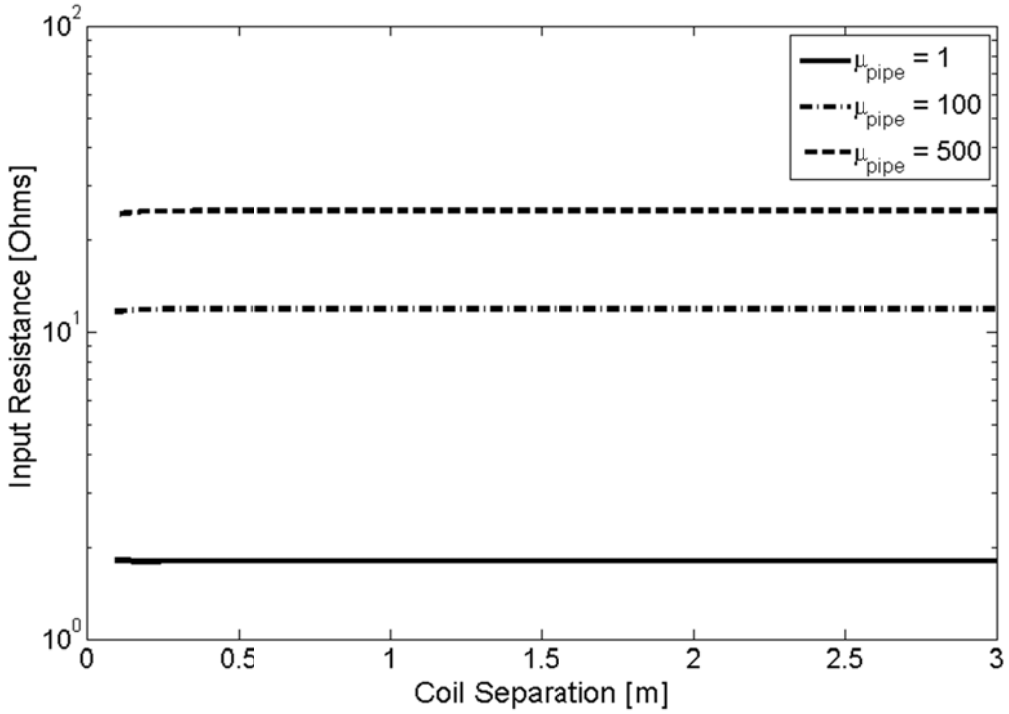

Figure 6-17. Input resistance of the transmitting coil on the metal pipe with a variation of the pipe metal permeability.

The input resistance data in Figure 6-17 shows that the input impedance of the transmitter increases with the pipe metal permeability. In the simulation model, the transmitting and the receiving coils are identical and their positions are symmetrical to the center of the metal pipe, so we assume that the input resistance of the receiver is the same with that of the transmitter. Combining the results shown in Figure 6-16 and Figure 6-17, we are expecting that the power transfer efficiency of the system will decrease as the permeability of the metal pipe becomes larger. The simulation results for power transfer efficiency are given in Figure 6-18.

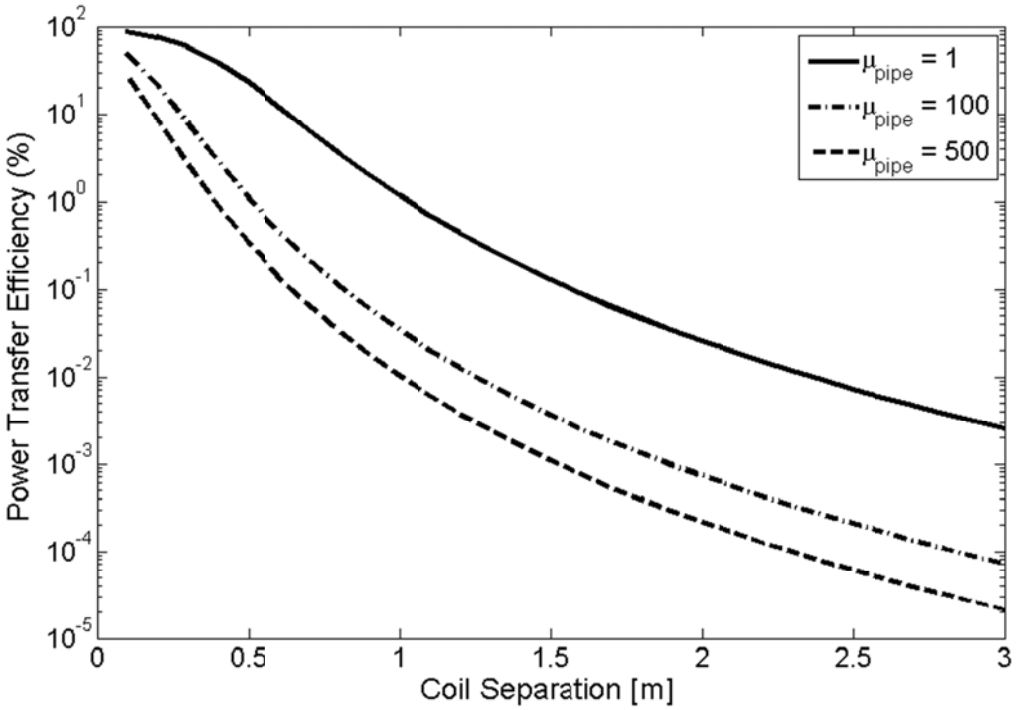

Figure 6-18. Simulation results for power transfer efficiency along a metal pipe with a variation in the pipe metal permeability.

The pipe permeability affects the power transfer efficiency negatively. In order to compensate the increase of input resistance brought by the pipe permeability, we could increase the thickness of the soft ferrite layer to enhance the magnetic coupling while reducing the eddy current effect inside the metallic pipe. While keeping the relative pipe metal permeability as 100, we plot the power transfer efficiency results from simulation with various soft ferrite layer thicknesses, and this is shown in Figure 6-19.

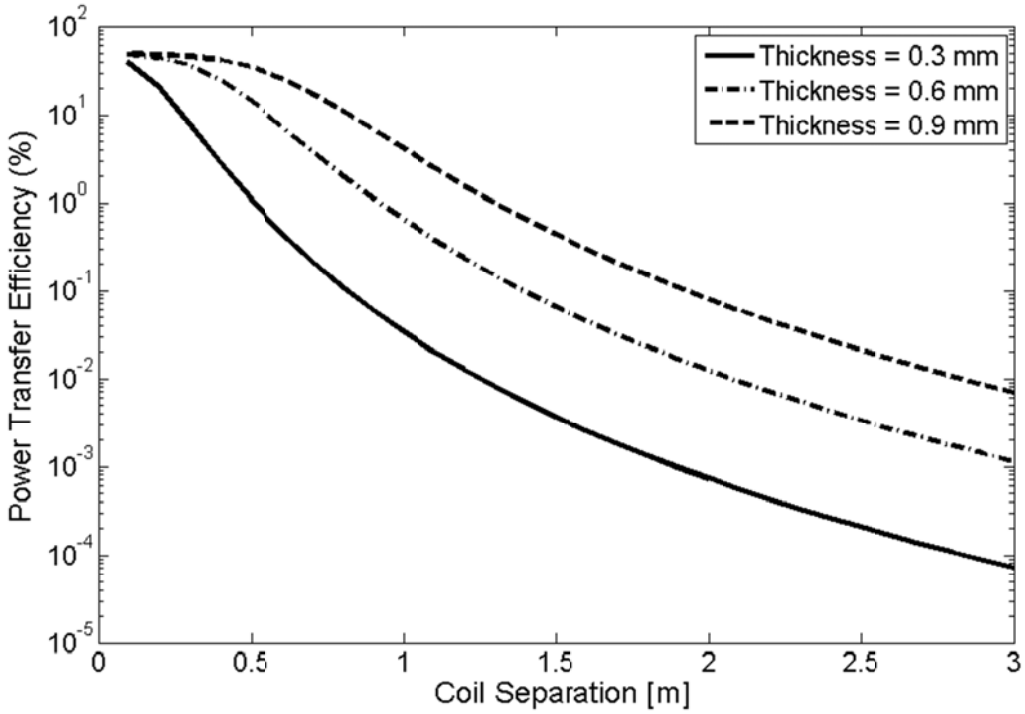

Figure 6-19. Power transfer efficiency along a ferromagnetic metal pipe with a variation of the soft ferrite layer thickness.

6.5 Experimental Validation

According to the previous discussion, we know that the improvement brought by a ferrite layer on the oil pipe is more obvious on a non-magnetic pipe than on a ferromagnetic pipe. In this section, we are also going to validate the simulation results with black steel pipes (which have the permeability μ_r larger than 1) and stainless steel pipes (which are slightly magnetic) in the lab. The ferrite layer we use is the experiment is made of 3M 1380 ferrite sheet. The permeability of the material is not provided by the manufacturer, but we are going to measure it ourselves.

6.5.1 Measuring Permeability of the Ferrite Sheet Material

We take a sample of the ferrite sheet with the shape of narrow rectangular, and we measure the permeability component along the long edge of the rectangular. We bind two identical samples together to increase the thickness of the sample so that it is easier to wind copper wires on it. We wind a testing coil with the ferrite sheet sample as the core, which is shown in Figure 6-20.

Figure 6-20. Coil wound on a 3M 1380 ferrite sheet sample.

We connect the sample coil to the RLC meter, and we measure the inductance and equivalent series resistance (ESR) of the coil at a frequency of 100 kHz. The RLC meter we use is a BK Precision 889 model, and the experimental setup of measuring the sample coil is shown in Figure 6-21.

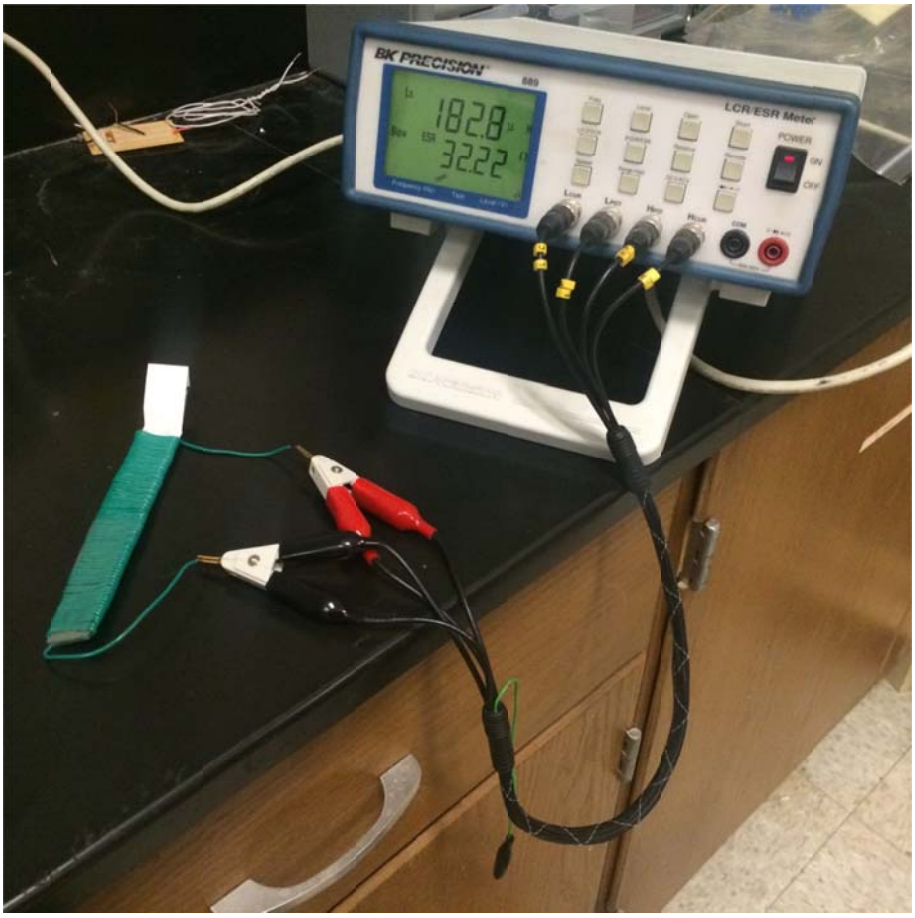

Figure 6-21. Experiment setup for measuring the sample coil inductance and resistance.

Once we obtained the inductance of the sample coil L_{sample}, we use the inductance formula for a long solenoid to calculate the permeability of the ferrite sheet [31]. The real part of the sample permeability is given by

$$\mu_r^{eff} = \frac{L_{sample} l_{sample}}{\mu_0 N_{sample}^2 A_{sample}}. \tag{6-3}$$

In (6-3), l_{sample} is the length of the sample coil, N_{sample} is the number of turns of the coil, and A_{sample} is the cross section area of the sample. We assume the sample ferrite sheet is narrow enough to approximate the coil as an infinitely long solenoid, so that (6-3) is accurate enough to estimate the material permeability. The imaginary part of the

permeability is estimated using the equivalent series resistance (ESR) of the coil. The ESR of the coil is contributed to by both the copper resistance and the magnetic loss tangent. The copper resistance is related to current frequency due to the proximity effect. For a single-layer coil, the AC resistance of the copper wire can be calculated as [32]

$$R_{ac}^{wire} = R_{dc}^{wire} A\left[\frac{\sinh(2A)+\sin(2A)}{\cosh(2A)-\cos(2A)}\right] \tag{6-4}$$

and

$$A = \left(\frac{\pi}{4}\right)^{3/4} \frac{d^{3/2}}{\delta t^{1/2}}. \tag{6-5}$$

In (6-5), d is the wire diameter and t is the distance between each turns. δ is the skin depth at a certain frequency. R_{dc}^{wire} is the DC resistance of the copper wire and can be directly measured using an RLC meter. Then, the ESR contributed by the magnetic loss tangent can be calibrated as

$$R_m = R_{sample} - R_{ac}^{wire}. \tag{6-6}$$

Then, the imaginary part of the material permeability is calculated as

$$\mu_i^{eff} = \frac{R_m l_{sample}}{2\pi f \mu_0 N_{sample}^2 A_{sample}}. \tag{6-7}$$

In (6-7), f is the frequency under which the resistance and inductance of the sample coil is measured. In the following table, we show the measured data relevant to the above analysis and the final results for the permeability of the material (which are shown in bold font numbers).

Table 6-2. Measurement Results for the Sample Ferrite Sheet.

Parameter (unit)	Value
f (kHz)	100
l_{sample} (mm)	145
A_{sample} (mm^2)	6
L_{sample} (uH)	153.3
R_{sample} (Ohms)	25.97
R_{wire}^{dc} (Ohms)	0.333
d (mm)	0.59
t (mm)	1.31
δ (mm)	0.206
R_{wire}^{ac} (Ohms)	0.49
R_m (Ohms)	25.5
μ_r^{eff}	**538**
μ_i^{eff}	**145**

The thickness of the ferrite sheet product is 0.3 mm but the actual magnetic layer inside the sheet is only 0.02 mm thick. Therefore, the permeability we measure in this section is the effective permeability of the ferrite sheet, that is to say, the average value of the permeability. We directly apply the overall thickness and the average permeability of the material to our FEM simulation and use the results to compare with the experimental data.

6.5.2 Ferrite Layer on a Black Steel Pipe

In this section, we build a wireless power transfer model along a ferromagnetic black steel pipe. We cover the pipe with a ferrite layer and add ferrite cores to the transmitting and the receiving coils. The conductivity and the permeability of the ferromagnetic pipe are unknown. We can only give our own estimation. In this section, we assume that the conductivity of the pipe is 1.1×10^6 S/m and the relative permeability of the pipe is 100. We apply these estimated parameter value to the FEM simulation and compare the results with the experiment. The experimental setup of the wireless power transfer system along the ferromagnetic black steel pipe is shown in Figure 6-22.

Figure 6-22. Experiment setup for wireless power transfer on a black steel pipe.

We measure the mutual inductance of the system and compare the data with FEM simulation results. Also, we remove the 3C90 ferrite core and 3M 1380 ferrite sheet from the system to see if the ferrite material does improve the magnetic coupling and power transfer efficiency. The experiment and simulation results for mutual inductance are given in Figure 6-23.

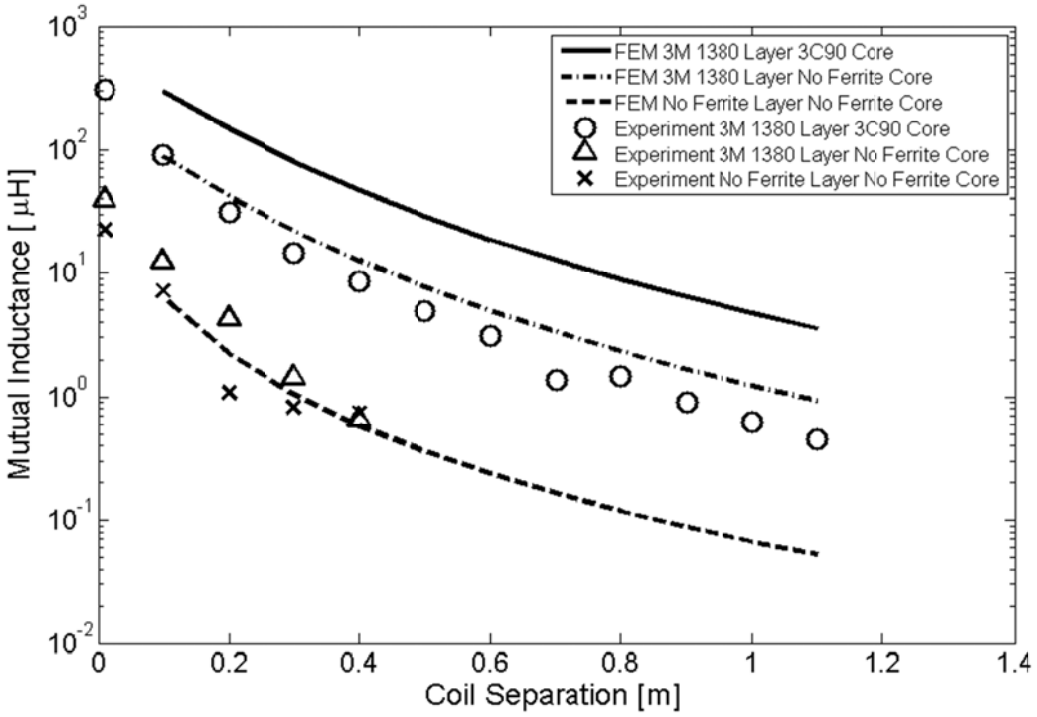

Figure 6-23. Experiment and simulation results for mutual inductance with a 3M 1380 ferrite layer on the pipe and 3C90 ferrite cores on the coils at 100 kHz.

Due to the fact that the conductivity and the permeability of the metal pipe are unknown, it is difficult for the simulation results to completely agree with the experiment. But still, we can see that the mutual inductance results for the coils on bare pipe agree with the experiment. This might also indicate that the measured permeability of the 3M 1380 ferrite sheet might not be accurate enough as well. Such an experimental procedure should be improved in the future. Also, we measured the power transfer

efficiency of the system and compare the data with simulation, and this is shown in Figure 6-23.

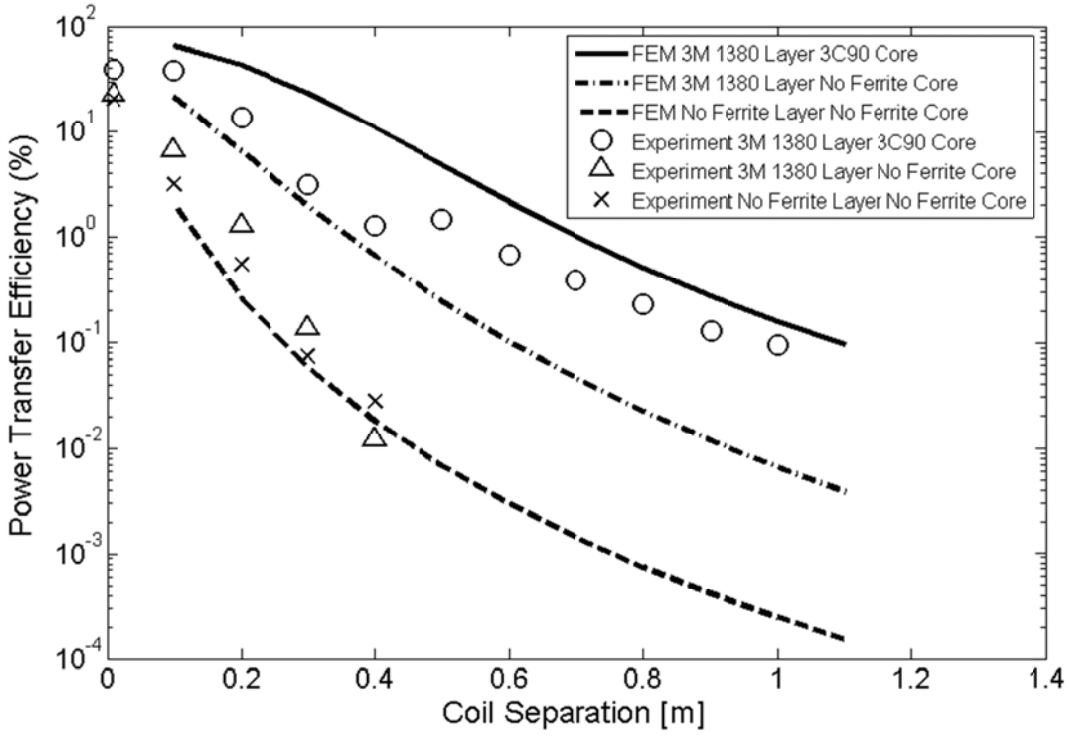

Figure 6-24. Experiment and simulation results for power transfer efficiency with a 3M 1380 ferrite layer on the pipe and 3C90 ferrite cores on the coils.

There are several possible reasons explaining in the inconsistency between the simulation and the experimental results. The permeability and conductivity of the metal pipe is unknown; the input power on the primary coil is not large enough to induce a relatively high voltage on the secondary coil that could overcome the noise. We measured the permeability of the 3M 1380 sheet with our own hand-wound coils, which also might add error to the FEM modeling. Still, we can see from both experiment and simulation that ferrite materials added to the system improves the power transfer efficiency. The ferromagnetic pipe increases the input resistance of the coil so the overall efficiency from

the experiment shows that merely adding a 3M 1380 ferrite layer might not improve the power transfer efficiency very much.

6.5.3 Ferrite Layer on a Stainless Steel Pipe

In this section, we build the wireless power transfer system on the stainless steel pipes in lab, and we measure the mutual inductance and power transfer efficiency to compare with FEM simulation results. It is estimated that the permeability of the stainless steel pipe is lesser than the black steel pipe. Here we assume that the permeability (μ_r) of the stainless steel pipe is 1. The experimental setup for the wireless power transfer system on the stainless steel pipe is shown in Figure 6-25.

Figure 6-25. Experimental setup for wireless power transfer on the stainless steel metal pipe.

This experiment setup is actually the same with one shown in Figure 4-8. But we will add a 3M 1380 ferrite sheet on the pipe to enhance the magnetic coupling. The outer diameter of the stainless steel pipe available in lab is larger than the inner diameter of the 3C90 ferrite core. So it is impossible to install ferrite cores on the coils. Therefore in this section we only explore the improvement brought by the 3M 1380 ferrite sheet. The experiment and simulation results of the mutual inductance are given in Figure 6-26.

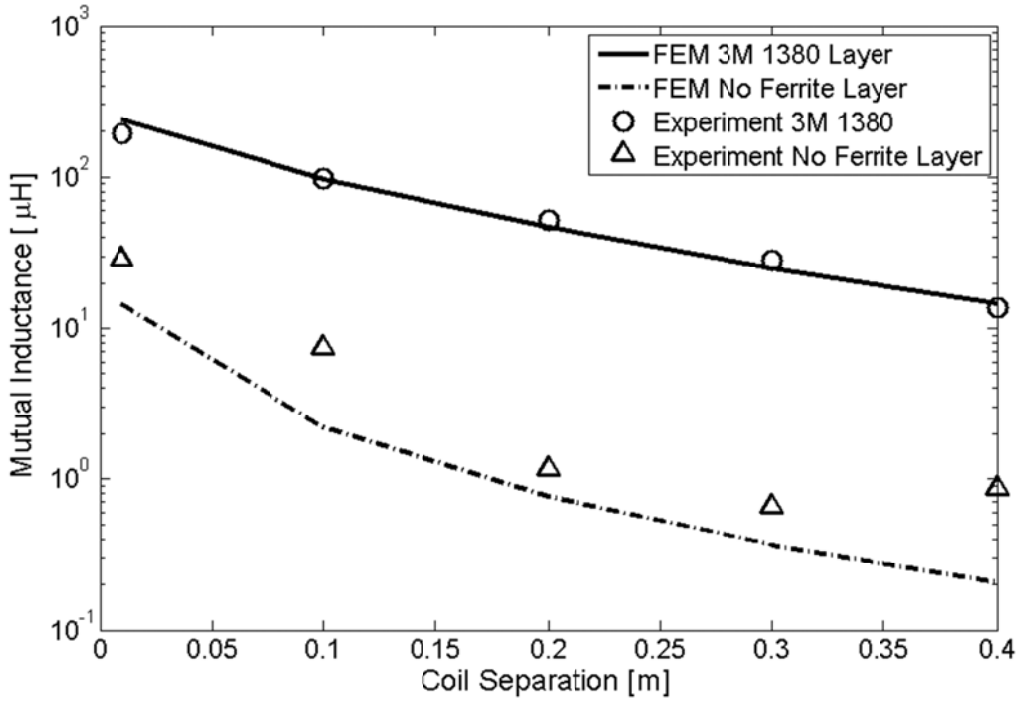

Figure 6-26. Experimental and simulation results for mutual inductance on a stainless steel pipe with 3M 1380 ferrite layer at 10 kHz.

We see a better agreement between the FEM simulation and experiment in this case. The results indicate that the experiment measurement of the 3M 1380 ferrite permeability is accurate enough to predict the mutual inductance. The experimental results for the mutual inductance on the bare nonmagnetic pipe are slightly off from the simulation data, and this is probably due to the fact that the input power to the primary

coil is small and the induced voltage on the secondary coil is affected by noise. In future we need to build power amplifier to amplify the power signal before it is sent to the primary coil. We also measure the power transfer efficiency and compare the results with FEM simulation, as is shown in Figure 6-27.

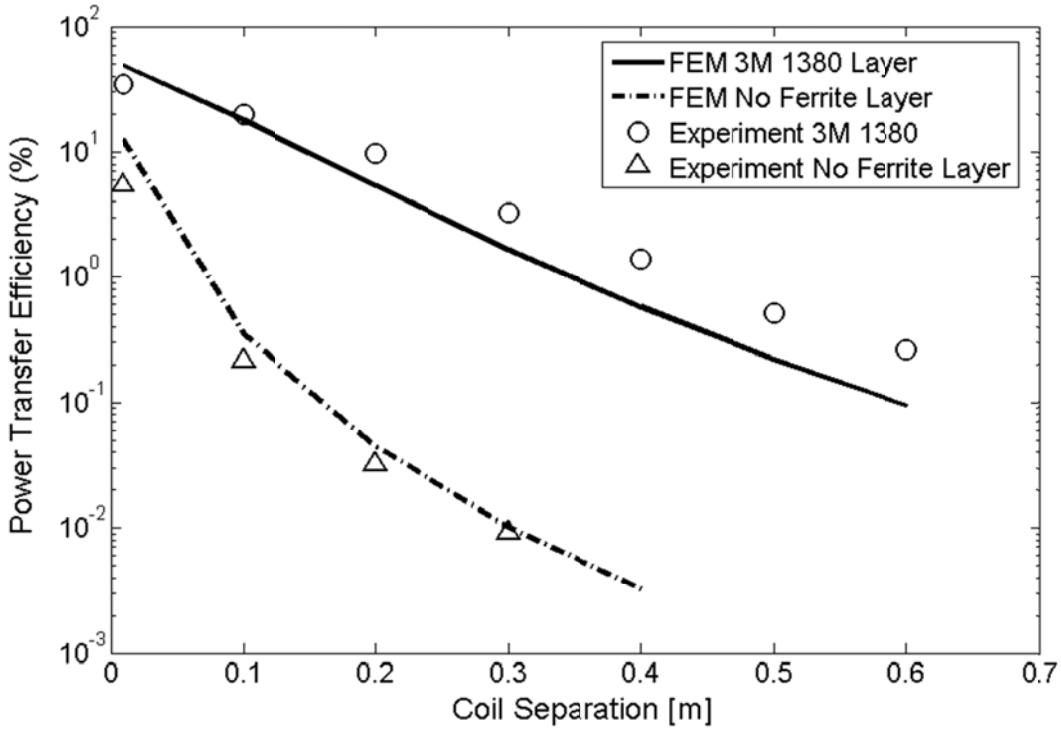

Figure 6-27. Experiment and simulation results of power transfer efficiency on the stainless steel pipe with 3M 1380 ferrite layer at 10 kHz.

We see better agreement for the power transfer efficiency. The magnetic loss tangent of the 3M 1380 layer is relatively high (about 0.27), and such a high loss tangent will add input resistance to the coils and reduce the power transfer efficiency. Therefore, in Figure 6-27, we lower the operation frequency to 10 kHz to reduce the loss effect. At a 10 kHz frequency, we can see that the ferrite layer on the nonmagnetic pipe enhances the magnetic coupling and increases the power transfer efficiency greatly.

Chapter 7 Summary and Conclusions

This dissertation shows a new approach for delivering power across the production packer along an oil pipe. There are previous works in this related area using a guided acoustic wave to deliver power along an oil pipe. Acoustic wave propagation will suffer from reflection at the production packers of the oil pipes. In this research, we deliver electric power using magnetic induction with a transmitting coil and a receiving coil at both sides of the production packer, and we add a soft ferrite layer on the metallic pipe and add ferrite cores to the transmitting and receiving coils to enhance the magnetic coupling. According to the simulation results presented in this dissertation, the magnetic coupling will not be obviously affected by discontinuous pipe breaks unless the length of the pipe break is approaching the coil separation distance. Therefore, delivering electric power using magnetic induction is a more practical option to provide power supply beyond the boundary brought by the production packers.

We analyze the model of two coils along the metallic pipe using analytical methods and FEM simulation. Using both approaches we discover that the main difficulty of applying a magnetic induction system to the oil pipe structure for power transfer is the eddy current effect on the metallic pipe. The eddy current effect reduce the magnetic coupling by generating an inverse magnetic field and increasing the ohmic loss of the overall power transfer system. Using the analogy of the magnetic circuit, we propose a way of improving the power transfer efficiency of the system by a adding soft ferrite layer on the metallic pipe and by adding soft ferrite cores to the coils. The soft ferrite materials have a relatively large magnetic permeability so that the ferrite structure

concentrates the magnetic flux generated by the transmitting coil, hence enhancing the magnetic coupling and improving the power transfer efficiency of the system.

We perform FEM simulation and experiments for wireless power transfer systems along metallic pipes, and discuss the improvement brought by the soft ferrite layer and the ferrite cores. We conclude that the ferrite layer on the metallic pipe enhances the magnetic coupling and therefore the mutual inductance between the transmitter and receiver increases. Adding thickness or selecting ferrite materials with a higher permeability will further improve the performance of the wireless power transfer system. Also, we point out that the performance of the wireless power transfer system is also related to the magnetic property of the oil pipe. Oil pipes made of ferromagnetic materials may increase the input resistance of the transmitting and the receiving coils so that the power transfer efficiency is affected negatively. We have good agreement between FEM simulation and experiment for the system built on the stainless steel pipe, but we do not see the same agreement on the system built on black steel pipe. This is due to the fact that the conductivity and permeability of the black steel pipe available in lab is unknown and the magnetic property of the stainless steel pipe is closer to our estimation.

We draw the conclusion that we can provide a new method of providing electric power across a production packer on an oil pipe by delivering power wirelessly via magnetic induction. We also provide a new oil pipe structure that has the pipe covered with soft ferrite layer. Such a layer concentrates the magnetic flux and acts as a magnetic pathway to deliver the magnetic field along the pipe. In the future, we will improve the model we implemented in lab and apply it to an actual oil well environment to further test the performance of this new wireless power transfer system along an oil pipe.

References

[1] "Well Integrity in Drilling and Well Operations," NORSOK, Lysaker, 2013.

[2] J. Anders, S. Rossberg, A. Dube, H. Engle and D. Andrews, "Well Integrity Operations at Prudhoe Bay, Alaska," in SPE Annual Technical Conference and Exhibition, San Antonio, 2006.

[3] C. Teodoriu, C. Kosinowski, M. Amani, J. Schubert and A. Shadravan, "Wellbore Integrity and Cement Failure at HPHT Conditions," International Journal of Engineering and Applied Sciences, vol. 2, no. 2, 2013.

[4] Y. L. Guen, S. Asamoto, E. Houdu and O. Poupard, "Well Integrity: Modeling of Thermo-Mechanical Behavior and Gas Migration along Wells - Application to Ketzin Injection Well," Energy Procedia, vol. 23, pp. 462-471, 2012.

[5] P. C. Ogle, "Well Integrity Monitoring System," US Patent 6,957,574 B2, 25 Oct 2005.

[6] A. Leitch, "Switch Mechanisms that Allow a Single Power Cable to Supply Electrical Power to Two or More Downhole Electrical Motors Alternatively and Methods Associated therewith," US Patent 8,353,352 B2, 15 January 2013.

[7] N. Tesla, "System of Transmission of Electrical Energy," US Patent 645,576, 20 March 1900.

[8] N. Tesla, "Apparatus for Transmitting Electrical Energy," US Patent 1,119,732, 4 May 1907.

[9] A. Kurs, A. Karalis, R. Moffat, J. D. Joannopoulos, P. Fisher and M. Soljacic, "Wireless Power Transfer via Strongly Coupled Magnetic Resonances," Science, vol. 317, no. 5834, pp. 83-86, 2007.

[10] X. Xin, D. R. Jackson, J. Chen and P. Tubel, “Wireless Power Transfer for Oil Well Applications,” in 2013 IEEE International Symposium on Electromagnetic Compatibility (EMC), Denver, 2013.

[11] K. E. Koh, T. C. Beh, T. Imura and Y. Hori, “Impedance Matching and Power Division Using Impedance Inverter for Wireless Power Transfer via Magnetic Resonant Coupling,” IEEE Transactions on Industry Applications, vol. 50, no. 3, pp. 2061-2070, 2014.

[12] S.-H. Lee and R. D. Lorenz, “Development and Validation of Model for 95%-Efficiency 220-W Wireless Power Transfer Over a 30-cm Air Gap,” IEEE Transactions on Industry Applications, vol. 47, no. 6, pp. 2495-2504, 2011.

[13] C. A. Balanis, “Power Density and Radiation Resistance,” in Antenna Theory, New Jersey, John Wiley & Sons, Inc., 2005, pp. 237-241.

[14] J. S. Ho, A. J. Yeh, E. Neofytou, S. Kim, Y. Tanabe, B. Patlolla, R. E. Beygui and A. S. Y. Poon, “Wireless Power Transfer to Deep-Tissue Microimplants,” Proceedings of the National Academy of Sciences, vol. 111, no. 22, pp. 7974-7979, 2014.

[15] I.-J. Yoon and H. Ling, “Realizing Efficient Wireless Power Transfer Using Small Folded Cylindrical Helix Dipoles,” IEEE Antennas and Wireless Propagation Letters, vol. 9, pp. 846-849, 2010.

[16] M. G. L. Roes, J. L. Duarte, M. A. M. Hendrix and E. A. Lomonova, “Acoustic Energy Transfer: A Review,” IEEE Transactions on Industrial Electronics, vol. 60, no. 1, pp. 242-248, 2013.

[17] G. G. Stokes, “On the Theories of the Internal Friction in Fluids in Motion, and of the Equilibrium and Motion of Elastic Solids,” Transaction of the Cambridge Philosophical Society, vol. 8, no. 22, pp. 287-342, 1845.

[18] H. R. Scarton, G. J. Saulnier and K. R. Wilt, “Method and Apparatus for Acoustical Power Transfer and Communication,” WO Patent 2014035785 A1, 6 March 2014.

[19] M. Kesler, “Highly Resonant Wireless Power Transfer: Safe, Efficient and over Distance,” WiTricity Corporation, Watertown, MA, 2013.

[20] D. Pozar, Microwave Engineering, John Wiley & Sons, Inc., 2012.

[21] S. Kim, J. S. Ho and A. S. Y. Poon, “Wireless Power Transfer to Miniature Implants: Transmitter Optimization,” IEEE Transactions on Antennas and Propagation, vol. 60, no. 10, pp. 4838-4845, 2012.

[22] S. Ramo, J. R. Whinnery and T. V. Duzer, “Mutual Inductance,” in Fields and Waves In Communication Electronics, 3rd Edition, New York, John Wiley & Sons, Inc., 1993, pp. 189-193.

[23] R. F. Harrington, “Cylindrical Wave Functions,” in Time-Harmonic Electromagnetic Fields, New York, IEEE Press, 2001, pp. 198-263.

[24] L. C. Shen, “Theory of a Coil-Type Resistivity Sensor for MWD Application,” The Log Analyst, vol. 32, no. 5, pp. 603-611, 1991.

[25] W. C. Chew, “Planary Layered Media,” in Waves and Fields in Inhomogeneous Media, New York, IEEE Press, 1995.

[26] Soft Ferrites: A User's Guide, Chicago: Magnetic Materials Producers Association, 1998.

[27] Soft Ferrite and Acessories Data Handbook, Ferroxcube, 2013.

[28] C. Park, S. Lee, G.-H. Cho and C. T. Rim, “Innovative 5-m-Off-Distance Inductive Power Transfer Systems With Optimally Shaped Dipole Coils,” IEEE Transactions on Power Electronics, vol. 30, no. 2, pp. 817-827, 2015.

[29] D. A. Bell, “Magnetic Circuits,” in Electric Circuits, 6th Edition, Sarnia, Ontario, David A. Bell, 1998, pp. 267-295.

[30] FLEXIBLE FERRITE SHEET For Wireless Power Charger, Toda Kogyo Corp., 2012.

[31] L. S. Lerner, “Inductance,” in Physics for Scientists and Engineers, Volume 2, Jones & Bartlett Learning, 1997, pp. 851-863.

[32] M. K. Kazimierczuk, G. Sancineto, G. Grandi, U. Reggiani and A. Massarini, “High-Frequency Small-Signal Model of Ferrite Core Inductors,” IEEE Transactions on Magnetics, vol. 35, no. 5, pp. 4185-4191, 1999.

[33] G. N. Watson, “The Harmonic Functions Associated with the Parabolic Cylinder,” Proceedings of the London Mathematical Society, vol. 2, no. 17, pp. 116-148, 1918.

[34] B. G. Korenev, Bessel Functions and Their Applications, CRC Press, 2002.

Appendix

In this appendix material, we are going to give a mathematical derivation of the asymptotic formula for mutual inductance along a metallic pipe given by (3-38). This result was originally published by Shen [24] without a derivation. We examine the infinite integral form of the electric field at the secondary coil and we are able to give a derivation by deforming the integration contour and applying Watson's lemma [33]. Assuming the secondary coil has the same radius as primary coil (which is illustrated in Figure 3-2), the electric field on the secondary coil is given by

$$E_{\phi 0}^{tot}\Big|_{\rho=a} = \left(\frac{\omega\mu_0 a}{4}\right)\int_{-\infty}^{+\infty} F^{PEC}\left(k_{\rho 0}\right) J_1(k_{\rho 0}a) H_1^{(2)}(k_{\rho 0}a) e^{-jk_z D_{coil}}\, dk_z, \tag{A-1}$$

in which

$$F^{PEC}(k_\rho) = 1 - \frac{H_1^{(2)}(k_{\rho 0}a) J_1(k_{\rho 0}b)}{H_1^{(2)}(k_{\rho 0}b) J_1(k_{\rho 0}a)}. \tag{A-2}$$

We deform the integration contour around the branch point of $k_z = k_0$, which is shown in Figure A-1.

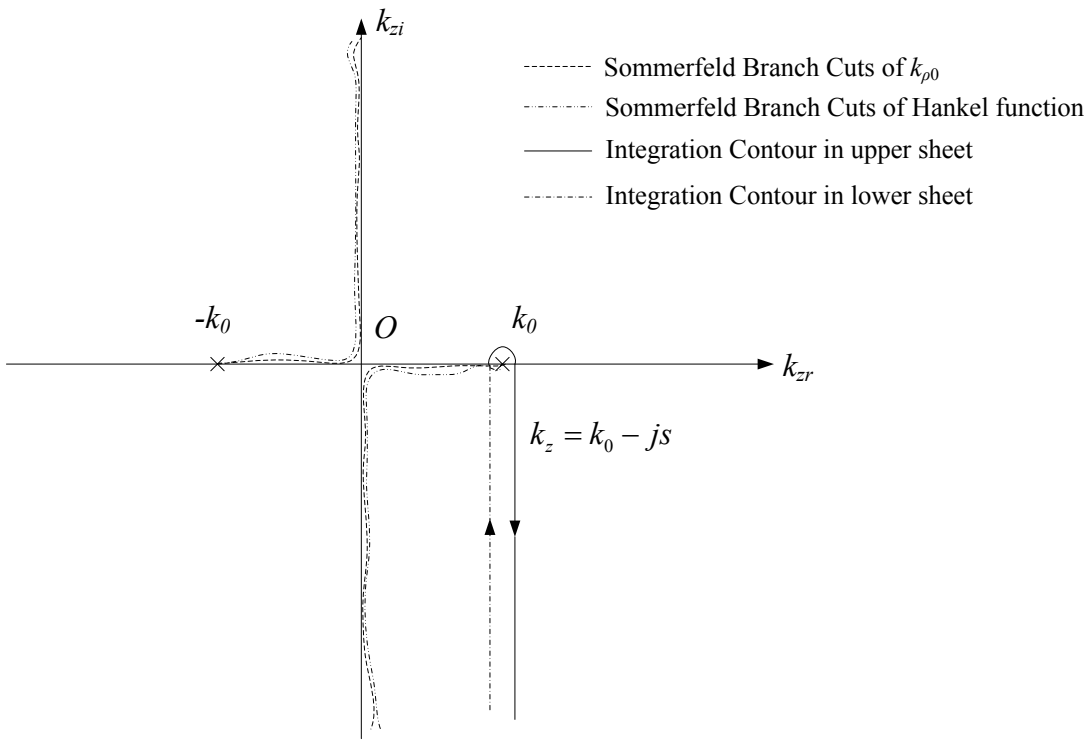

Figure A-1. Deformed integration contour for asymptotic approximation.

The integration contour shown in Figure A-1 is actually along the path of $k_z = k_0 - js$. It goes towards the real axis in the lower sheet (in which $k_{\rho 0}$ is improper) and goes way from real axis in the upper sheet (in which $k_{\rho 0}$ is proper). The wave number $k_{\rho 0}$ is then given by

$$k_{\rho 0} = \sqrt{k_0^2 - (k_0 - js)^2} = \sqrt{2jk_0 s + s^2}. \tag{A-3}$$

Clearly we have two branches of $k_{\rho 0}$, one is the first quadrant (improper) and one is in the third quadrant (proper), and both branches of $k_{\rho 0}$ are the functions of s. If we assume that function $k_{\rho 0}(s)$ is a proper wave number on the upper sheet, then it is an improper wave number on the lower sheet. Next, we define

$$H^-(s) = F^{PEC}\left(-k_{\rho 0}(s)\right) J_1(-k_{\rho 0}(s)a) H_1^{(2)}(-k_{\rho 0}(s)a) \tag{A-4}$$

and

$$H^{+}(s) = F^{PEC}\left(k_{\rho 0}(s)\right) J_1(k_{\rho 0}(s)a) H_1^{(2)}(k_{\rho 0}(s)a). \tag{A-5}$$

Then, (A-1) can be rewritten as

$$E_{\phi 0}^{tot}\Big|_{\rho=a} = -j\left(\frac{\omega\mu_0 a}{4}\right) e^{-jk_0 D_{coil}} \int_0^{+\infty} (H^{+}(s) - H^{-}(s)) e^{-sD_{coil}} ds. \tag{A-6}$$

When the coil separation D_{coil} becomes large, the integration function in (A-6) will decay very fast as s goes away from the real axis. Then, most of the contribution of the integral comes from the branch point where $k_{\rho 0} \to 0$. Therefore, we could apply asymptotic forms to the Bessel and Hankel functions appeared in (A-4) and (A-5). The first order Bessel function of the first kind can be given as [34]

$$\begin{aligned} J_1(x) &= \frac{x}{2} - \frac{x^3}{2^2 \cdot 4} + \frac{x^5}{2^2 \cdot 4^2 \cdot 6} - \frac{x^7}{2^2 \cdot 4^2 \cdot 6^2 \cdot 8} + \ldots \\ &= \frac{x}{2} + e_1(x). \end{aligned} \tag{A-7}$$

The function $e_1(x)$ is the sum of all terms in (A-7) except the leading term $x/2$, and apparently $e_1(x)$ converges to 0 faster than the leading term. For the first order Hankel function of the second kind, the series expansion is given as [34]

$$\begin{aligned} Y_1(x) &= \frac{2}{\pi}\left\{\ln\frac{x}{2} + \gamma\right\} J_1(x) - \frac{2}{\pi x} - \frac{1}{\pi}\sum_{k=0}^{\infty} (-1)^k \left\{\phi(k) + \phi(1+k)\right\} \frac{(x/2)^{2k+1}}{k!(1+k)!} \\ &= -\frac{2}{\pi x} + e_2(x). \end{aligned} \tag{A-8}$$

In (A-8), $e_2(x)$ is the sum of all residual terms except the leading term and it converges to zero when x approaches to zero. Therefore, the first order Hankel functions can be given by

$$\begin{aligned} H_1^{(1)}(x) &= J_1(x) + jY_1(x) \\ &= \frac{x}{2} + e_1(x) + j\left(-\frac{2}{\pi x} + e_2(x)\right) \end{aligned} \tag{A-9}$$

and

$$H_1^{(2)}(x) = J_1(x) - jY_1(x)$$
$$= \frac{x}{2} + e_1(x) + j\left(\frac{2}{\pi x} - e_2(x)\right). \tag{A-10}$$

Substituting (A-7), (A-9) and (A-10) into (A-6), The E field can be asymptotically expressed as

$$\begin{aligned}
E_{\phi 0}^{tot}\Big|_{\rho=a} &\sim -j\left(\frac{\omega\mu_0 a}{4}\right)e^{-jk_0 D_{coil}}\left(\int_0^{+\infty}\frac{1}{2}a^2k_\rho^2\left(1-\frac{b^2}{a^2}\right)e^{-sD_{coil}}ds\right. \\
&\qquad \left. +\int_0^{+\infty}\left(-\frac{1}{\pi^2}\right)\left(\frac{a}{b}-\frac{b}{a}\right)\frac{\frac{1}{2}abk_\rho^2}{\left(\frac{abk_\rho^2}{4}+\frac{k_\rho a}{2}e_1\left(k_\rho b\right)\right)^2+\left(\frac{1}{\pi}\frac{b}{a}-\frac{k_\rho a}{2}e_2\left(k_\rho b\right)\right)^2}e^{-sD_{coil}}ds\right) \\
&\sim -j\left(\frac{\omega\mu_0 a}{4}\right)e^{-jk_0 D_{coil}}\left(\int_0^{+\infty}\frac{1}{2}a^2k_\rho^2\left(1-\frac{b^2}{a^2}\right)e^{-sD_{coil}}ds\right. \\
&\qquad \left. +\int_0^{+\infty}\left(\frac{b}{a}-\frac{a}{b}\right)\frac{1}{2}ab\left(\frac{b}{a}\right)^2k_\rho^2e^{-sD_{coil}}ds\right) \\
&= -j\left(\frac{\omega\mu_0 a}{4}\right)e^{-jk_0 D_{coil}}\int_0^{+\infty}\frac{1}{2}a^2k_\rho^2\left(1-\frac{2b^2}{a^2}+\frac{b^4}{a^4}\right)e^{-sD_{coil}}ds \\
&= -j\left(\frac{\omega\mu_0 a^3}{4}\right)\left(1-\frac{b^2}{a^2}\right)^2\frac{1+jk_0D_{coil}}{D_{coil}^2}e^{-jk_0D_{coil}}.
\end{aligned} \tag{A-11}$$

If we apply the same procedure to the two coil system without the metallic pipe, then the incident E field on the secondary coil is given as

$$E_{\phi 0}^{inc}\Big|_{\rho=a} = -j\left(\frac{\omega\mu_0 a^3}{4}\right)\frac{1+jk_0D_{coil}}{D_{coil}^2}e^{-jk_0D_{coil}}. \tag{A-12}$$

Therefore, the total E field on the secondary coil with metallic pipe can be calculated as

$$E_{\phi 0}^{tot}\Big|_{\rho=a} = \left(1-\frac{b^2}{a^2}\right)^2 E_{\phi 0}^{inc}\Big|_{\rho=a}. \tag{A-13}$$